Surface Soil Moisture Dynamics from Remote Sensing, Modeling, and In Situ Observations

by

Peter J. Shellito

B.A., Dartmouth College, 2009

A thesis submitted to the

Faculty of the Graduate School of the

University of Colorado in partial fulfillment

of the requirements for the degree of

Doctor of Philosophy

Department of Geological Sciences

2017

This thesis entitled:
Surface Soil Moisture Dynamics from Remote Sensing, Modeling, and In Situ Observations
written by Peter J. Shellito
has been approved for the Department of Geological Sciences

Eric Small

Ethan Gutmann

Ben Livneh

Shemin Ge

Balaji Rajagopalan

Date: ______________________

The final copy of this dissertation has been examined by the signatories, and we find that both the content and the form meet acceptable presentation standards of scholarly work in the above mentioned discipline.

Shellito, Peter Judd (Ph.D., Department of Geological Sciences)

Surface Soil Moisture Dynamics from Remote Sensing, Modeling, and In Situ Observations

Dissertation directed by Professor Eric E. Small

Soil moisture content plays a central role in the coupled water and energy exchange between the land surface and the atmosphere. It also controls infiltration rates and is therefore key to predicting groundwater recharge and discharge. Land Surface Models (LSMs) use meteorologic data with parameterizations of local soil and vegetation conditions to simulate soil moisture, runoff, and turbulent fluxes. Accurate predictions of droughts, floods, crop productivity, and climate change depend on our ability to understand and model the state and dynamics of surface soil moisture.

Satellite-based remote sensing missions provides global coverage and therefore offer the potential to improve existing LSMs. We use remotely-sensed and *in situ* soil moisture observations from seven well-instrumented field sites to estimate soil hydraulic properties (SHPs) in the Noah LSM. Default SHPs are based on mapped soil type, but ample evidence shows that soil type is a poor predictor of hydraulic behavior. Improvements can be made by calibrating these parameters to unbiased observations of surface soil moisture, especially when the dynamics of the default model are poor.

Remotely-sensed soil moisture observations measure between the surface and up to 5 cm depth. However, the shallowest layer of most LSMs and the placement of *in situ* probes is typically centered at 5 cm. This depth discrepancy affects observations of soil moisture dynamics. We find that after rain events, NASA's SMAP (Soil Moisture Active Passive) satellite observes drying to occur over a 44% shorter timescale and twice as fast as 17 *in situ* validation networks spread across the globe.

Lastly, we demonstrate the strengths of SMAP and document how it differs from Noah simulated soil moisture over North America during drydown periods. Both SMAP and Noah drying rates depend on potential evaporation, soil moisture content, and vegetation. SMAP retrievals show that areas with sparse vegetation dry faster than areas with dense vegetation. Noah simulations show the opposite. After normalizing by potential evaporation, however, both SMAP and Noah data show that increased vegetation cover corresponds with lower evaporative efficiency. These differences are related to sensing depth and may also provide indications for how models can be improved.

Acknowledgements

I am grateful for all the support I have received at the University of Colorado Boulder. These five years have presented challenges that have tested my abilities and given me opportunities to grow and learn.

My advisor Eric Small diligently guided me towards useful research and often reminded me not to sweat the details. I would surely still be working on my first project if not for his coaching and encouragement. He has served as a role model for what a healthy work-life balance can be, and I am happy to have collaborated with someone with a well-rounded set of priorities.

Ethan Gutmann has patiently provided me with ideas and context for my research. His ongoing work at NCAR reminds me of the importance of my own work and the opportunities that exist to apply it outside of my academic field.

I am thankful that I have gotten to see the career of Ben Livneh take hold here at CU. He has provided me with questions, answers, and introductions that have widened my horizon and made me think critically about modeling and academic life.

The tireless work of Shemin Ge has instilled in me the importance not only of diligence but also of strong relationships and university service. I am happy to have her leading the department and grateful for the opportunities she has given me within it.

While the Geological Sciences has been home, Balaji Rajagopalan welcomed me into another of CU's world-class departments. He provided me with rigorous analytical techniques and encouraged me to think critically about systems and models. I have used his lessons in my research and to better understand and qualify the work of others.

Collaborators who are not on my committee include many talented and supportive scientists. Michael Cosh contributed to Chapter 2 and 3. Andreas Colliander, Rajat Bindlish, David Bosch, David Goodrich, John Prueger, Patrick Starks, Aaron Berg, Todd Caldwell, Heather McNairn, Rogier van der Velde, and Jeffrey Walker contributed to Chapter 3. The SMAP team, including Rajat Bindlish, Steven Chan, Tom Jackson, Peggy O'Neill, and Eni Njoku has been generous in sharing data and providing feedback.

Friends and lab mates who have been by my side have helped me make sense of data, programs, classwork, and my own self. Thank you to Clara Chew, Sarah Evans, Thomas Enzminger, Shahen Huda, Emily Carbone, Emily Fairfax, William Armstrong, Sarah Crump, Nadine Reitman, Steven Henning, and Rob Littlefield.

Lastly, I thank my family—Drs. Paul and Barbara Shellito, John and Haley Shellito, and Dr. Cailey Condit—for unparalleled support and love.

Research has been supported by NASA Grant NNX13AF43G. The data used in this study were acquired as part of the mission of NASA's Earth Science Division and archived and distributed by the Goddard Earth Sciences (GES) Data and Information Services Center (DISC).

Table of Contents

List of Figures

List of Tables

Chapter 1: Introduction

By studying soil moisture and its role in the hydrologic cycle, hydrologists can improve weather forecasts, flood and drought assessments, crop yields, freshwater availability estimates, and climate predictions. Aside from being a storage reservoir and mediating runoff and infiltration rates, available liquid water can change phase to vapor and therefore affect the relative intensities of latent and sensible heat fluxes. Relatively small differences in energy partitioning have a significant impact on boundary layer processes [Schär et al., 1999]. So while precipitation events are short-lived (minutes to days), resulting soil moisture anomalies can persist and influence the atmosphere for months [Delworth and Manabe, 1993]. Wet soils are linked to increases in precipitation, and the mechanism behind this connection includes changes to net radiation, land surface temperatures, evapotranspiration, and carbon fluxes [Entekhabi et al., 1996; Eltahir, 1998; Schär et al., 1999; Koster et al., 2004; Daly and Porporato, 2005]. Such variables are critical to hydrology, ecology, biogeochemistry, and climate. A better understanding and quantification of soil moisture processes is therefore key to reducing uncertainties in future climate projections with regard to extreme events, agriculture, and ecology [Seneviratne et al., 2010].

Soil moisture is most commonly expressed in terms of the volume of water present in a volume of soil ($cm^3\ cm^{-3}$). To directly ascertain this "volumetric soil moisture" (VSM), one must use destructive methods: oven-dry a soil sample of known volume, and use the resulting change in water mass to calculate VSM of the original sample. Continuous monitoring efforts must therefore utilize indirect observation techniques. In my research, I use three distinct methods to estimate soil moisture: *in situ* soil moisture probes, remote sensing, and modeling.

In situ probes determine VSM using a well-established relationship between the soil's dielectric properties and moisture content [*Topp et al.*, 1980]. Though such probes have good precision and accuracy, they characterize only the few centimeters surrounding them [*Topp and Davis*, 1985; *Ferré et al.*, 1998]. Horizontal variability is significant, so scaling from individual probe measurements to the field scale requires many instruments to be installed and maintained [*Western et al.*, 2002; *Famiglietti et al.*, 2008]. The expense and small-scale nature of *in situ* methods therefore prohibit their direct use at the continental scale.

Remote sensing of soil moisture offers a more efficient observation method. It has been known for some time there is a correlation between surface soil moisture content and passive microwave emissions [*Njoku and Kong*, 1977; *Dobson et al.*, 1985; *Ulaby et al.*, 1986; *Jackson and O'Neill*, 1987; *Njoku and Entekhabi*, 1996]. More recently, this knowledge has been used to develop two satellites whose primary mission is to measure soil moisture from space: the Soil Moisture Ocean Salinity (SMOS) mission of the European Space Agency (ESA) launched in November 2009, and the Soil Moisture Active Passive mission of the National Aeronautics and Space Administration (NASA) launched in January 2015 [*Kerr et al.*, 2010b; *Entekhabi et al.*, 2014]. Satellite remote sensing platforms are useful for hydrologic research because unlike *in situ* probes, their observations are global and large-scale (10s of kilometers).

Like remote sensing platforms, model products can characterize soil moisture anomalies on a continuous, continental scale [*Xia et al.*, 2012b]. Land surface models (LSMs) such as Noah contain empirically- and theoretically-derived equations that predict how meteorologic observations will affect water storage, runoff, streamflow, soil temperature, and turbulent fluxes [*Ek et al.*, 2003].

The goal of this research is to assess the utility and characteristics of satellite-based soil moisture by comparing remote sensing products to both *in situ* data and land surface models. In this dissertation, I present (Chapter 2:) a study of how observed surface soil moisture can be used in a data assimilation framework to improve Noah LSM soil moisture simulations, (Chapter 3) an investigation into how *in situ* probes and SMAP retrievals observe the dissipation of moisture anomalies differently, and (Chapter 4) model-based insight into the utility of SMAP-observed soil moisture anomalies on a continental scale. In this way, I provide the community with a better understanding of the advantages and limitations of microwave remote sensing.

Chapter 2: Calibration of Noah soil hydraulic property parameters using surface soil moisture from SMOS and basin-wide *in situ* observations

2.1 Background

When a precipitation event wets the ground surface, the pathway water takes depends on the soil's characteristics. Hydrologic LSMs use soil hydraulic properties (SHPs) to parameterize various soil types and generate reasonable simulations of the redistribution and drainage of water through the soil column. Surface and root zone soil moisture content affects runoff, baseflow, and partitioning of net radiation between ground, sensible, and latent heat fluxes (LHF) [*Betts et al.*, 1996; *Entekhabi et al.*, 1996]. Water and energy fluxes are thus dependent on SHPs. Land surface parameterizations and soil properties in particular have been shown to significantly affect continental-scale climate simulations [*Pitman*, 2003; *Osborne et al.*, 2004; *Richter et al.*, 2004; *Guillod et al.*, 2013].

SHPs in LSMs are typically assigned using laboratory-derived look-up tables or empirical functions, both based on mapped soil texture [*Teuling et al.*, 2009]. This approach is problematic because soil texture is a poor predictor of SHPs [*Gutmann and Small*, 2005, 2007]. The existence of soil texture maps allows the practice to persist despite overwhelming evidence that it is ill-suited. First, mapped texture classes often do not match the texture observed at the site. *Xia et al.* [2015] show that correcting for such mismatches does not categorically improve the root mean squared difference (RMSD) between simulations and *in situ* observations. Values for both range from 0.03 to 0.09 $cm^3 cm^{-3}$. Second, models use the mean SHP values of each texture class, but commonly used soil databases (including *Holtan et al.* [1968], *Rawls et al.* [1976], and *Schaap and Leij* [1998]) exhibit more SHP variation within a single texture class than between the 12 class means [*Soet and Stricker*, 2003; *Gutmann and Small*, 2005, 2007; *Harrison et al.*, 2012]. This indicates an arbitrary discretization of SHPs and a decrease in soil property diversity, which decreases the likelihood of accurate soil properties [*Wösten et al.*, 1995]. Third, the scale of LSMs (typically 1-50 km) is incommensurate with that of laboratory (~10 cm) measurements. Soil properties are different when measured at a large scale because they must account for smaller-scale heterogeneities [*Grayson and Blöschl*, 2000; *Harter and Hopmans*, 2004]. Fourth, soil structure, organic material, bulk density, and preferential flow through macropores influence soil drainage but are not captured by the typical assignation of sand/silt/clay percentages or texture class [*Beven and Germann*, 1982; *Soet and Stricker*, 2003; *Gutmann and Small*, 2005, 2007]. And finally, although use of the Richards equation at field and watershed scales is common, it is not based on sound physical basis; models at the kilometer scale only provide effective representations of unsaturated flow processes [*Beven*, 1995; *Vereecken et al.*, 2007]. These problems make small-scale information about soils and hydraulic parameters nearly impossible to use in real-world upscaling approaches [*Vereecken et al.*, 2007]. The limitations of such "bottom-up" approaches have led to instead using calibration to select parameters. This "top-down" strategy does not depend on knowledge of soil classes within the model domain [*Ines and Mohanty*, 2009].

The calibration process matches modeled outputs to observations of those fluxes or states by adjusting model parameters, and it has been shown to improve model performance [*Franks and Beven*, 1997; *Gupta et al.*, 1999; *Hogue et al.*, 2006; *Gutmann and Small*, 2010; *Harrison et al.*, 2012]. Studies to-date have used runoff, soil temperature, and heat fluxes to calibrate hydrologic model parameters [*Sorooshian et al.*, 1993; *Yapo et al.*, 1996; *Franks and Beven*, 1997; *Crow et al.*, 2003; *Hogue et al.*, 2005; *Liu et al.*, 2005; *Gutmann and Small*, 2007, 2010; *Nandagiri*, 2007].

With a given model and observation set, calibration schemes differ in the number of included parameters. Studies such as *Gutmann and Small* [2010], *Burke et al.* [1998], and *Santanello et al.* [2007] estimate only two to five parameters, which allows them to evaluate the role of each on the observed response. *Gupta et al.* [1999], *Houser et al.* [2001], and others, on the other hand, allow for complex interactions between parameters by simultaneously calibrating a dozen or more. *Bastidas et al.* [2006], however, find overparameterization in complex models, which decreases parameter identifiability. To this point, *Beven* [1989] points specifically to "making use of measured internal state variables" such as soil moisture as a path towards reducing "equifinality": that different parameter sets can produce equally good simulations [*Beven and Binley*, 1992].

Soil moisture observations are particularly well-suited for LSM model calibration, as they capture a key component of hydrologic behavior. Due to data availability, past calibration experiments have only utilized soil moisture observations in a small domain or in combination with other data [e.g., *Mattikalli et al.*, 1998; *Wooldridge et al.*, 2003; *Koren et al.*, 2008; *Ines and Mohanty*, 2009; *Pauwels et al.*, 2009; *Milzow et al.*, 2011; *Harrison et al.*, 2012]. The present work calibrates a hydrologic model to two large-scale observations of near-surface soil moisture: (1) basin-averaged *in situ* measurements, and (2) remotely-sensed observations from the ESA's SMOS satellite mission. Multi-year data are available for both. Because soil moisture alone has never been used to calibrate a model at this temporal and spatial scale, we limit our study to only four parameters that directly affect soil moisture. This is the logical first step before expanding to secondary parameters and interactions. We address the following questions: (1) What aspects of modeled soil moisture can be improved through calibration of SHPs with soil moisture? (2) What are the strengths and weaknesses of using SMOS in such calibrations? To assess model calibration success, we investigate the resulting absolute soil moisture values and soil moisture anomalies. Absolute values affect the magnitude of other model fluxes such as LHF and runoff [*Betts et al.*, 1996; *Entekhabi et al.*, 1996]. Soil moisture anomalies are useful for characterizing system dynamics [e.g., *Kurc and Small*, 2004] and for assimilation efforts [e.g., *Reichle and Koster*, 2004; *Crow et al.*, 2010; *Juglea et al.*, 2010; *Pan et al.*, 2012; *Blankenship et al.*, 2014].

2.2 Methods

The model setup mimics that of the Noah LSM [*Chen and Dudhia*, 2001; *Ek et al.*, 2003] in Phase 2 of the North American Land Data Assimilation System (NLDAS-2) [*Xia et al.*, 2012b]. This framework allows our results to be directly applicable to ongoing NLDAS and NLDAS-type research. The calibration process uses observations that are roughly commensurate with the 1/8 degree (approximately 144 km^2) NLDAS resolution, so soil moisture scaling is not part of this study.

2.2.1 Model, parameters, and forcing data

We employ the widely-used Noah LSM version 3.3 [*Chen and Dudhia*, 2001; *Ek et al.*, 2003]. Noah is run in a stand-alone configuration, although it can be coupled directly to an atmospheric model [*Skamarock et al.*, 2008]. The soil thickness is set to the default 2 m, with layer boundaries at 10, 40, 100, and 200 cm. Noah solves the Richards equation [*Richards*, 1931] to simulate the soil moisture content of each layer through time and allows gravity drainage from the bottom soil layer. The Richards equation is presented here as in Chen et al. [1996]:

$$\frac{\partial \theta}{\partial t} = \frac{\partial}{\partial z}\left[K\left(\frac{\partial \psi}{\partial \theta}\right)\frac{\partial \theta}{\partial z}\right] + \frac{\partial K}{\partial z} + F_{\theta} \tag{1}$$

θ is the volumetric soil moisture (VSM) content in m^3 m^{-3} (or cm^3 cm^{-3}), t is time in s, z is depth in m, and F_θ represents the sum of sources (positive) and sinks (negative) in cm^3 cm^{-3} s^{-1}: infiltration into and evaporation from layer 1, and transpiration from layers that contain roots. The remaining variables K and ψ are the hydraulic conductivity (m s^{-1}) and water tension (m H_2O). Noah uses the Campbell model to define their nonlinear behavior [*Campbell*, 1974]:

$$\psi = \psi_{sat}\left(\frac{\theta}{\theta_{sat}}\right)^{-b} \tag{2}$$

$$K = K_{sat}\left(\frac{\theta}{\theta_{sat}}\right)^{2b+3} \tag{3}$$

The four parameters in the above equations are SHPs (Table 1): (1) the inverse of the pore size distribution index, b (unitless), which defines the shape of the relationship between water tension and water content; (2) the saturated soil moisture content, θ_{sat} ($cm^3\ cm^{-3}$); (3) the saturated matric potential, ψ_{sat} (m H_2O), which is the water tension at which air enters a saturated volume of soil; and (4) the saturated hydraulic conductivity, K_{sat} ($m\ s^{-1}$).

Table 1. SHP parameters, their limits, and the ranges of their texture-based default values.

Parameter			Uniform prior distribution		Noah default values	
Name	Symbol	Units	Minimum	Maximum	Minimum	Maximum
Inverse of pore size distribution index	b	–	0.34	50.91	2.79	11.55
Saturated soil moisture content	θ_{sat}	$cm^3\ cm^{-3}$	0.12	0.698	0.339	0.476
Saturated matric potential	ψ_{sat}	m H_2O	0.036	4.01	0.036	0.759
Saturated hydraulic conductivity	K_{sat}	$m\ s^{-1}$	9.74E-07	1.51E-04	9.74E-07	4.66E-05

Through Eq. (1) – (3), SHPs directly affect the flux of water between Noah's soil layers. Each parameter controls one or more aspect of the simulated soil moisture time series. For example, higher K_{sat} enhances gravity-driven flow, which can result in drier surface soil. Nonlinear interactions between parameters exist, which is one reason why formal calibration schemes may be superior to manual selection of parameter values [*Boyle et al.*, 2000]. Prior studies with Noah demonstrate that soil moisture and heat fluxes are sensitive to all four SHPs, whether on their own or through interactions with other parameters [*Bastidas et al.*, 2006; *Rosero et al.*, 2010].

We use hourly NLDAS-2 meteorological forcings [*Xia et al.*, 2012b]. Default model parameters are either constant or are chosen according to soil texture and vegetation (Table 2). STATSGO-based soil textures and a lookup table from Cosby et al. [1984] provide Noah with its four SHPs at each location [*Miller and White*, 1998; *Mitchell et al.*, 2004]. Noah's vegetation parameters are chosen according to the location's University of Maryland 1 km Land Cover Classification, based on AVHRR data from 1981 to 1994 [*Hansen et al.*, 2000]. These consist of rooting depth, minimum and maximum leaf areas, emissivity, albedo, roughness height, and canopy stress parameters. The fractional cover of green vegetation, *shdfac*, is set to its monthly climatological average from NLDAS Noah forcings between 1979 and 2014.

Table 2. Site descriptions.
S: sand, L: loam, Si: silt, C: clay. CGM: Cropland/grassland mosaic, WG: wooded grassland. "Soil probes" are the number of available probes at 5 cm depth during 2012 and 2013. "Mean veg cover" is the average of the monthly climatological shdfac values used in the simulations. "Precip" is average annual precipitation from 2011-2013 NLDAS forcings.

Site	State	Abbrev	Lat	Lon	Mapped soil type	Vegetation	Mean veg cover	Precip (mm)	Soil probes	Approx km^2	Climate	Topo
Fort Cobb	OK	FC	35.34	-98.57	SiL	CGM	0.45	606	15	813	Sub-humid	Rolling
Marena	OK	Mar	36.06	-97.22	SL	WG	0.45	774	4	1	Sub-humid	Rolling
Little Washita	OK	LW	34.88	-98.07	SL	Grassland	0.44	773	15	610	Sub-humid	Rolling
St. Josephs	IN	SJ	41.44	-85.03	SiL	CGM	0.41	780	13	300	Humid	Flat
Walnut Gulch	AZ	WG	31.63	-110.40	L	Grassland	0.22	320	14	148	Semi-arid	Rolling
Little River	GA	LR	31.40	-83.56	LS	CGM	0.50	1333	8	334	Humid	Flat

Reynolds Creek	ID	RC	43.18	-116.78	L	Grassland	0.20	346	11	238	Semi-arid	Mountainous

2.2.2 Study sites and soil moisture observations

Seven sites are used (Table 2): Marena, OK (Mar); Walnut Gulch, AZ (WG); Little Washita, OK (LW); Fort Cobb, OK (FC); Little River, GA (LR); St. Josephs, IN (SJ); and Reynolds Creek, ID (RC). At each, surface soil moisture data are available from: (1) a network of *in situ* probes operated by the United States Department of Agriculture Agricultural Research Service (USDA–ARS), and (2) the ESA's SMOS satellite mission [*Kerr et al.*, 2010b]. Soil moisture is reported as VSM ($cm^3\ cm^{-3}$), representing the ratio between volume of water and total soil volume.

A primary goal of these *in situ* networks is calibration and validation of satellite products. Each has a distributed network of Stevens Water Hydra Probes placed at 5 cm depth and an up-scaling function that qualifies it for use at the 36 km scale [*Colliander et al.*, 2015]. The networks' "basin" average thus is representative of a passive microwave satellite footprint [*Jackson et al.*, 2010]. Supporting studies have determined most of the networks (WG, LW, LR, RC) to represent soil moisture with high accuracy (~0.01 $cm^3\ cm^{-3}$) from 0 to 5 cm [*Bosch et al.*, 2006; *Cosh et al.*, 2006, 2008; *Jackson et al.*, 2012]. FC has been shown to perform well in a multiyear stability study, though it has not been explicitly validated [*Cosh et al.*, 2014]. SJ is still under development, but its design and instrumentation are similar to the other sites.

Each sites' 5 cm *in situ* averages are used for SHP calibration. When available, we also use probes from lower in the soil column to evaluate performance of the calibrated models. Five of the seven sites have deeper probes. We assign these to represent the second model layer (10 to 40 cm) as follows: when two probes fall within the second model layer, they are averaged. When only one exists, it represents the entire layer. For both soil layers, multiple probe locations contribute to the network's average. Observations are recorded hourly, but for direct comparison with SMOS observations, only 0600 LT (local time) observations are used each day. Hereafter, "*in situ*" VSM refers to the daily, network-averaged soil moisture.

SMOS uses a passive, synthetic aperture, L-band radiometer to retrieve soil moisture every ~3 days with spatial resolution of ~1200 km^2 [*Jackson et al.*, 2012]. The radiometer measures microwave brightness temperature, which is then converted into a soil moisture value according to the relationship outlined by Jackson and Schmugge [1989] and detailed in Kerr et al. [2010a]. Vegetation affects the retrievals, but corrections for vegetation are possible when vegetation water content is less than 5 kg m^{-2} [*Kerr et al.*, 2010b]. SMOS has a sun-synchronous orbit, which passes over the equator at approximately 0600 LT (ascending) and 1800 LT (descending). The SMOS algorithm's underlying equations are based on an assumption of uniform soil moisture and soil/vegetation temperature over the sensing depth. The ground surface is closest to meeting this assumption when it has had maximal time to equilibrate from the previous day's fluxes [*Jackson*, 1980; *Jackson et al.*, 2012]. We therefore use the ascending (0600 LT) level 3 soil moisture data, which are provided by the Centre Aval de Traitement de Données SMOS.

2.2.3 Calibration strategy and experiments

The general format for model calibration to a single observational time series has been detailed in *Vrugt et al.* [2008]. We calibrate the four SHPs in Table 1. Posterior distributions have limited sensitivity to prior distributions [*Harrison et al.*, 2012], so for simplicity, priors are taken to be uniform between two bounds. We use similar parameter ranges to those used by *Harrison et al.* [2012], except that the ranges of ψ_{sat} and K_{sat} priors are narrowed to avoid unrealistic layer two soil moisture contents observed in some preliminary experiments. The range of parameter values in the calibration scheme is purposefully larger than the range of mean values used in default Noah simulations (Table 1). This allows for increased parameter diversity and potential advantages to calibrated values.

We calibrate SHPs by minimizing the differences between surface soil moisture observations and simulations. We quantify their differences with an objective function (OF), which we choose to be root mean squared difference (RMSD), Eq. (4).

$$RMSD = \sqrt{\frac{\sum\left(VSM_{sim} - VSM_{obs}\right)^2}{n}} \tag{4}$$

sim and obs indicate the simulated and observed VSM, respectively, and n is the number of days that both are available. RMSD is used in many hydrologic calibration studies [*Burke et al.*, 1997; *Gupta et al.*, 1998; *Santanello et al.*, 2007; *Peters-Lidard et al.*, 2008; *Gutmann and Small*, 2010; *Harrison et al.*, 2012] and is a convenient way to measure dispersion of the model residual around zero [*Gupta et* *al.*, 1998]. As in *Albergel et al.* [2012], we use the terminology RMS difference, instead of RMS error, because observations do not represent true soil moisture.

We use the differential evolution adaptive Metropolis (DREAM) algorithm to search the parameter space using 50,000 – 100,000 model simulations [*Vrugt et al.*, 2008, 2009]. Each simulation is two years long: a calibration year (2012) following a 1-year spinup (2011). The spinup is sufficiently long for Noah SHP calibration purposes [*Gutmann and Small*, 2010]. The exact number of simulations depends on the $\hat{R}$ statistic of Gelman and Rubin [1992], indicating convergence to a stationary posterior distribution. We ensure at least 2,500 additional model simulations after convergence to characterize the posterior distributions of the parameters in each experiment. Simulations from converged parameter sets are run for an additional year (2013) for validation against *in situ* soil moisture.

The DREAM algorithm's lineage includes the SCE-UA and SCEM-UA parameter estimation algorithms [*Duan et al.*, 1992; *Vrugt et al.*, 2003]. It is distinct in its ability to provide posterior parameter distributions, which we use to quantify uncertainty in our analyses.

At each study site, both *in situ* and remotely-sensed surface soil moisture observations are available. With these two sources, we produce three calibration experiments:

(1) "*in situ*": Minimize the OF between simulated and *in situ* surface soil moisture. The calibration and validation observations are from the same

soil probes. This experiment therefore provides an upper limit to model performance at each site in the validation period.

(2) "SMOS": Minimize the OF between simulated and remotely-sensed soil moisture from the SMOS pixel centered on each field site.

(3) "$SMOS_{adj}$": Minimize the OF between simulated soil moisture and a bias-free SMOS product: the SMOS soil moisture time series has been adjusted through a translation of the observations so that the mean of the 2012 SMOS and *in situ* observations are equal. Bias removal is completed on a site-by-site basis. In the rare cases when a shifted moisture value would drop below zero, it is limited to zero. This experiment shows the potential of a bias-free SMOS time series in our calibration framework.

Our experiments produce posterior distributions for each parameter. The single best parameter set is that whose simulation produces the maximum a posteriori probability (MAP; in this case, lowest RMSD) in the calibration period. The associated model run is referred to as the calibrated simulation.

2.2.4 Texture-based simulations

A site's soil texture designation (and thus SHPs) may differ between global maps, local maps, and site observations [*Guillod et al.*, 2013; *Xia et al.*, 2015]. We therefore carry out simulations using all 12 possible texture designations at each site. These parameter sets and their resulting simulations are hereafter called "texture-based." They allow us to illustrate the range of states and fluxes that are possible for a given location using the current parameterization strategy. At each site, we highlight two of these texture-based simulations:

(1) The default texture: that which is used by NLDAS simulations.

(2) The best texture: that which minimizes the RMSD between simulated and *in situ* surface VSM in the calibration period.

The best texture simulation allows the calibration results to be compared with those of an improved texture. We acknowledge that the best texture cannot be determined in this fashion at sites that do not have soil moisture instrumentation.

2.2.5 Assessment of model calibrations

We use:

(1) RMSD between simulated and *in situ* VSM. While the *in situ* soil moisture is not without its own measurement and averaging errors, it is our only proxy for the true surface soil moisture.

(2) The arithmetic mean of VSM time series. This metric provides insight into how minimizing RMSD affects moisture biases.

(3) RMSD between simulated and *in situ* VSM anomalies (unbiased RMSD, or "ubRMSD"). UbRMSD provides a measure of how well each simulation captures soil moisture dynamics. We calculate ubRMSD both for the validation year as a whole ("year-long ubRMSD") and on a moving 90-day window throughout the validation period ("windowed ubRMSD"). The latter method identifies the time periods when calibration yields the greatest improvements.

2.2.6 Study limitations and sources of error

2.2.6.1 Representativeness and accuracy of data products

Soil moisture variability increases with scale, so representative basin-wide *in situ* values require many observations [*Famiglietti et al.*, 2008]. The monitoring sites used in this study are the best available, but they cannot be perfect. Moreover, results from Mar must be considered differently. The probe type and installation depth match the other sites, but Mar only includes four sensors distributed across a 1 km^2 area. We include this location to identify what useful information (if any) can be gleaned from a site whose representative area is intermediate between a remotely-sensed pixel and a single probe.

The SMOS mission's target accuracy of 0.04 cm^3 cm^{-3} RMSD is not met at all sites. In 2010, at WG, LW, LR, and RC, RMSD values were 0.038, 0.042, 0.051, and 0.039 cm^3 cm^{-3}, and biases were 0.003, 0.002, 0.026, and -0.023 cm^3 cm^{-3}, respectively [*Jackson et al.*, 2012]. Elsewhere in North America, SMOS biases of up to -0.12 cm^3 cm^{-3} have been documented [*Al Bitar et al.*, 2012; *Albergel et al.*, 2012; *Collow et al.*, 2012].

In situ, remotely-sensed, and modeled depths are not identical. The 5 cm *in situ* probes measure over a depth of approximately 3 to 7 cm. This is similar to the first model layer, 0 to 10 cm. The correspondence between remotely-sensed and modeled VSM is not as exact. SMOS retrieval depth is approximately 5 cm. However, the sensing depth decreases after rainfall when the surface layer is nearly saturated and increases to more than 5 cm when the soil is dry [*Jackson et al.*, 2012]. To assess the significance of this difference, we have completed our parameter estimation analysis with the Noah layer 1 thickness set to 0-5 cm instead of 0-10 cm. We find this change leads to trivial differences in both simulated soil moisture time series and parameter distributions. We continue with 0-10 cm thickness to avoid modifying the standard model setup and to make our findings directly applicable to NLDAS Noah simulations. Finally, we note that the spatial resolution of NLDAS-2 is finer than that of SMOS (Figure 1). Mar, as mentioned above, is of a different spatial scale.

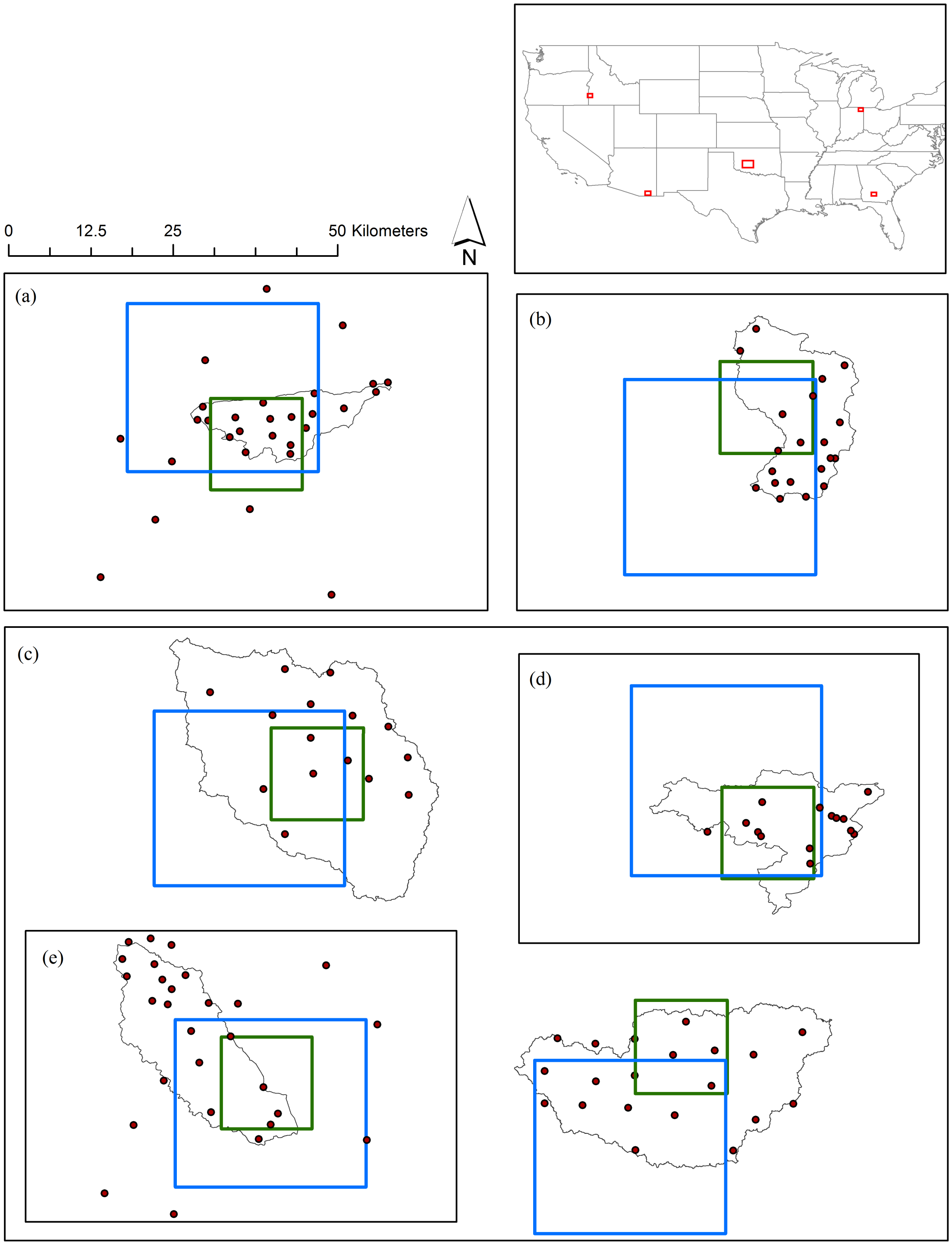

Figure 1: The spatial coverage of *in situ*, SMOS, and NLDAS for all sites except Mar.

2.2.6.2 Calibration scheme

Adjusting specific parameters can compensate for errors in other parameters, model structure, or input data [*Doherty and Welter*, 2010]. The DREAM algorithm limits the user to one OF, which has weaknesses compared to multi-objective schemes: calibration can lead to compensating biases in other aspects of the system, such as LHF and runoff [*Gupta et al.*, 1999; *Salvucci and Entekhabi*, 2011; *Wöhling et al.*, 2013]. In turn, changes to LHF of 15 to 20 W m^{-2} can have a significant impact on atmospheric processes [*Schär et al.*, 1999]. Despite these disadvantages, we wish to study the potential of SMOS soil moisture in a single-objective scheme before combining it with other constraining states or fluxes. We lack observations of surface runoff, baseflow, and LHF, so a comprehensive evaluation of all model fluxes is admittedly not possible. However, these are high-quality soil moisture networks and thus provide unique and powerful constraints on SHPs. We supplement the validation by qualitatively assessing the effects that calibrated parameter sets have on discharge and LHF.

Even a model with ideal parameters may have structural inadequacies and meteorological forcing errors. The latter has been shown to account for 20% to 60% of soil moisture prediction uncertainty [*Hossain and Anagnostou*, 2005]. Finally, parameters selected through calibration are not easily transferable to other scales or ungauged locations [*Liang et al.*, 2004; *Troy et al.*, 2008]. To mitigate these problems, we have included a variety of locations in this study, and as discussed above, *in situ* scales are roughly commensurate with forcing data.

2.3 Results

2.3.1 Improvement of surface soil moisture

Surface VSM results are exclusively from the validation period and compare simulations with *in situ* observations.

2.3.1.1 RMSD

Figure 2 shows an example of the calibration results at SJ. We include soil moisture time series from the three calibrations as well as the 12 texture-based simulations. The site's default soil texture, silty loam, is far from the best: RMSD is 0.059 $cm^3\ cm^{-3}$. Five other textures yield better soil moisture simulations. The best texture is sandy loam, with a RMSD of 0.048 $cm^3\ cm^{-3}$. Thus, by changing the soil texture designation, we can reduce model error by nearly 20%. Similar results are found at all seven sites (Figure 3, Table 3). At no site is the default texture the same as the best texture. RMSDs for the default simulations range from 0.03 to 0.11 $cm^3\ cm^{-3}$ (mean 0.07 $cm^3\ cm^{-3}$). If the best texture were used at each site, error would decrease by an average of 0.03 $cm^3\ cm^{-3}$, bringing all but the RC simulation below 0.05 $cm^3\ cm^{-3}$, the low end of the RMSD range found in default simulations by *Xia et al.* [2015]. Such improvement from switching soil type reflects a general failure of using mapped soil texture to select SHPs but not necessarily a problem with the 12 texture-based parameter sets themselves.

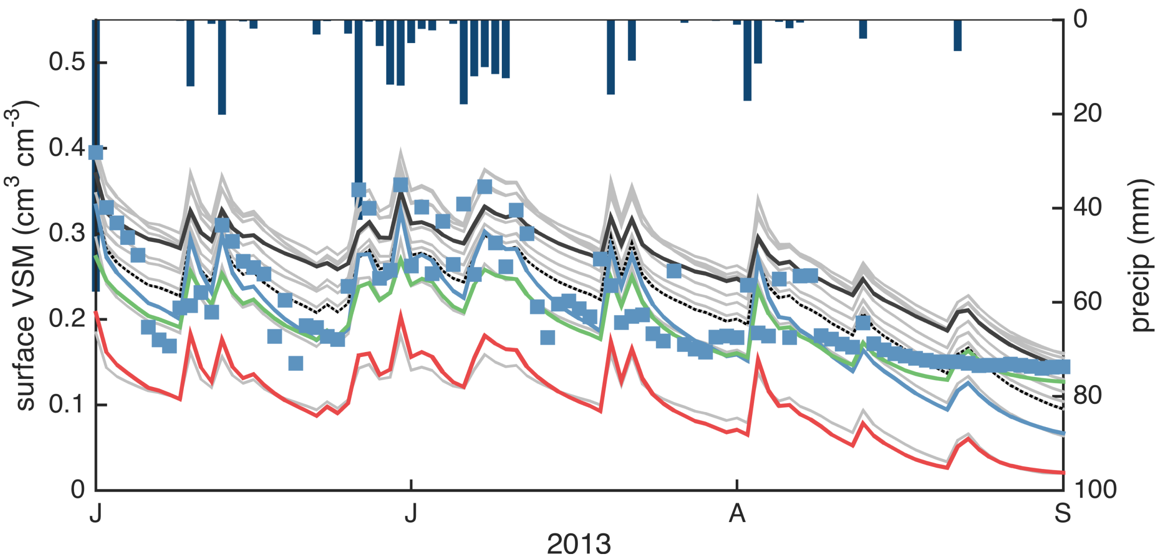

Figure 2: An example time series at SJ.
Shown are the basin-averaged *in situ* surface soil moisture measurements (blue squares), the texture-based simulations (gray lines), the default simulation (silty loam, black line), the best texture simulation (sandy loam, black dotted line), and the three calibrated timeseries (blue: *in situ*; red: SMOS; green: $SMOS_{adj}$). Precipitation is shown in dark blue.

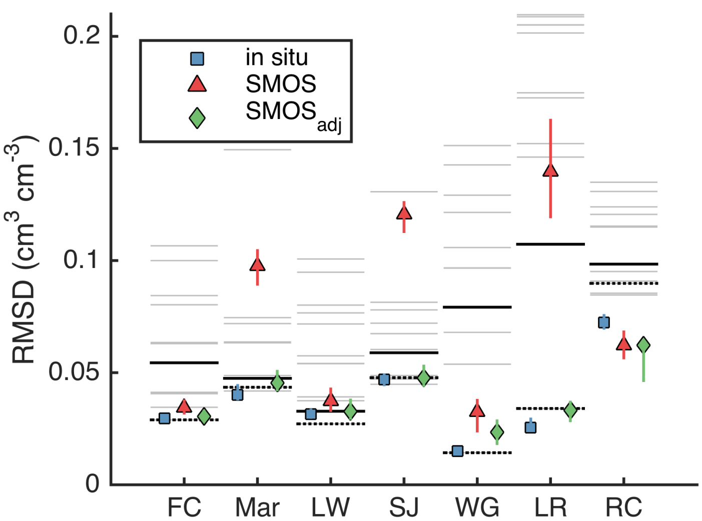

Figure 3: RMSD between simulations and *in situ* soil moisture
at each site in the validation period. Simulations include texture-based (gray lines), default (solid black lines), best texture (dotted black lines), *in situ* calibrated (blue squares), SMOS calibrated (red triangles), and $SMOS_{adj}$ calibrated (green diamonds). Error bars show the range of performances from each calibration's stable posterior parameter distribution.

As expected, calibration to *in situ* observations improves simulated soil moisture. For example, the best *in situ* calibrated soil moisture time series at SJ (blue line, Figure 1) more closely follows the *in situ* observations than the default simulation does. Across all sites, RMSD improves by an average of 0.03 cm^3 cm^{-3}. All but RC are brought below 0.05 cm^3 cm^{-3}. The improvements from *in situ* calibration at each site are only slightly better than the improvements made by replacing the default soil texture with the best texture. At sites where the default simulation performs well (Mar and LW), calibration changes the RMSD very little. Equally important, these best sites are not made worse through calibration. Sites with poor default simulations benefit the most from calibration (WG, LR, and RC).

Calibration to SMOS observations does not consistently improve RMSD. At SJ, the SMOS calibrated soil moisture is far below the *in situ* observations (red line, Figure 2). FC, WG, and RC are improved through SMOS calibration (Figure 3, Table 3), but an equal number are made worse (Mar, SJ, LR). The average change to RMSD is close to zero.

Table 3. RMSD between simulations and observed *in situ* soil moisture during the validation period. For readability, all values are expressed as hundredths of cm^3 cm^{-3} (divide by 100 for actual values). Change (Δ) is with respect to the default simulation. Bold indicates improvement of at least 0.005 cm^3 cm^{-3} (or 0.5 in the table); italics indicate degradation of at least 0.005 cm^3 cm^{-3}. S: sand, L: loam, Si: silt, C: clay.

	Default texture		Best texture			*in situ*		SMOS		$SMOS_{adj}$	
Site	Class	RMSD	Class	RMSD	Δ	RMSD	Δ	RMSD	Δ	RMSD	Δ
FC	SiL	5.4	LS	2.9	**-2.5**	3.0	**-2.5**	3.4	**-2.0**	3.0	**-2.4**
Mar	SL	4.8	SCL	4.4	**-0.4**	4.0	**-0.7**	9.8	*5.0*	4.6	-0.2
LW	SL	3.3	LS	2.7	**-0.6**	3.2	-0.1	3.7	0.5	3.3	0.0
SJ	SiL	5.9	SL	4.8	**-1.1**	4.7	**-1.2**	12.1	*6.2*	4.8	**-1.1**
WG	L	7.9	S	1.4	**-6.5**	1.5	**-6.4**	3.3	**-4.7**	2.3	**-5.6**
LR	LS	10.7	S	3.4	**-7.3**	2.6	**-8.2**	14.0	*3.3*	3.3	**-7.4**
RC	L	9.8	LS	9.0	**-0.0**	7.2	**-2.6**	6.2	**-3.6**	6.2	**-3.6**
Mean		6.8		3.9	**-2.8**	3.7	**-3.1**	7.5	**0.7**	3.9	**-2.9**

At all seven sites, calibration to $SMOS_{adj}$ observations results in a lower RMSD than the default simulations (Figure 3, Table 3). The average improvement is 0.03 cm^3 cm^{-3}. At SJ, the $SMOS_{adj}$ calibrated simulation (green line, Figure 2) is better than the default and SMOS calibrated simulations. Like simulations calibrated to *in situ*, the sites already performing well (Mar and LW) maintain their good performance when calibrated to $SMOS_{adj}$.

While RMSD establishes model error, it does not explicitly address how well model variability matches observations. To this end, we have calculated R^2 values for all simulations shown in Figure 3, and the results are effectively the same (Figure 4). Error improvement, when present, is also bringing an improvement to modeled variability.

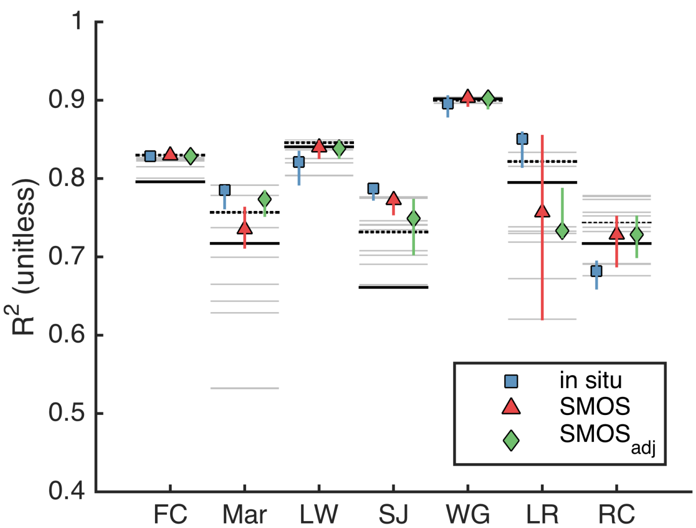

Figure 4: As in Figure 3, but showing R^2 between simulations and *in situ* soil moisture.

2.3.1.2 Mean VSM

Figure 5a shows how the mean VSM of each simulation compares with the mean of the *in situ* observations. For all texture-based and calibrated simulations except RC, the closer the match between simulated and observed mean VSM, the lower the RMSD is. In this light, it is not surprising that the SMOS retrievals cannot be used to successfully select SHPs, since the SMOS retrievals often have biases with respect to the *in situ* observations. Sites whose SMOS calibrated simulations have a greater RMSD than default simulations are Mar, SJ, and LR. They also have the worst SMOS biases: -0.064, -0.101, and 0.136 $cm^3\ cm^{-3}$, respectively. SMOS biases at FC, LW, WG, and RC are smaller: -0.008, -0.008, 0.013, and -0.049 $cm^3\ cm^{-3}$. At these sites, the SMOS and $SMOS_{adj}$ calibrations are similarly successful at reducing or not changing RMSD.

These results qualify the utility of SMOS data. The success of the $SMOS_{adj}$ calibrations is in large part due to their unbiased nature, a characteristic imposed on the calibration data by design prior to the experiment.

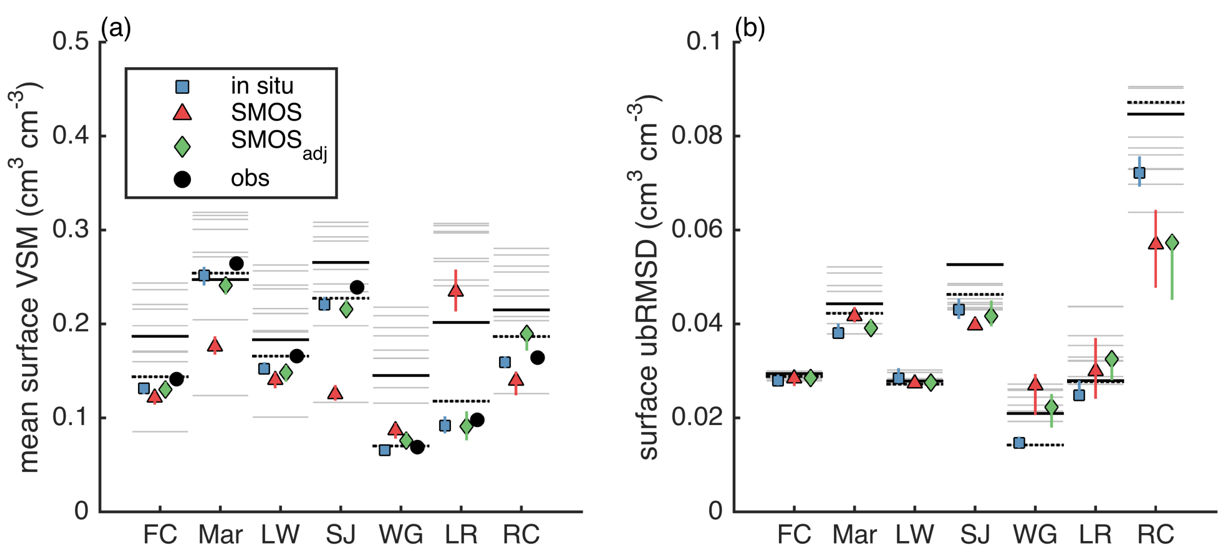

Figure 5: Mean VSM (a) and year-long ubRMSD in the surface layer (b).
Symbols and lines are as in Figure 3, with *in situ* observations also included as black circles.

2.3.1.3 UbRMSD

We must determine the value of SMOS observations independent of their biases. Figure 6 shows VSM anomalies. The model does not capture the wetting events near the end of June nor the drying period at the end of August, no matter what parameter set is used. We quantify such temporal dynamics in each simulated VSM time series using year-long and windowed ubRMSD.

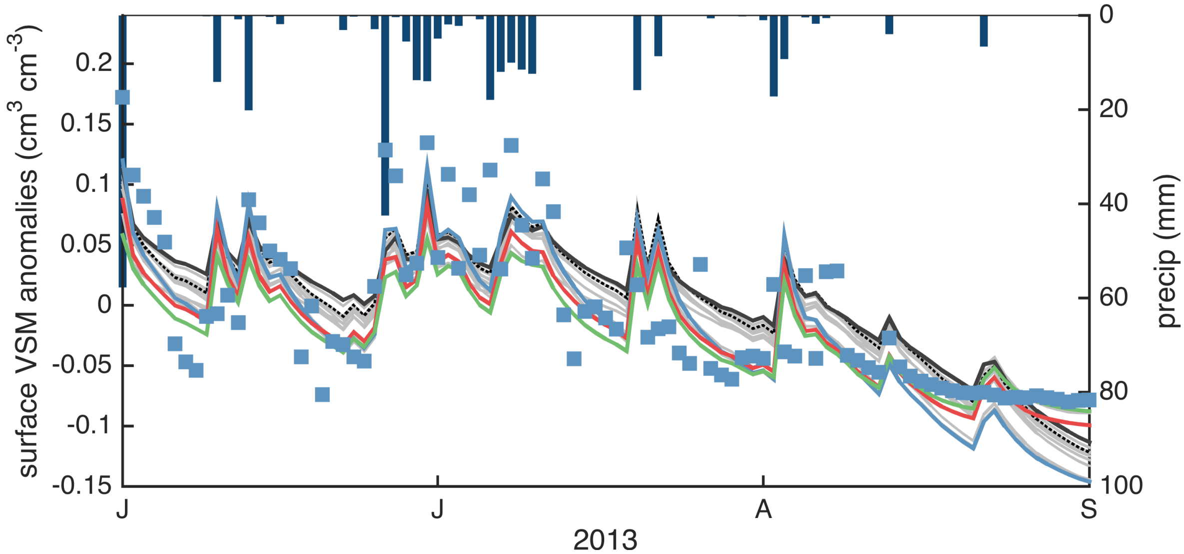

Figure 6: SJ. As in Figure 2, but with the mean of each time series removed.

We first summarize the year-long ubRMSD results (Figure 5b, Table 4). The best texture simulations do not minimize year-long ubRMSD at all sites. At Mar, SJ, and RC, a number of textures would have produced lower ubRMSDs than the best texture did. This failure indicates that minimization of RMSD does not require minimization of ubRMSD. It only requires a good match between mean values of the time series.

Table 4. UbRMSD between simulations and observed *in situ* soil moisture during the validation period. For readability, all values are expressed as hundredths of $cm^3\ cm^{-3}$ (divide by 100 for actual values). Change (Δ) is with respect to the default simulation. Bold indicates improvement of at least 0.005 $cm^3\ cm^{-3}$; italics indicates degradation of at least 0.005 $cm^3\ cm^{-3}$.

	Default texture	Best texture		*in situ*		SMOS		$SMOS_{adj}$	
Site	ubRMSD	ubRMSD	Δ	ubRMSD	Δ	ubRMSD	Δ	ubRMSD	Δ
FC	2.9	2.9	-0.06	2.8	-0.15	2.8	-0.10	2.9	-0.09
Mar	4.4	4.2	-0.20	3.8	**-0.63**	4.2	-0.26	3.9	**-0.51**
LW	2.8	2.7	-0.06	2.8	0.06	2.7	-0.04	2.8	-0.03
SJ	5.3	4.6	**-0.63**	4.3	**-0.96**	4.0	**-1.29**	4.2	**-1.10**
WG	2.1	1.4	**-0.67**	1.5	**-0.62**	2.7	*0.60*	2.2	0.14
LR	2.8	2.8	-0.02	2.5	-0.31	3.0	0.20	3.3	0.46
RC	8.5	8.7	0.25	7.2	**-1.25**	5.7	**-2.78**	5.7	**-2.75**
Mean	4.1	3.9	-0.2	3.6	**-0.55**	3.6	**-0.52**	3.6	**-0.55**

Calibrated soil moisture curves at most sites either do not change or improve the year-long ubRMSD over the default simulation. In five experiments, calibrated simulations improve year-long ubRMSD more than any texture-based simulation can: SJ calibrated to *in situ* and $SMOS_{adj}$, LR calibrated to *in situ*, and RC calibrated to SMOS and $SMOS_{adj}$. In these cases, unlike in texture-based simulations, minimization of RMSD does not merely match simulated and observed mean VSM. It has the additional effect of improving soil moisture dynamics.

At the other extreme are FC and LW, whose calibrated and texture-based simulations all have the same year-long ubRMSD. Despite a wide range of RMSDs, all simulations have identical abilities to capture soil moisture dynamics. RMSD and the calibration process at these sites therefore depends entirely on the match with *in situ* mean VSM.

Changes to year-long ubRMSD are not large. The windowed ubRMSD however, exposes notable improvements to calibrated simulations' soil moisture dynamics. We see the largest improvements occurring at sites and times of year when the default simulation is worst. Figure 7 compares the default simulation's windowed ubRMSD to that of the three calibrated and best texture simulations at SJ. The default simulation has the highest ubRMSD around March and April, which are times of year when all three calibrated simulations show the largest improvements to windowed ubRMSD. The best texture simulation, on the other hand, has mixed, small effects on ubRMSD throughout the year, regardless of the default simulation's performance.

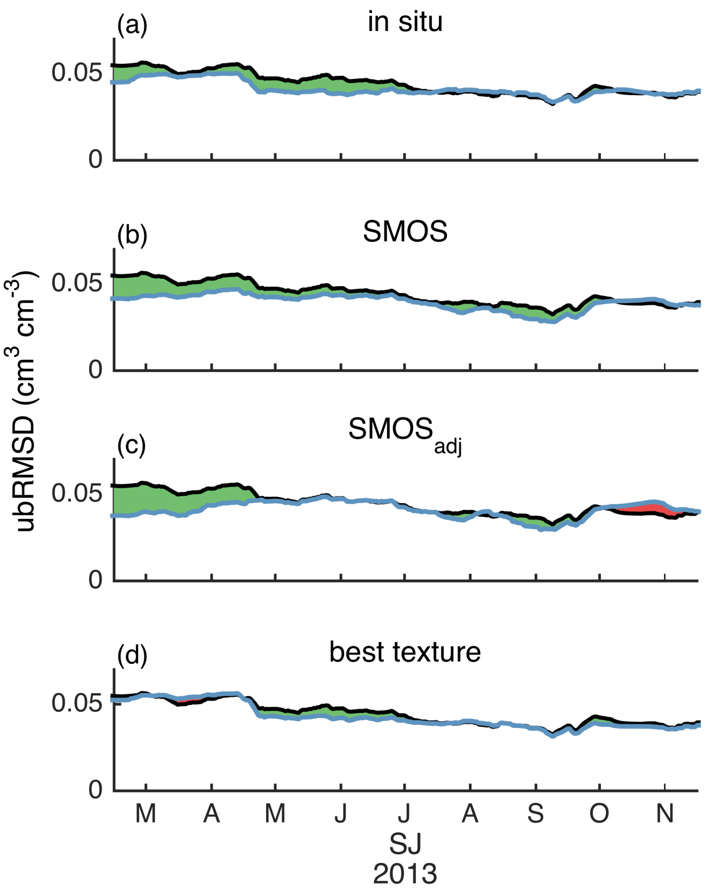

Figure 7: Windowed ubRMSD at SJ, from the *in situ* (a), SMOS (b), $SMOS_{adj}$ (c) experiments, and the best texture simulation (d).
Default simulation is shown in black. Calibrated and best texture simulations are shown in blue. Green shading highlights periods when the calibrated or best texture simulation is better than the default simulation. Red shading shows the reverse.

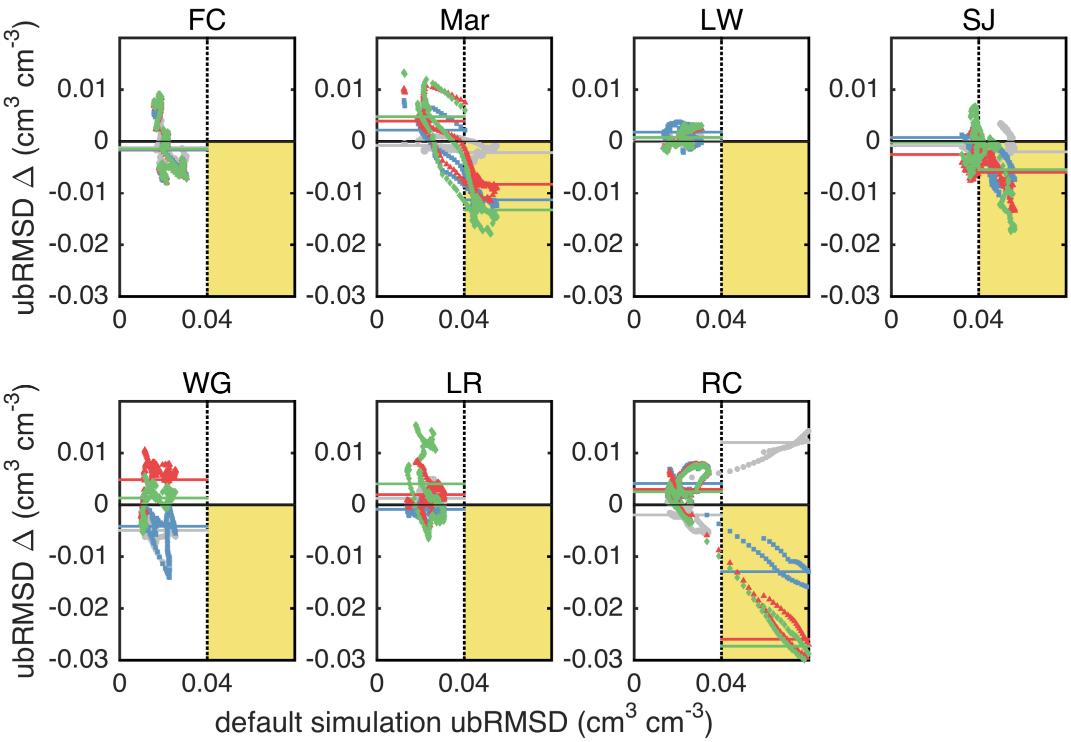

Figure 8: The default simulation's windowed ubRMSD and the change (Δ) that four alternative simulations can make:
in situ calibrated (blue squares), SMOS calibrated (red triangles), $SMOS_{adj}$ calibrated (greed diamonds), and best texture (gray circles). Dotted line shows 0.04 cm^3 cm^{-3} threshold. Colored horizontal lines show mean values on each side of the threshold. Yellow shading shows where the default is worst and can be improved.

Beyond SJ, improvements to ubRMSD are made at all sites and time periods when the default windowed ubRMSD is poor. In addition, ubRMSD is not made worse when the default simulation is good. In Figure 8, the x-axis shows the windowed ubRMSD of the default simulation for all validation days. The y-axis shows the changes that each calibration or best texture would make on each day (negative numbers indicate improvement). We use a black dotted line to define a threshold default ubRMSD at 0.04 cm^3 cm^{-3}. We average the windowed ubRMSD both below and above this threshold, shown with the solid colored lines. Below the threshold, where the default simulations are good, all calibrations have a mixed, small effect on ubRMSD. There are no increases greater than 0.005 $cm^3\ cm^{-3}$ at any site. Above the threshold, which is crossed at Mar, SJ, and RC, calibrated simulations have a lower ubRMSD than default simulations do, by as much as 0.026 $cm^3\ cm^{-3}$. We highlight this region of the plot by shading it yellow. In contrast, the best texture simulations do not improve ubRMSD at times when the default simulation is above the threshold. Improvement at Mar and SJ are present but small. At RC, the best texture is worse even than the default simulation.

2.3.2 Changes to other model states and fluxes

In this section, we describe the effects of calibration on deeper soil moisture, runoff, and LHF. Because none of these three variables were involved in calibration, the following results utilize modeled data from both the calibration and validation periods.

2.3.2.1 Deeper soil moisture

10 to 40 cm *in situ* data have not been verified as an accurate measurement of the second model layer's VSM. We therefore assess performance with ubRMSD (Figure 9a), which depends only on changes to soil moisture, not absolute VSM values. The best texture simulations have no consistent effect on layer 2 dynamics. FC, Mar, and LW stay the same, SJ is made worse, and LR is improved. Calibrated simulations do not harm the model's layer 2 dynamics and often slightly improve them. Only the *in situ* calibration at SJ is made worse.

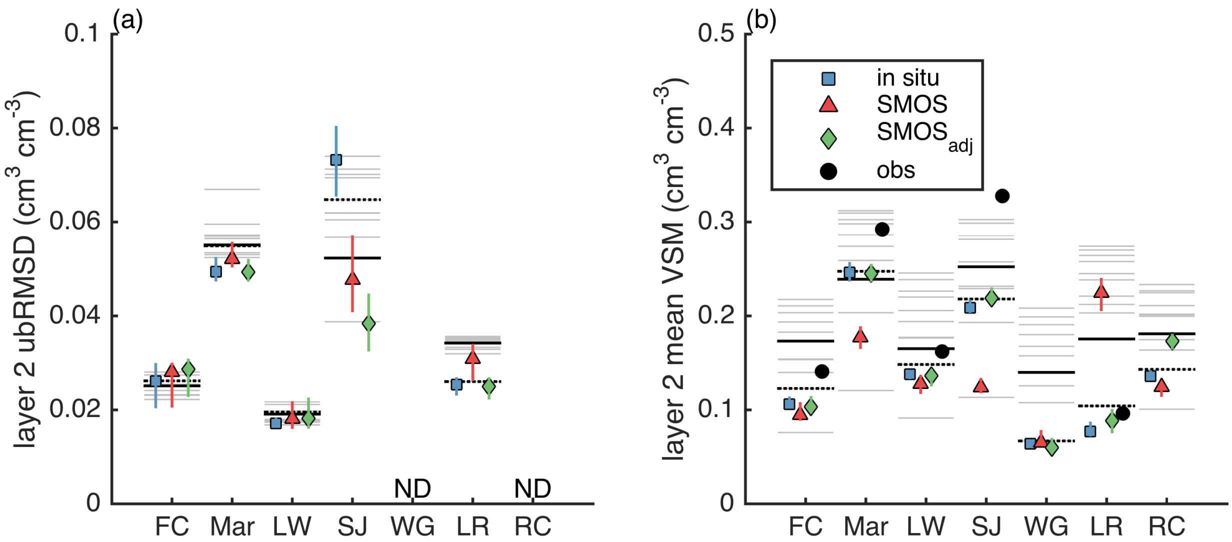

Figure 9: UbRMSD (a) and mean VSM (b) in model layer 2.
ND indicates no data is available below 10 cm. Symbols and lines are as in Figure 3, with *in situ* observations also included as black circles.

Figure 9b shows the mean layer 2 VSM for all simulations. The calibrated simulations produce drier layer 2 VSM than the default in all cases except the *in situ* and SMOS$_{adj}$ calibrations at Mar, and the SMOS calibration at LR. The best texture simulations also decrease mean layer 2 moisture at all sites except Mar. The deeper (third and fourth) soil layers are similarly affected (not shown). For reference, we also show the mean *in situ* soil moisture, which can be either drier or wetter than the default simulation, although these *in situ* observations cannot be considered as truth.

2.3.2.2 Runoff and LHF

Conservation of mass requires that changes to soil moisture magnitudes and dynamics be associated with changes in runoff and LHF. We look first at each site's surface runoff, subsurface runoff, and total runoff ratio (Figure 10). With only two exceptions (*in situ* at WG and SMOS$_{adj}$ at LR), calibrated simulations have more surface runoff than default simulations do. This change corresponds to an increase in the runoff ratio (total runoff / total precipitation) for all experiments except *in situ* and $SMOS_{adj}$ at Mar, and SMOS at LR, which have counteracting decreases in subsurface runoff. We include runoff ratios from all 12 texture-based simulations at each site to illustrate the range of values possible without calibration. The calibrated simulations are mostly at the high end of this range. In contrast, the best textures produce simulations whose runoff ratios are more often at the low end or in the middle of this range.

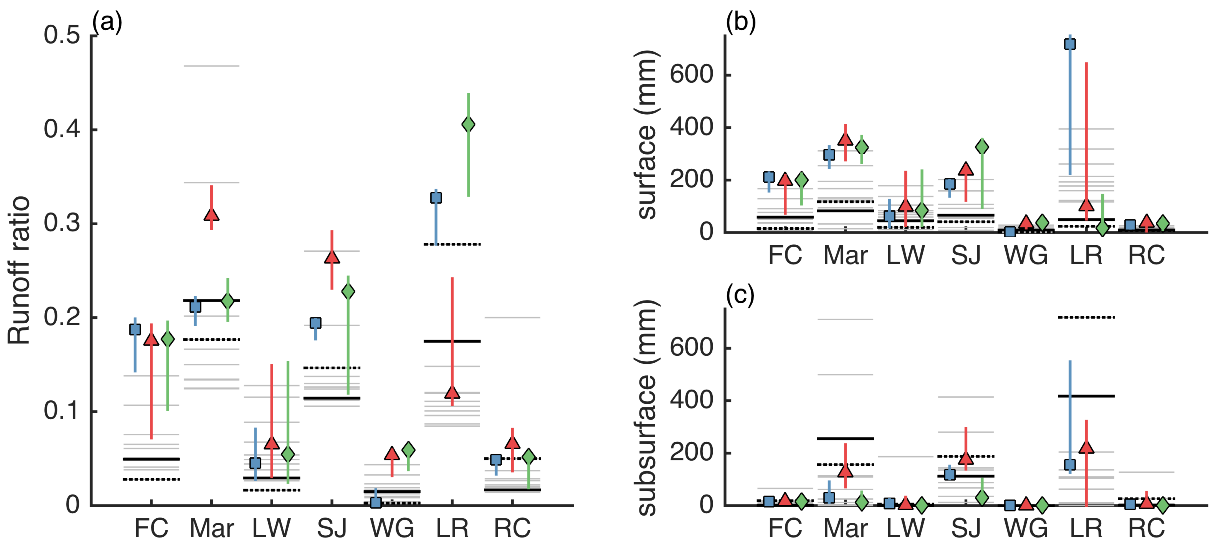

Figure 10: Runoff ratio (a) at each site for each calibration over 2012-2013. Corresponding volume of surface (b) and subsurface (c) runoff.
Symbols and lines are as in Figure 3. Subsurface runoff at LR calibrated to $SMOS_{adj}$ is off-scale, at 1065 mm.

Figure 11 shows the differences in each simulation's mean daily summertime LHF. We focus on summer because that is the season in which LHF is greatest. The range of LHF produced by the 12 texture-based parameters is generally less than 15 to 20 W m^{-2}, and the best texture is at most only 8.3 W m^{-2} different from the default simulation. On the other hand, three of the seven sites have significantly lower (>20 W m^{-2}) LHF values after calibration: FC, SJ, and LR. The remaining four sites have changes to LHF that are relatively small (less than 10 W m^{-2}). We do not have flux tower data at all sites to determine whether LHF should be much different from that of the default simulation. But together the increased surface runoff and decreased LHF data indicate that calibrated parameters allow less water to pass through the soil column during rainfall events.

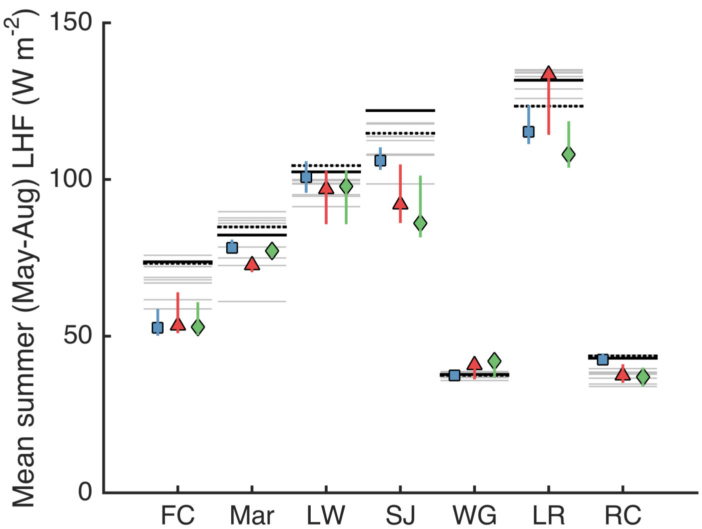

Figure 11: Mean summertime (May-Aug) LHF at each site for each calibration and texture-based simulation.
Symbols and lines are as in Figure 3.

2.3.3 Parameter values and trends

The DREAM algorithm, in addition to identifying a MAP value, produces a posterior probability distribution for each experiment. Similarly, *Cosby et al.* [1984] provide not only the mean of each texture class but also standard deviations. We illustrate the differences between each distribution for all four parameters in Figure 12 through 15. All default and calibrated parameter values are provided in Table 5.

At most sites, the calibrated θ_{sat} parameters (Figure 12), occupy a narrower range than they do in the laboratory measurements of *Cosby et al.* [1984]. Moreover, most MAP parameter values fall within the Gaussian distribution of the prescribed texture class, evidence that the calibrated parameter values are reasonable estimates.

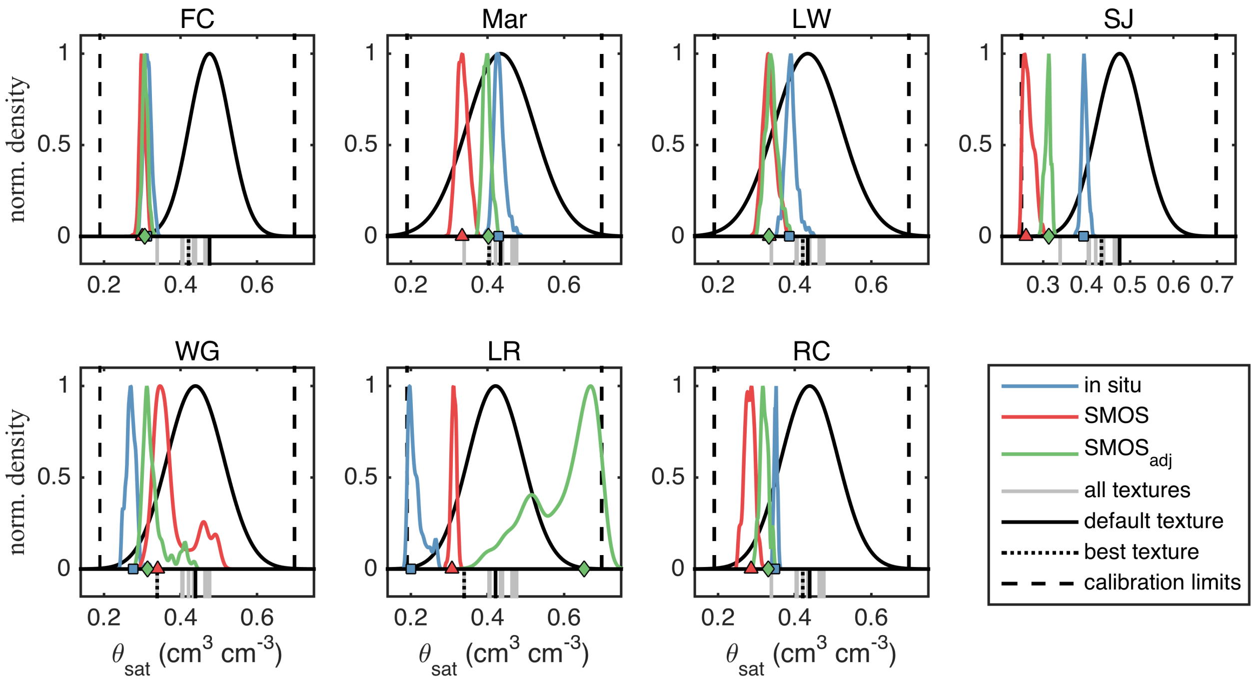

Figure 12: The distributions of the θ_{sat} parameter at each site.
Vertical dashed lines indicate the lower and upper constraints placed on the calibration algorithm. Normalized posterior probability density functions at each site for each calibration scheme are shown with colored curves. Laboratory-derived texture-based distributions are shown in black [*Cosby et al.*, 1984]. Markers on the x-axis show the MAP parameter values for the *in situ* (blue squares), SMOS (red triangles), and SMOS$_{adj}$ (green diamonds) calibrations. Along the bottom, gray bars show all texture-based parameter values, black bar shows default parameter value, and dotted bar shows the best texture value.

Most calibrated values for *b* are near the texture-based value (Figure 13). The calibration to SMOS$_{adj}$ at SJ and to SMOS at LR are both outliers, with *b* values of 20.85 and 50.88, respectively, which are off the scale shown.

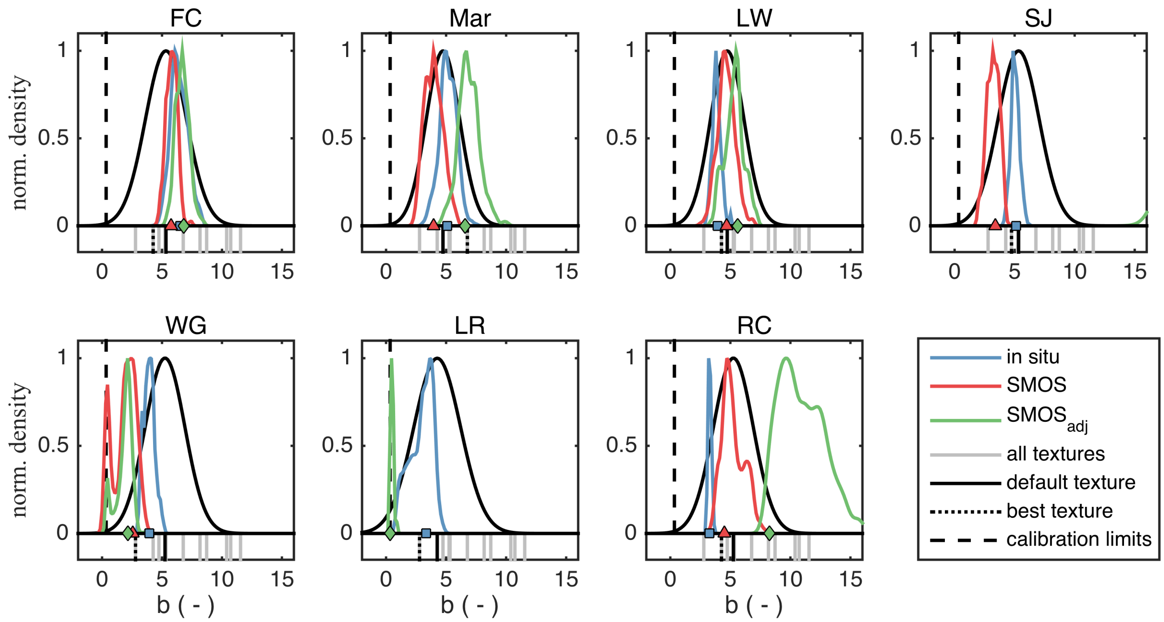

Figure 13: As in Figure 12, but for distributions of the *b* parameter.
The far-right range of this parameter space is not shown to better illustrate the region that most experiments occupy.

The calibrated posterior distributions for ψ_{sat} are not all well-defined (Figure 14). We observe multi-modal distributions in this parameter at all sites except for Mar. This indicates that surface soil moisture may be less sensitive to this parameter (consistent with *Bastidas et al.* [2006]) than the other three or that some of the observational products do not contain enough information to constrain this parameter very well.

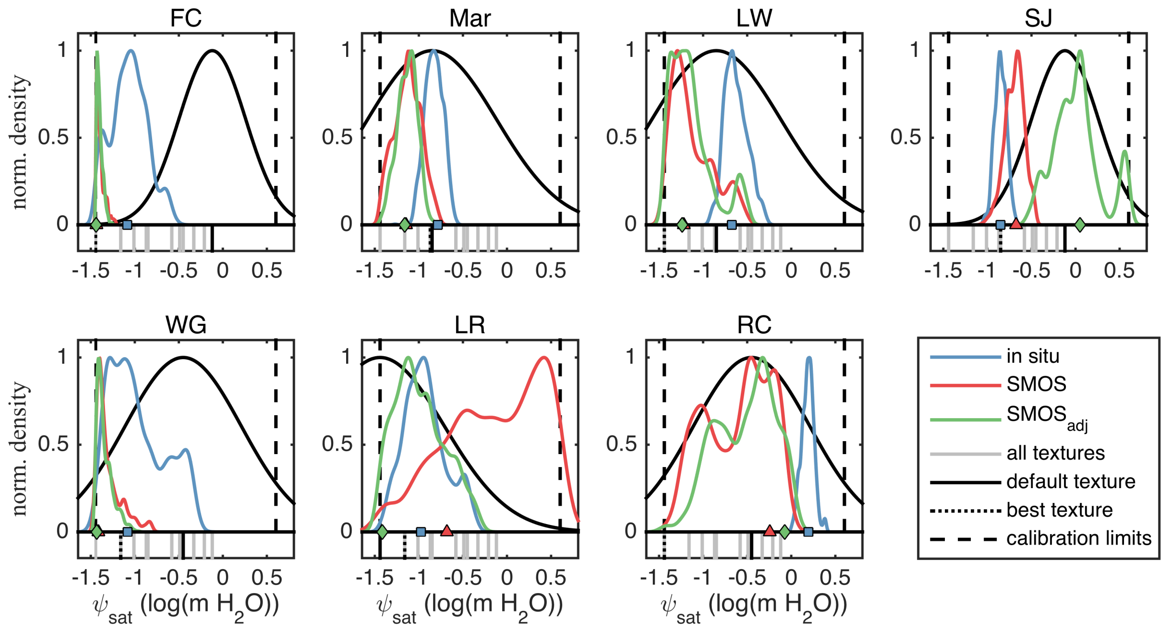

Figure 14: As in Figure 12, but for distributions of the ψ_{sat} parameter.

Figure 15 shows the posterior K_{sat} distributions. Like ψ_{sat}, K_{sat} also contains a few poorly-constrained posterior distributions, most notably at LR and RC using SMOS and $SMOS_{adj}$. We suspect these distributions to have resulted from lower-quality SMOS observations because the *in situ* calibrations are relatively well-behaved.

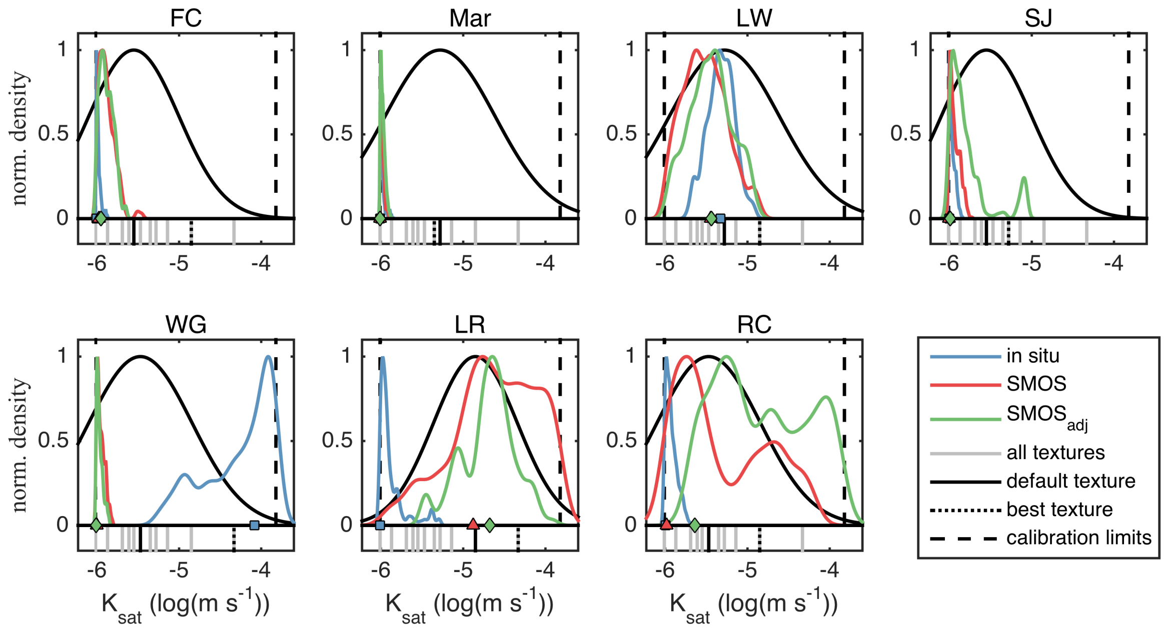

Figure 15: As in Figure 12, but for distributions of the K_{sat} parameter.

Table 5. A complete listing of the calibrated and default parameter values at each site. We also include two parameters that the Noah code derives from the four in this study: soil moisture at field capacity and soil moisture at wilting point.

		SHPs in this study				SHPs derived in Noah code	
Site	Parameter set	b (-)	θ_{sat} (cm^3cm^{-3})	ψ_{sat} (log (m H_2O)	K_{sat} (log (m s^{-1}))	soil moisture at field capacity (cm^3cm^{-3})	soil moisture at wilting point (cm^3cm^{-3})
FC	Default texture	5.33	0.476	-0.120	-5.552	0.360	0.084
	Best texture	4.26	0.421	-1.440	-4.852	0.283	0.028
	Calibrated to in situ	6.50	0.312	-1.085	-6.008	0.255	0.047
	Calibrated to SMOS	5.75	0.301	-1.436	-5.976	0.240	0.034
	Calibrated to $SMOS_{adj}$	6.81	0.307	-1.440	-5.953	0.251	0.043
Mar	Default texture	4.74	0.434	-0.850	-5.282	0.312	0.047
	Best texture	6.77	0.404	-0.870	-5.352	0.315	0.069
	Calibrated to in situ	5.10	0.429	-0.785	-6.010	0.337	0.053
	Calibrated to SMOS	3.96	0.334	-1.147	-6.010	0.250	0.022
	Calibrated to $SMOS_{adj}$	6.58	0.402	-1.159	-6.011	0.329	0.060
LW	Default texture	4.74	0.434	-0.850	-5.282	0.312	0.047
	Best texture	4.26	0.421	-1.440	-4.852	0.283	0.028
	Calibrated to in situ	3.94	0.386	-0.675	-5.330	0.267	0.034
	Calibrated to SMOS	4.68	0.333	-1.221	-5.447	0.243	0.029
	Calibrated to $SMOS_{adj}$	5.60	0.333	-1.239	-5.438	0.252	0.039

SJ	Default texture	5.33	0.476	-0.120	-5.552	0.360	0.084
	Best texture	4.74	0.434	-0.850	-5.282	0.312	0.047
	Calibrated to in situ	5.13	0.393	-0.851	-6.004	0.309	0.048
	Calibrated to SMOS	3.39	0.261	-0.673	-6.009	0.190	0.017
	Calibrated to $SMOS_{adj}$	20.85	0.313	0.050	-5.990	0.290	0.122
WG	Default texture	5.25	0.439	-0.450	-5.472	0.329	0.066
	Best texture	2.79	0.339	-1.160	-4.332	0.192	0.010
	Calibrated to in situ	3.94	0.277	-1.083	-4.081	0.169	0.019
	Calibrated to SMOS	2.55	0.340	-1.415	-6.002	0.234	0.006
	Calibrated to $SMOS_{adj}$	2.15	0.314	-1.431	-6.011	0.208	0.003
LR	Default texture	4.26	0.421	-1.440	-4.852	0.283	0.028
	Best texture	2.79	0.339	-1.160	-4.332	0.192	0.010
	Calibrated to in situ	3.32	0.200	-0.976	-6.010	0.145	0.010
	Calibrated to SMOS	50.88	0.307	-0.682	-4.878	0.293	0.134
	Calibrated to $SMOS_{adj}$	0.34	0.652	-1.415	-4.676	0.264	0.000
RC	Default texture	5.25	0.439	-0.450	-5.472	0.329	0.066
	Best texture	4.26	0.421	-1.440	-4.852	0.283	0.028
	Calibrated to in situ	3.25	0.349	0.196	-5.997	0.251	0.039
	Calibrated to SMOS	4.49	0.286	-0.242	-5.983	0.219	0.039
	Calibrated to $SMOS_{adj}$	8.25	0.331	-0.075	-5.640	0.272	0.085

The remainder of this section focuses on summarizing the differences between MAP values and texture class mean values for each SHP.

Except for $SMOS_{adj}$ at LR, all experiments and all best textures result in θ_{sat} being lower than its default assignment. We show in Figure 16 that this parameter correlates well with the mean VSM of its calibration time series, which is lower than that of the default simulation in almost all cases (Figure 5a). We include a line connecting the *in situ* and SMOS data at each site to show that this relationship is always positive within a location. The $SMOS_{adj}$ θ_{sat} values fall between those of the *in situ* and SMOS calibrations; $SMOS_{adj}$ is a hybrid of the two observational time series. The $SMOS_{adj}$ calibration at LR is clearly visible here as an outlier.

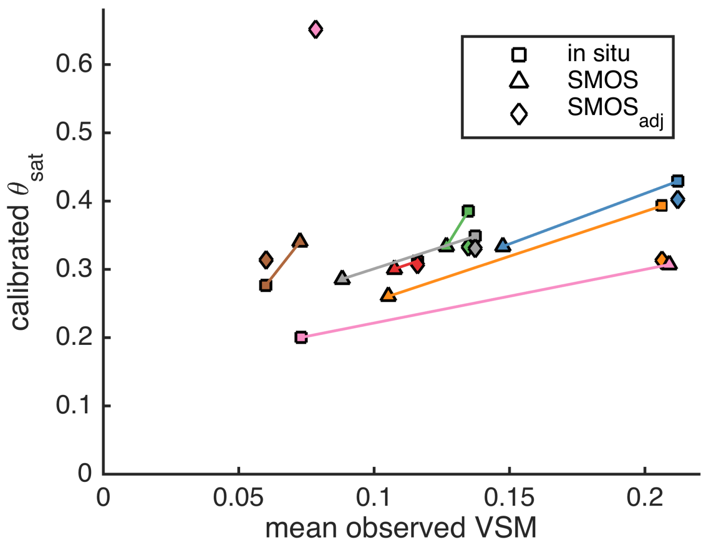

Figure 16: The calibrated θ_{sat} and the mean VSM for *in situ* (squares), SMOS (triangles), and SMOS$_{adj}$ (diamonds) observations.
Colors indicate site: FC red, Mar blue, LW green, SJ orange, WG brown, LR pink, and RC gray.

All calibrated K_{sat} parameters are lower than the default values with only two exceptions: SMOS$_{adj}$ calibration at LR and *in situ* at WG. In contrast, the best texture values are all higher than the default values, except at Mar. This division is the most distinct of the four parameters, and we address its implications in the discussion.

Neither b nor ψ_{sat} change much with calibration. The value of b remains similar to the default value, and ψ_{sat} values are similar or slightly lower. For both, however, the best texture values are consistently lower than the default. The only exception for b is Mar, where it is slightly higher and for ψ_{sat} is LR, where it already had the lowest possible value.

2.3.4 Nonbehavioral simulations at LR

LR has a number of problems with its calibrated simulations and parameters. Figure 17 shows the observational time series, default simulation, and rainfall at LR. The rainfall and vegetative cover are higher than at any other site (Table 2).

The *in situ* observations are lower than all but the arid WG site. The default simulation, likely because of this inconsistency, is poor, having a higher RMSD than any other location (Figure 3).

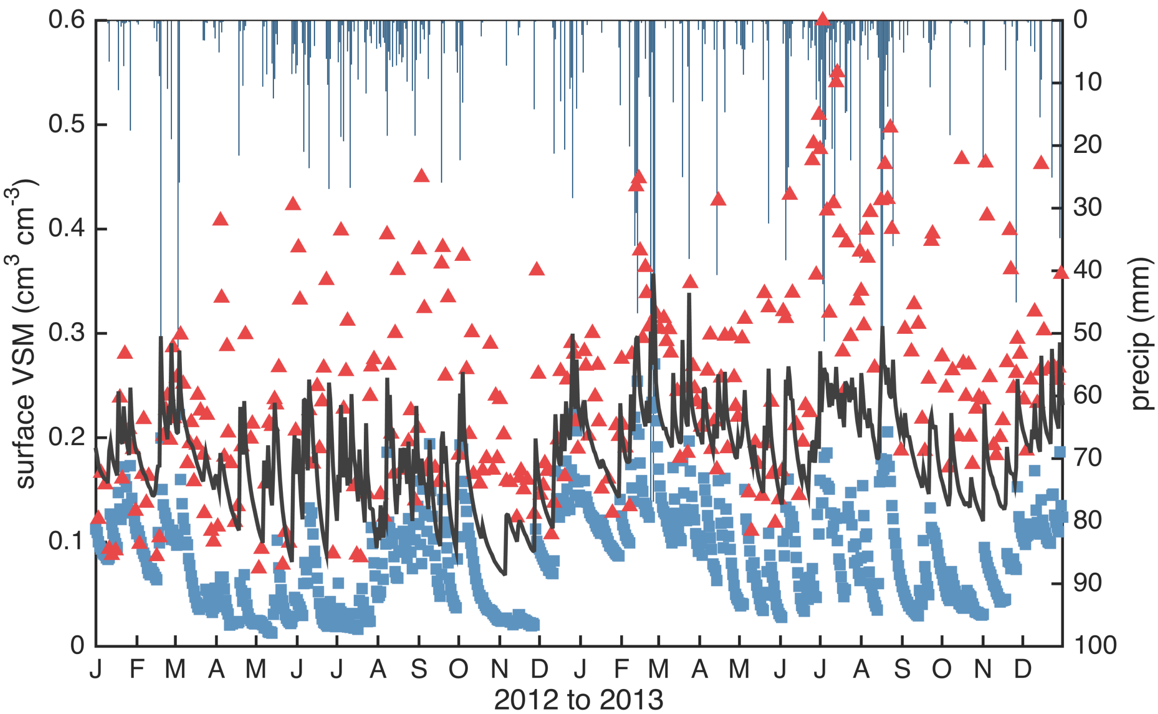

Figure 17: LR surface soil moisture content of the default simulation (black line), *in situ* observations (blue squares), and SMOS observations (red triangles). Daily precipitation is also included.

In all three LR calibration experiments, parameter values move away from the default, and simulations are nonbehavioral. When LR is calibrated to *in situ*, there is more than twice as much surface runoff as in any other simulation, and summer LHF decreases by 20 W m^{-2}. When LR is calibrated to SMOS, the simulation's surface soil moisture RMSD becomes higher than that of any other. Also, the value of the *b* parameter reaches its upper limit, which may not be physically realistic. Finally, when LR is calibrated to SMOS$_{adj}$, the resulting simulation has 1.5 times the subsurface runoff than the next highest simulation, and summer LHF decreases by more than 20 W m^{-2}. In addition, the θ_{sat} value is clearly an outlier (Figure 16), and the b value reaches its minimum value.

The mismatch between simulated and observed VSM at LR is too great to be reconciled through parameter calibration. The resulting nonbehavioral simulations reveal the following possibilities: (1) VSM data is not representative of the basin; (2) other parameters or model physics do not adequately characterize this site; and (3) meteorological forcings are inaccurate.

2.4 Discussion

Using the mapped soil texture and the standard SHP lookup table does not yield optimal Noah parameters. Simulations can be improved by changing the site's soil texture designation or by calibrating soil parameters using surface soil moisture from either *in situ* or $SMOS_{adj}$ observations. In either case, RMSD decreases mainly because of improved agreement between the simulated and observed mean surface VSM. Calibrating to SMOS alone does not reliably improve simulations. There are tradeoffs to using calibrated and best texture parameters. It is more likely that total column soil moisture, runoff, and LHF are affected through calibration, possibly yielding nonbehavioral simulations. On the other hand, no texture-based parameter set improves soil moisture dynamics as much as calibrated simulations do. We find this to be especially true at times and locations when the default simulation is worst.

Because of the poor performance of simulations calibrated to SMOS, we limit the remainder of our discussion to parameters and simulations from (1) the best *in situ* and $SMOS_{adj}$ calibrations, and (2) the best texture.

In situ and $\mathrm{SMOS_{adj}}$ calibrated parameters all have lower θ_{sat} and K_{sat} values than the default simulation does. The effect of decreasing θ_{sat} is to lower the threshold for surface runoff, lower the field capacity and residual VSM, and increase the relative conductivity of soil in the column. All three changes decrease the mean modeled surface VSM. The role of lower K_{sat} values is to decrease the speed at which water can be transferred into and through the soil column. Subsurface runoff decreases, and again, the likelihood of surface runoff increases. These processes explain our experimental results: lower VSM in calibrated simulations. Because water availability is lower, plant transpiration and overall LHF also decrease for all calibrations except $\mathrm{SMOS_{adj}}$ at WG, where there is limited vegetation. Subsurface runoff is unchanged or lower in all cases except $\mathrm{SMOS_{adj}}$ at LR.

An unfortunate side effect of calibration is the possibility of nonbehavioral simulations. All three calibrated simulations at LR are unreasonable in some way. They provide extreme runoff volumes and parameter values at the edges of their ranges. In addition, the changes to LHF seen at SJ and FC cannot be verified, and thus must be considered as potentially problematic. We attribute the LR failures in part to it being wet and well-vegetated. Large amounts of precipitation limit the number of soil drydown events, making SHPs less important relative to meteorological forcings. SMOS retrievals are subject to a wet bias on days with precipitation due to a shortening of the sensing depth [*Jackson et al.*, 2012]. Vegetation also increases the chances of inaccurate SMOS retrievals. Poor SMOS performance at LR is not new. In 2010, it had the highest RMSD among LR, WG, LW, and RC [*Jackson et al.*, 2012].

The best texture parameters result in simulations with lower mean surface VSM than default simulations. But they do not change physical processes of the model as much as calibrated parameters do. Surface runoff remains the same. Every site's best texture has lower b and ψ_{sat} values than its default texture, which decreases the water tension at a given moisture level. Together with higher K_{sat} values, these three parameters allow faster drainage through the soil column, but the overall volume of subsurface flow does not necessarily change. Because water is still transmitted through the lower layers, LHF is maintained at similar levels to the default simulation.

We have shown important differences in the ability of calibrated and texture-based simulations to capture wetting and drying events. When the default simulation is behaving poorly, all textures suffer from similar problems. Mar, SJ, and RC are the three locations that exhibit high ubRMSDs during some portion of the year. Visual inspection of the problematic time periods reveals that they occur during successive wetting and drying events. Calibrated simulations show decent agreement with observations. Low K_{sat} values allow surface soil moisture to increase dramatically during rain events because they limit infiltration to lower layers. Excess rainfall is shed as surface runoff, so subsequent drying is rapid. Texture-based parameters poorly characterize events that dry quickly. They allow for more infiltration, and subsurface runoff and transpiration are by nature slower than surface runoff.

Our study indirectly assesses the effect of scaling on SHPs. Texture-based parameters were developed in small-scale laboratory settings [*Cosby et al.*, 1984]. The modeling in this study applies to watersheds on the order of 100s of km^2. By identifying the best texture for each site, we are implicitly identifying the best texture for use at that larger scale. Thus, we reiterate the differences between mapped textures and best textures: b, θ_{sat}, and ψ_{sat} decrease, and K_{sat} increases. The change to b causes soils to drain more easily and decreases the residual VSM. The change to θ_{sat} causes more runoff, higher relative hydraulic conductivity, and lower overall moisture levels. The changes to ψ_{sat} and K_{sat} cause faster infiltration. These processes are consistent with the existence of macropores at larger scales and with the positive relationship between hydraulic conductivity and scale in heterogeneous media [*Schulze-Makuch et al.*, 1999]. Although the spatial coverage at Mar is small, its calibrated parameter values were well-behaved and not significantly different from those at the other sites.

There are different challenges associated with implementing a calibration strategy or choosing the best texture class at a continental scale. A successful calibration requires high-quality *in situ* measurements or an unbiased remotely-sensed product. At present, neither of these exists outside of specific, well-studied regions. NASA's SMAP mission [*Entekhabi et al.*, 2010] may provide data that meet such requirements, but the changes to runoff and LHF discussed here call for a more extensive investigation to assess viability. Alternatively, we can focus on developing a revised soil texture map. Presently, soil maps are associated with actual observations. At our study sites, however, the best texture is different from the mapped texture. We suggest using remotely-sensed data to select the best textures at a number of verifiable locations. Then, regionalization techniques could be used to apply the best textures continent-wide [*Singh et al.*, 2012]. This will require remotely-sensed data of higher quality (smaller or no bias) than we presently have, which we look to SMAP or SMOS reprocessing to provide.

2.5 Conclusions

We summarize our main findings:

(1) The mapped soil texture designations used in NLDAS-2 simulations do not provide optimal SHPs for Noah at all sites (FC, Mar, LW, SJ, WG, LR, and RC). Simulations with parameters from a different texture class would match surface soil moisture observations more closely. At SJ and WG, the best textures also improve ubRMSD.

(2) Calibration of SHPs is successful when we use *in situ* or unbiased SMOS observations: the resulting RMSDs between simulated surface soil moisture and *in situ* observations are lower than those from the default simulations. SMOS observations are not useful for calibration at Mar, SJ, and LR due to bias in the product.

(3) Calibration improves the simulation of surface soil moisture dynamics during time periods when default modeled wetting and drying is worst.

(4) Little or no change is made to surface soil moisture RMSD or ubRMSD when the default simulations are already good.

(5) The best textures and calibrations all produce simulations that have lower mean soil moisture than the default simulations, both at the surface and at depth. The best texture simulations allow for faster drainage through the column, whereas the calibrated simulations produce more surface runoff.

The calibration framework used in this study allows for reconciliation of model simulations with observations when it is executed using high-quality soil moisture data. However, when biases are present, this method results in compensating effects within the model that may be unrealistic. In addition, we have shown that ubRMSD is more challenging to improve than bias or RMSD. What this means is that the model cannot easily be made to match the dynamics of observed soil moisture. Now that we've established that differences in drying behavior are present, we take a step backwards to investigate and compare two observation sources against one another: remotely-sensed and *in situ* VSM.

Chapter 3: SMAP soil moisture drying more rapid than observed *in situ* following rainfall events

3.1 Background

The climate system retains memory of precipitation events through root zone soil moisture anomalies, which can persist on timescales up to months [*Koster et al.*, 2006; *Ghannam et al.*, 2016]. Although surface soil moisture varies more rapidly than deeper soil moisture due to the direct effects of precipitation and evaporation [e.g., *Kurc and Small*, 2004], propagation of anomalies from the surface layer influences dynamics throughout the soil profile and below [*Eltahir and Yeh*, 1999]. Observations of soil drying at the surface can therefore inform on deeper, more persistent anomalies that define the onset of drought [*Serafini and Sud*, 1987; *Ford et al.*, 2015], affect ecosystem dynamics [*D'Odorico et al.*, 2000; *Rodriguez-Iturbe*, 2000; *Daly and Porporato*, 2005], and control soil carbon and nitrogen cycles [*Porporato et al.*, 2003; *Ivanov et al.*, 2008]. Here, we focus on two ways to observe surface soil moisture dynamics: *in situ* measurements, and remotely-sensed products. The nature of these data is different enough to warrant investigation into how they characterize soil drying. The reason these observations are important is that studying them can lead to a better understanding of how observations can work together with models.

Remote-sensing missions such as SMAP and SMOS have coarse spatial resolution and only pass over a particular location periodically [*Njoku et al.*, 2003; *Kerr et al.*, 2010b; *Entekhabi et al.*, 2014]. However, the global coverage of space-borne sensors makes their data optimal for assimilation, allowing for possible improvements in simulations of root zone soil moisture and hydrometeorologic fluxes [e.g., *Martens et al.*, 2016]. To facilitate this process, efforts must be taken to characterize the differences between satellite retrievals and *in situ* observations.

The science requirement for SMAP (and SMOS) is to provide estimates of soil moisture in the top 5 cm of soil with an unbiased root mean squared error (ubRMSE) no greater than 0.04 cm^3 cm^{-3} [*Kerr et al.*, 2010b; *Entekhabi et al.*, 2014]. For SMAP validation, *in situ* soil moisture monitoring sites were developed and charged with providing an estimate of soil moisture over this same depth interval, at a spatial scale commensurate with the SMAP sensing footprint [*Entekhabi et al.*, 2014]. For practical reasons, *in situ* probes in these networks are typically placed at 5 cm depth, which means they measure soil moisture content between 3.5 and 6.5 cm [*Rondinelli et al.*, 2015]. In contrast, L-band radiometers such as that on SMAP measure soil moisture between the surface and a depth that varies. Though nominally 5 cm, penetration depth can be much shallower when soil water content is high [*Njoku and Kong*, 1977; *Escorihuela et al.*, 2010; *Jackson et al.*, 2012]. In addition, SMAP's soil moisture retrieval algorithm is strictly valid only for uniform soil moisture profiles [*Jackson et al.*, 2016], which may not exist immediately following rainfall.

Notwithstanding this imperfect representation of the passive L-band sensing depth, monitoring sites with probes inserted at 5 cm depth have been and continue to be a primary means of validating satellite-based soil moisture estimates [*Jackson et al.*, 2010, 2012; *Entekhabi et al.*, 2014]. *Chan et al.* [2016] used 13 such sites, referred to as core validation sites (CVS) [*Jackson et al.*, 2016], to demonstrate that initial SMAP soil moisture retrievals yield an ubRMSE of 0.038 cm^3 cm^{-3}, thus meeting the mission target. Despite this success, it was qualitatively noted that SMAP soil moisture dries more rapidly than observed *in situ* [*Chan et al.*, 2016], perhaps due to differences in sensing depth between the satellite and *in situ* observations [*Jackson et al.*, 2016].

Two previous studies demonstrated that SMOS soil moisture also decreases more quickly following rainfall than observed *in situ*. *Champagne et al.* [2016] analyzed data from four sites in Canada (including the two used here) and showed that although SMOS captured drying trends, SMOS soil moisture was often higher than the *in situ* observations soon after rainfall events. *Rondinelli et al.* [2015], using data from South Fork, Iowa, showed that surface drying rates from SMOS were faster than rates calculated from *in situ* observations. They used an unsaturated soil water flow model to demonstrate that differences in observation depths could explain the observed differences in drying rates.

This paper contributes to SMAP validation by comparing retrieved soil moisture with *in situ* observations during soil drying (drydown) events. Data from 193 distinct events across 17 sites with distributed networks of soil moisture probes were used for this analysis. SMAP and *in situ* soil moisture are both used to calculate (1) exponential timescales of soil drying [e.g., *Kurc and Small*, 2004; *Rondinelli et al.*, 2015], and (2) discrete drying rates as a function of time since last rainfall. Calculations are independent of bias and answer a more specific question than ubRMSE can: What differences exist between how SMAP and *in situ* probes characterize drying of the land surface after a rain event? Analyses include *in situ* data at both its native high frequency and at the SMAP observation frequency, allowing us to assess if critical information about drying is lost due to the timing and frequency of SMAP observations. Quantifying the accuracy of SMAP drying rates is necessary for informed use of SMAP soil moisture observations.

3.2 Materials and Methods

3.2.1 Data

3.2.1.1 SMAP Observations

The SMAP satellite was launched on January 31, 2015. SMAP overpasses are every 1 to 3 days, with the repeat interval depending on latitude. SMAP's radiometer operates in the L band of the microwave spectrum (1.41 GHz) [*Entekhabi et al.*, 2014]. The SMAP radiometer soil moisture team has developed five soil moisture retrieval algorithms to generate level 2 passive soil moisture estimates (L2SMP). This study used the baseline soil moisture algorithm: single channel algorithm using vertical polarization observations (SCAV) [*Chan et al.*, 2016]. All SMAP data shown here were processed using a 36 km grid centered on each CVS (described below) and thus differs from the publically-available data on the EASE-Grid. We used level 2 descending half-orbit (~6 am local time) observations from 31 March 2015, to 1 March 2016 (data version 3). Data flagged due to frozen conditions, snow, dense vegetation, and precipitation were excluded from the analysis.

3.2.1.2 *In situ* observations

The SMAP validation program collaborates with CVS situated around the world. These locations constitute an extensive network of densely-instrumented soil monitoring sites, allowing rigorous and continual evaluation of SMAP retrievals. Analyses use up-scaled data from 17 CVS (Table 6), not individual probe values. Up-scaling is based on a geometrically-weighted average of probes within the pixel [*Colliander et al.*, 2015] that qualifies them for use at the 36 km scale [*Jackson et al.*, 2016]. At all sites, probes were inserted horizontally at 5 cm depth, except Yanco and Kyeamba, Australia, where most probes were inserted vertically (0 to 5.8 cm).

Table 6: Each core validation site (CVS) used in this paper.
We provide the location, the abbreviation we use in figure legends, the principal investigator(s), the number of drydowns analyzed, the number of days in those drydowns, and the date ranges used. *Indicates that as of 1/23/16, the site was a candidate CVS.

Number of Drydowns	Number of days	Data availability (snow-free) Start	End
7	80.4	3/31/15	3/1/16
16	191.6	3/31/15	3/1/16
12	144	3/31/15	3/1/16
10	76.7	3/31/15	11/15/15
9	84.9	3/31/15	11/1/15
2	13.3	4/1/15	1/15/16
13	155.8	3/31/15	3/1/16
2	15.7	3/31/15	12/1/15
16	186.6	3/31/15	3/1/16
22	166	3/31/15	3/1/16
20	222	3/31/15	3/1/16
2	15.1	3/31/15	11/1/15
15	122.5	3/31/15	12/10/15
12	110.3	3/31/15	1/5/16
13	140.9	3/31/15	3/1/16
14	187.8	3/31/15	3/1/16
8	91.95	3/31/15	3/1/16

Site Name	State, Country	Abbreviation	PI	Latitude	Longitude
Monte Buey	Argentina	mobu	Thibeault	-32.96	-62.52
Kyeamba	Australia	kyea	Walker	-35.36	147.51
Yanco	Australia	yanc	Walker	-34.85	146.17
Carman	MB, Canada	carm	McNairn	49.58	-97.94
Kenaston	SK, Canada	kena	Berg	51.45	-106.46
Twente	Netherlands	twen	van der Velde	52.28	6.69
REMEDHUS	Spain	reme	Martínez-Fernández	41.28	-5.41
Valencia*	Spain	vale	Lopez-Baeza	39.52	-1.21
Fort Cobb	OK, USA	foco	Starks	35.42	-98.62
Little River	GA, USA	liri	Bosch	31.62	-83.59
Little Washita	OK, USA	liwa	Starks	34.88	-98.09
Reynolds Creek	ID, USA	recr	Seyfried	43.14	-116.76
South Fork	IA, USA	sofo	Cosh/Prueger	42.47	-93.39
St Josephs*	IN, USA	stjo	Livingston	41.40	-85.02
Tonzi Ranch*	CA, USA	tora	Moghaddam	38.47	-121.00
TxSON	TX, USA	txso	Caldwell	30.31	-98.78
Walnut Gulch	AZ, USA	wagu	Goodrich	31.68	-110.04

In situ data have a sampling frequency of 60 minutes or less. These data, referred to in our analyses below as $\text{inSitu}_{\text{all}}$, are assumed to represent the 'true' soil moisture drying dynamics at each CVS. Land surface heterogeneities are averaged out by the upscaling calculation at each site. Network accuracies where quantified are 0.02 cm^3 cm^{-3} or better [*Cosh et al.*, 2004, 2006, 2008; *Bosch et al.*, 2006]. Probe random errors average 0.01 cm^3 cm^{-3} [*Coopersmith et al.*, 2016], and probe precision is better than 0.01 cm^3 cm^{-3} [*Seyfried et al.*, 2005]. All analyses were also completed using a subset of *in situ* observations that correspond in time with SMAP retrievals.

This subset of data is referred to as inSitu$_{SMAP}$. Figure 18 shows the temporally-resampled *in situ* data and a graphic representation of the model parameters. Temporal resampling isolates the effects of SMAP observation frequency (inSitu$_{all}$ vs. inSitu$_{SMAP}$) from overall differences (inSitu$_{all}$ vs. SMAP).

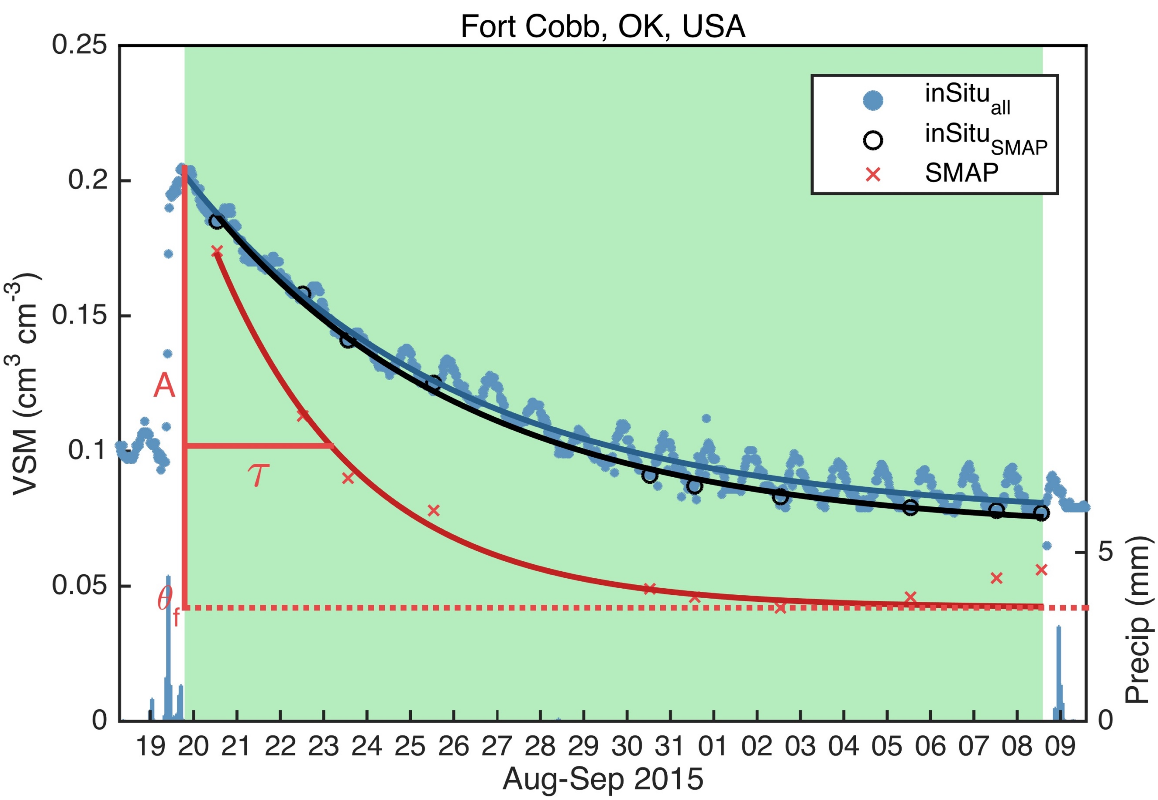

Figure 18: A single drydown (highlighted in green) at Fort Cobb, Oklahoma. Markers show inSitu$_{all}$, inSitu$_{SMAP}$, and SMAP observations. Exponential model fits are shown with curves. Parameter values A, τ, and θ_f characterize the curves as shown for the SMAP fit.

3.2.1.3 Precipitation Products

Precipitation networks are not available at every CVS. In order to ensure a homogenous analysis (gauges, where present, do not have uniformity in number or density), we used Land Data Assimilation System (LDAS) products at all sites. North American LDAS (NLDAS-2) precipitation [*Xia et al.*, 2012b] covers North American locations, and Global LDAS (GLDAS-1) covers all others [*Rodell and*

Beaudoing, 2007]. Analyses employed the 1/8th degree NLDAS-2 or the 1/4th degree GLDAS-1 cell that is most closely aligned with each CVS. The use of such large-scale precipitation products prohibits investigation into possible effects of non-uniform rainfall. In addition, because these products have errors and scale discrepancies, they provided only initial guidance in selecting rain-free intervals. The drydowns were further evaluated and adjusted as follows.

3.2.2 Selection of drydown events

We selected discrete drydown intervals using a two-step process. First, we used LDAS precipitation to automatically identify dry periods that follow rainfall events. The start of such a drydown is designated after 5 mm (or more) of rain has accumulated in the preceding 24 hours. The drydown ends once more than 2 mm of subsequent precipitation accumulates. We only consider drydowns that are at least 4 days long. Second, we manually adjusted the drydown start time to within an hour after the observed maximum *in situ* soil moisture and adjusted the end time to just prior to any increase in soil moisture due to new rainfall. In addition, we excluded events that: had obvious errors (sensors dropping in or out), contained fewer than two concurrent SMAP and *in situ* observations, or demonstrated no response of soil moisture to the rainfall or drydown. The selection process therefore avoided relying exclusively on LDAS products, so using different precipitation data would have minimal impacts on the results.

Using these criteria, 193 drydown events were identified, totaling 2005 days across the 17 CVS (Table 6, and Figure 19 – Figure 35). All analyses are limited to observations from these drydown periods, which include 959 SMAP observations and constitute 40% of the snow-free record.

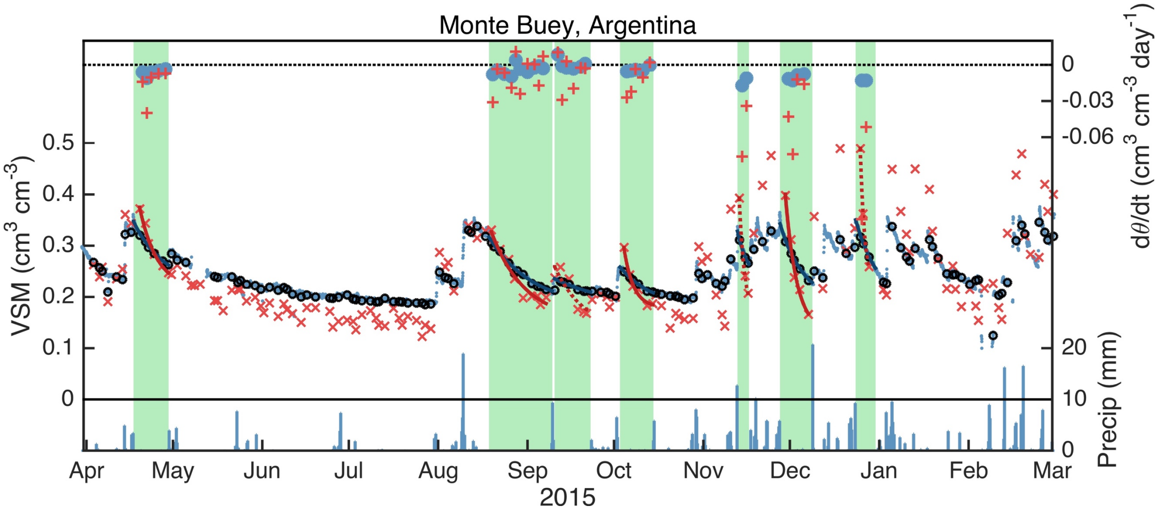

Figure 19: Rainfall (bottom), VSM (middle), and soil drying rates (top) at Monte Buey, Argentina.
Drydowns are highlighted in green. Markers show $inSitu_{all}$ (blue dot), $inSitu_{SMAP}$, (black circle), and SMAP (red ex) observations. Solid curves are models whose confidence interval around τ does not include zero (acceptable fits). Dotted curves are fitted exponential models whose confidence interval around τ includes zero (low-quality fits). $InSitu_{SMAP}$ fits are nearly identical to $inSitu_{all}$ fits and are not shown.

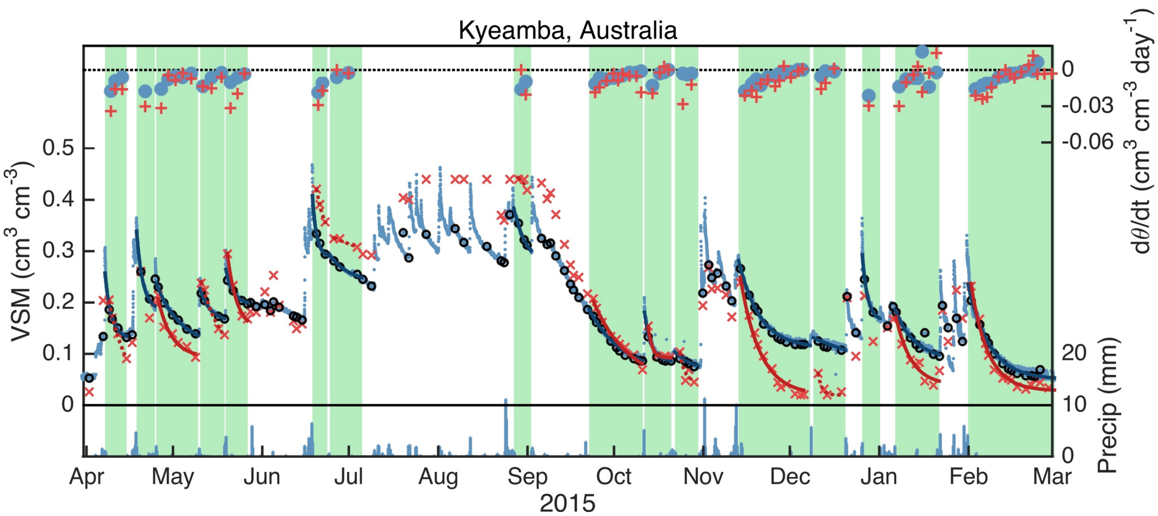

Figure 20: Kyeamba, Australia.
Markers and lines are as in Figure 19.

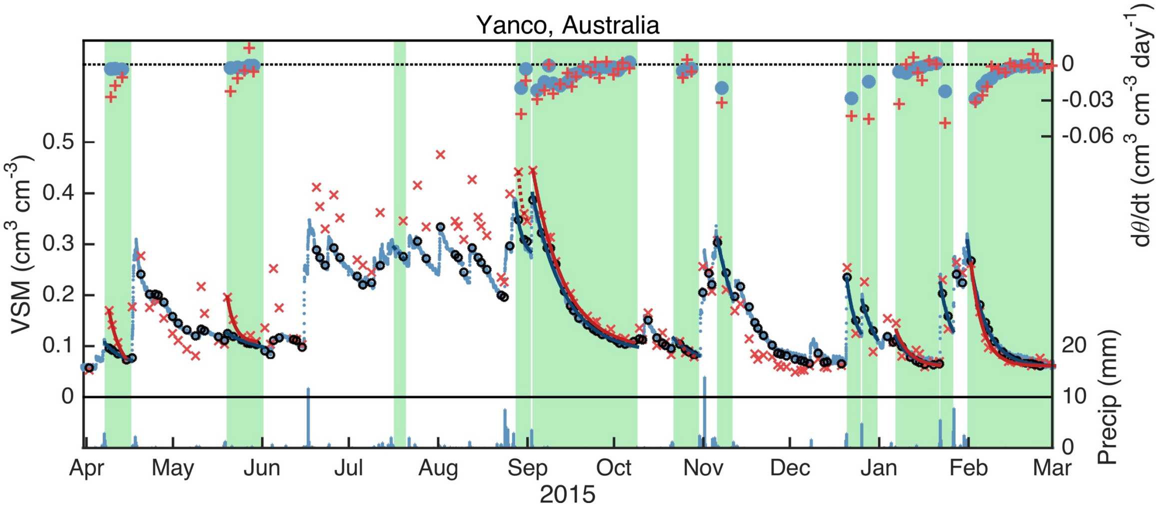

Figure 21: Yanco, Australia.
Markers and lines are as in Figure 19.

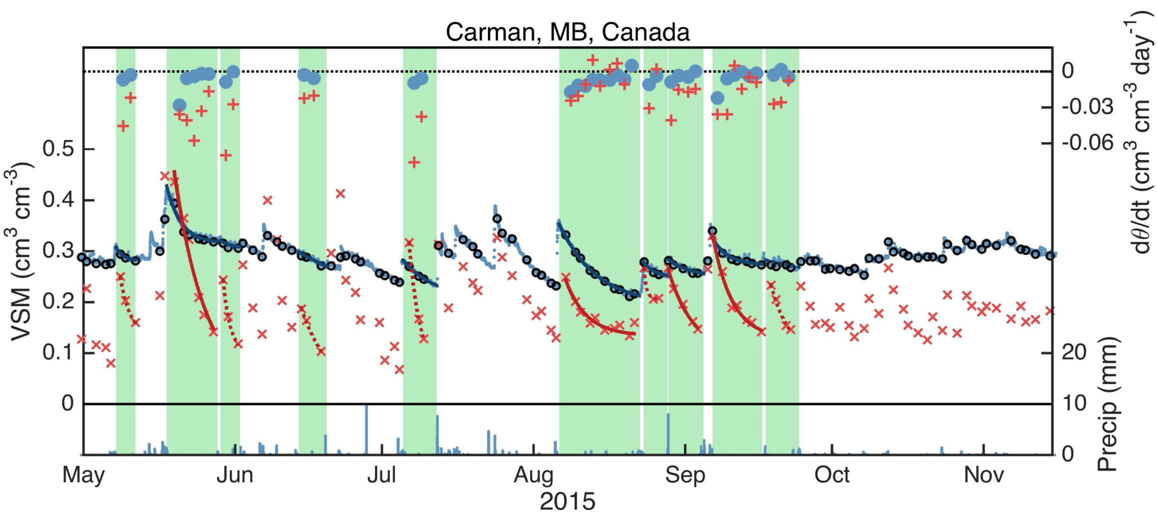

Figure 22: Carman, Manitoba, Canada.
Markers and lines are as in Figure 19.

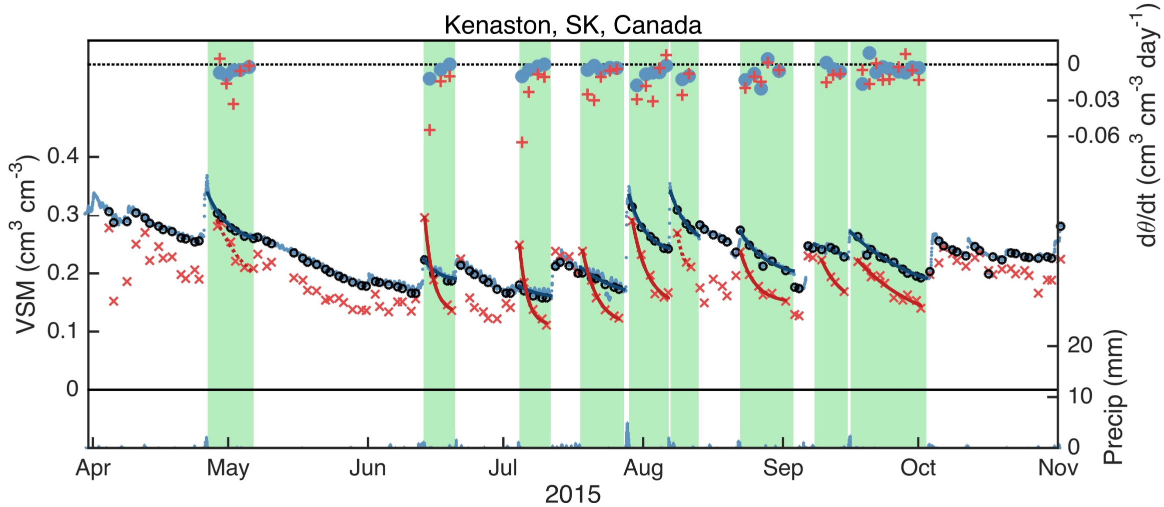

Figure 23: Kenaston, Saskatchewan, Canada.
Markers and lines are as in Figure 19.

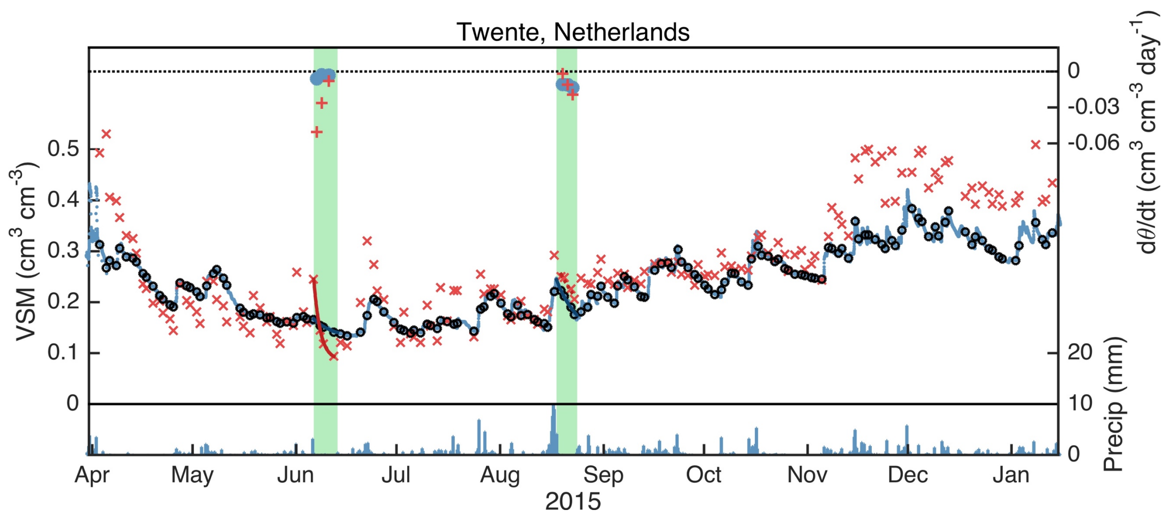

Figure 24: Twente, Netherlands.
Markers and lines are as in Figure 19.

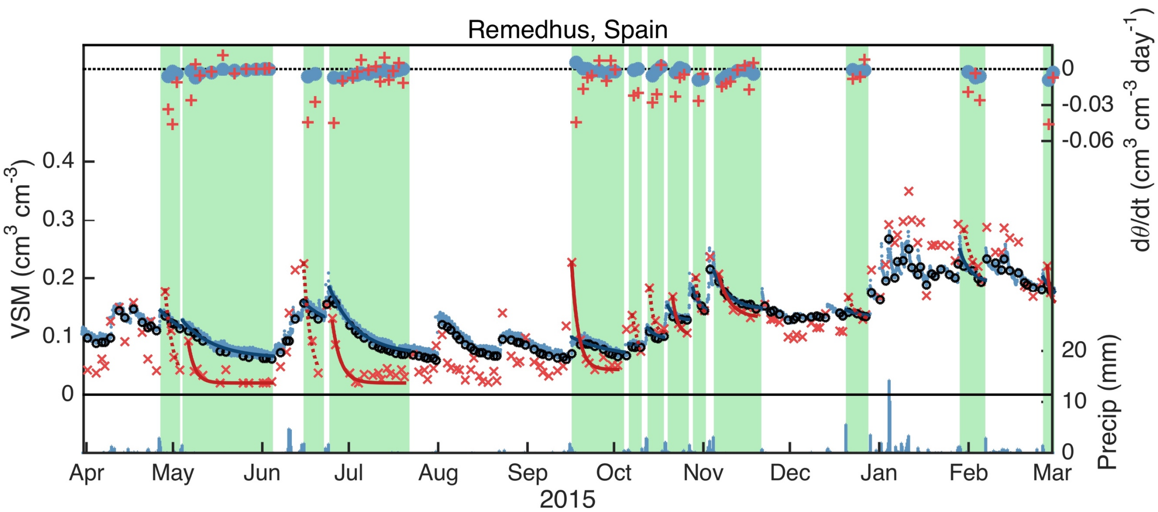

Figure 25: REMEDHUS, Spain.
Markers and lines are as in Figure 19.

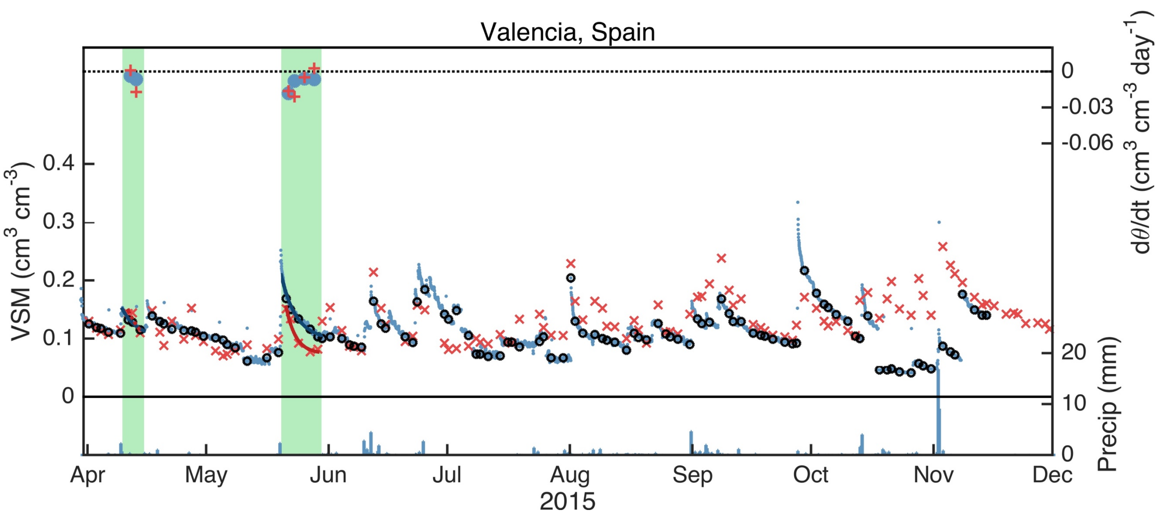

Figure 26: Valencia, Spain.
Markers and lines are as in Figure 19.

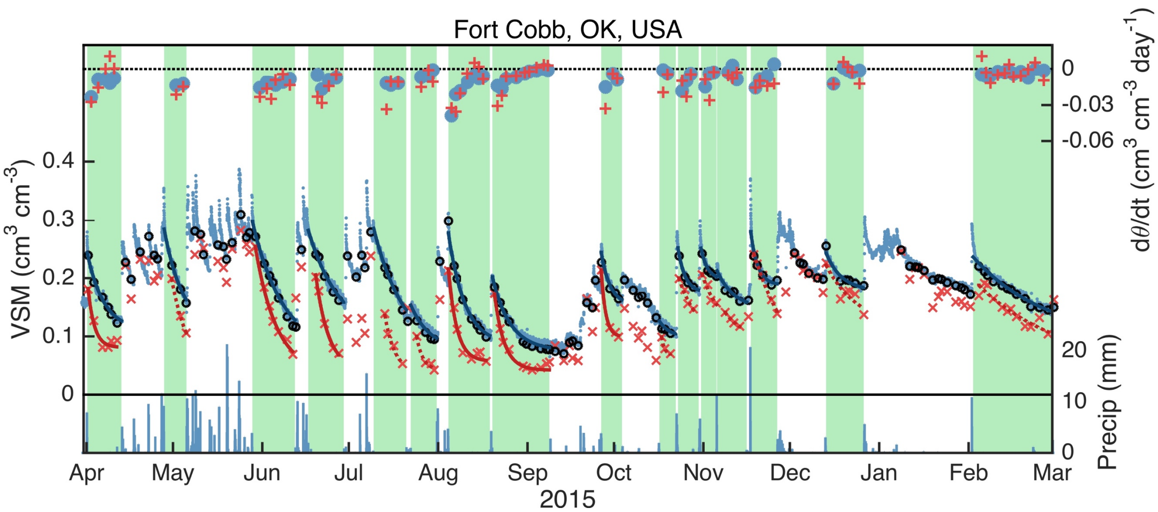

Figure 27: Fort Cobb, Oklahoma, USA.
Markers and lines are as in Figure 19.

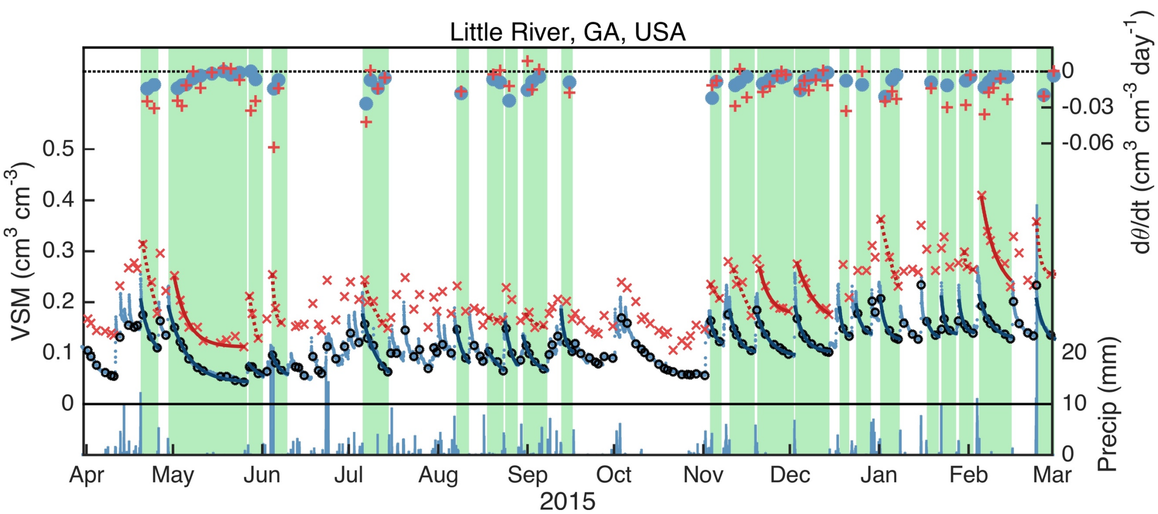

Figure 28: Little River, Georgia, USA.
Markers and lines are as in Figure 19.

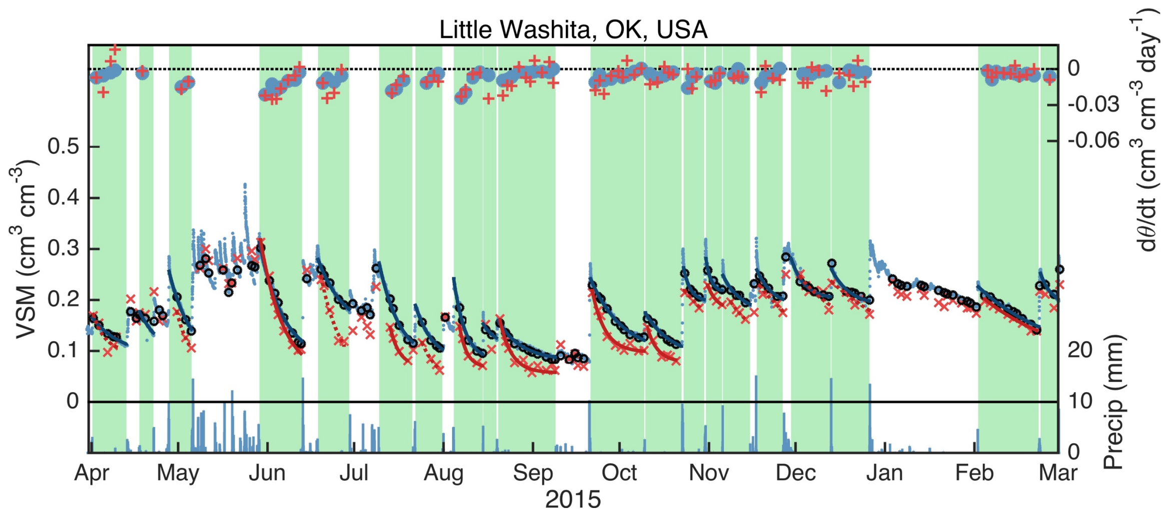

Figure 29: Little Washita, Oklahoma, USA.
Markers and lines are as in Figure 19.

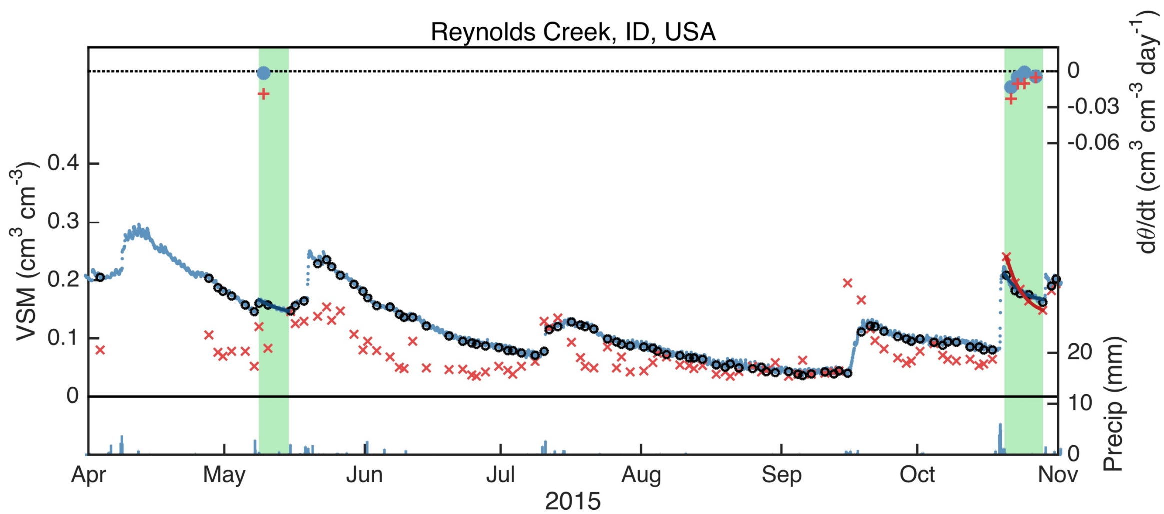

Figure 30: Reynolds Creek, Idaho, USA.
Markers and lines are as in Figure 19.

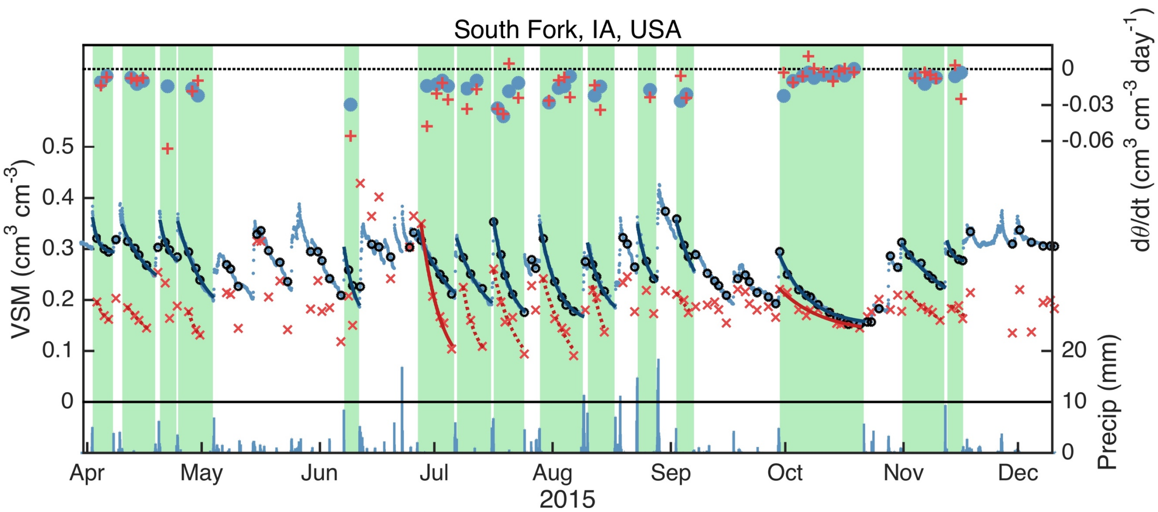

Figure 31: South Fork, Iowa, USA.
Markers and lines are as in Figure 19.

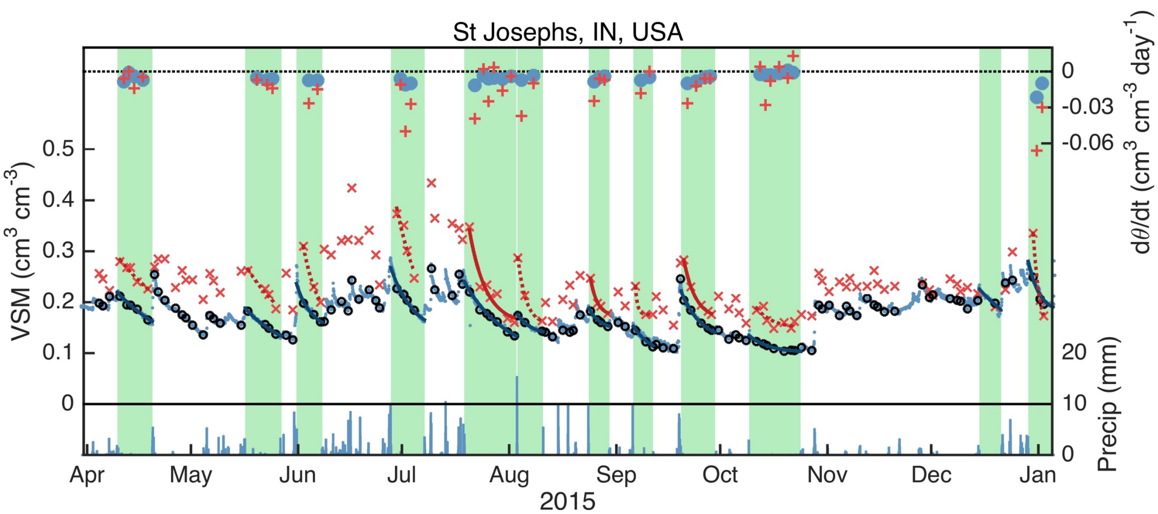

Figure 32: St Josephs, Indiana, USA.
Markers and lines are as in Figure 19.

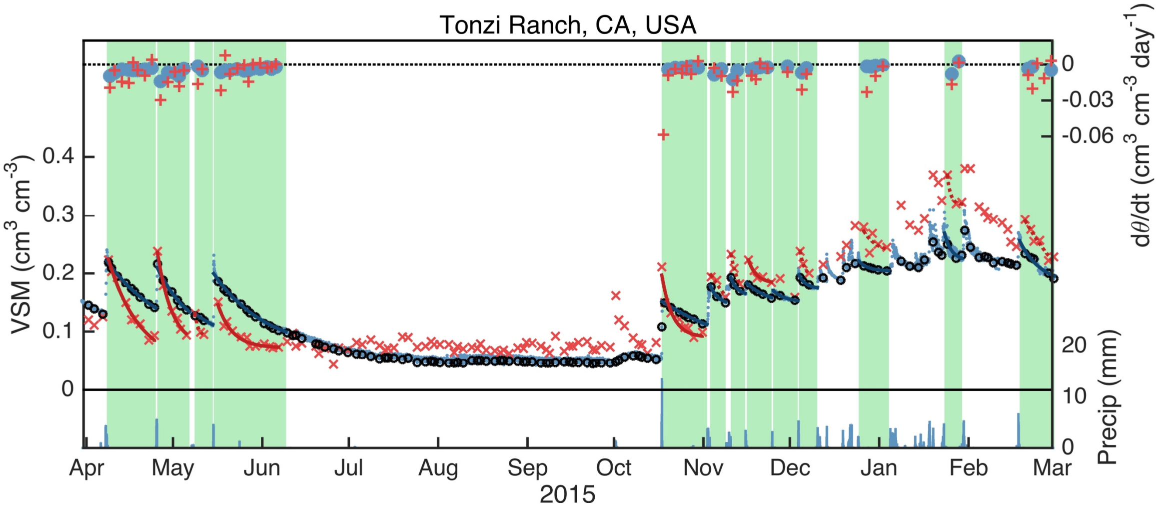

Figure 33: Tonzi Ranch, California, USA.
Markers and lines are as in Figure 19.

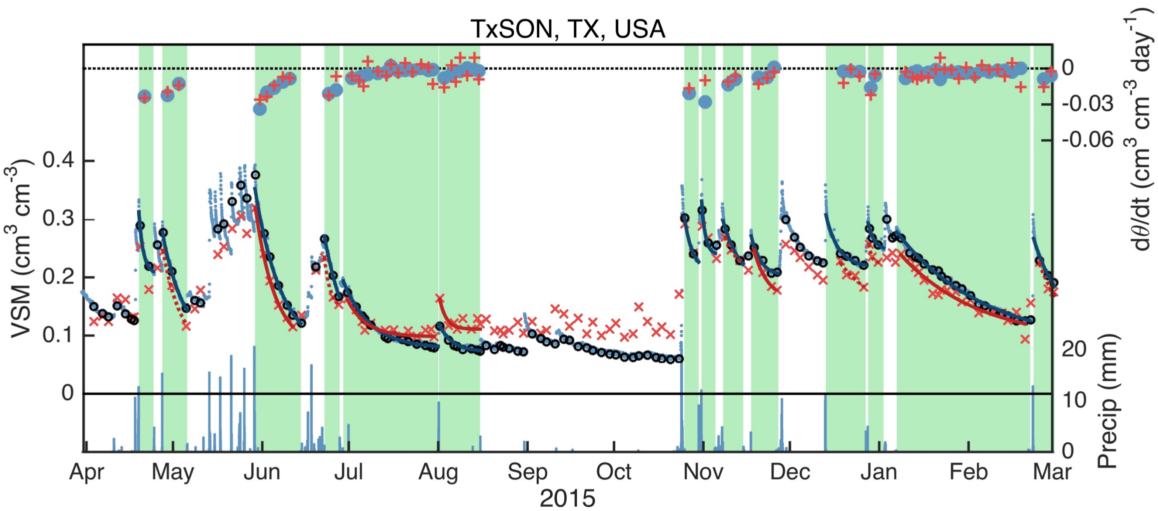

Figure 34: TxSON, Texas, USA.
Markers and lines are as in Figure 19.

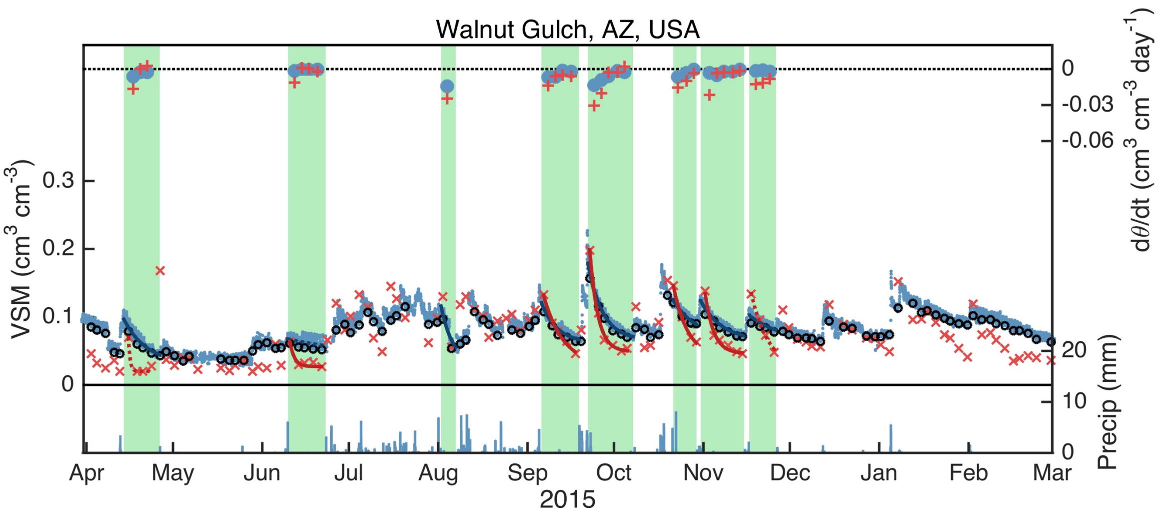

Figure 35: Walnut Gulch, Arizona, USA.
Markers and lines are as in Figure 19.

3.2.3 Analysis methods

Two methods were used to analyze and compare SMAP observations with *in situ* observations: (1) Fitting of an exponential model to assess the timescale and magnitude of drying; and (2) Calculation of discrete drying rates between successive observations. Both of these methods provide information in an unbiased framework, so adjusting SMAP time series for bias is unnecessary.

3.2.3.1 Exponential model

We modeled the *in situ* and SMAP observations from individual drydowns as exponential decay functions [*Kurc and Small*, 2004; *Rondinelli et al.*, 2015]:

$$\theta(t) = A * e^{\left(-\frac{t}{\tau}\right)} + \theta_f, \tag{5}$$

where θ is surface soil moisture content (cm^3 cm^{-3}), t is time since the beginning of the drydown (days), and A, τ, and θ_f are empirically-determined fitting parameters indicating, respectively, the magnitude of soil moisture drying (cm^3 cm^{-3}), the exponential time constant (days), and a final soil moisture content (cm^3 cm^{-3};

Figure 18). Modeled θ approaches but never reaches θ_f. We therefore constrain θ_f below the lowest soil moisture observed during the drydown and at or above the site's lowest (residual) soil moisture.

For each event, model parameters (τ, A, and θ_f) were selected to minimize the sum of squared errors between modeled soil moisture and: (1) $inSitu_{all}$, (2) $inSitu_{SMAP}$, and (3) SMAP observations. Parameter selection used a subspace trust-region algorithm, based on the interior-reflective Newton method [*Coleman and Li*, 1994, 1996].

When fitting Eq. (5) to the three observation types, confidence intervals at the 68% level were determined, corresponding to one standard deviation. An 'acceptable' fit is considered to be one in which the τ confidence interval does not include zero. Using this criterion, 188 of the 193 models fit to $inSitu_{all}$ drydowns were found to be acceptable. Such success indicates that the exponential model provides a reasonable characterization of soil moisture. In contrast, only 88 and 74 models fit to $inSitu_{SMAP}$ and SMAP (respectively) were acceptable. This does not indicate that the exponential model is inappropriate for these data, but that the lower SMAP observation frequency increases parameter uncertainty. After screening out low-quality fits, there were 63 drydowns that had acceptable model fits to all three observation types. Exponential model results are limited to this subset of drydowns. Widening or narrowing the confidence interval does not significantly alter the results of this study.

3.2.3.2 Soil drying rates

We calculated rates of soil drying ($d\theta/dt$) using finite differences within drydown periods:

$$\frac{d\theta}{dt} = \frac{\theta_{n+1} - \theta_n}{t_{n+1} - t_n}, \tag{6}$$

where n and $n+1$ correspond to consecutive observations. This analysis required only 2 or more soil moisture observations within each drydown interval. Thus, unlike the exponential analysis, all 193 drydowns were included. For comparison against SMAP, we use daily *in situ* data ($\text{inSitu}_{\text{daily}}$), starting 12 hours after the drydown commences. This removes the diurnal fluctuations present in $\text{inSitu}_{\text{all}}$. A total of 1807 $\text{inSitu}_{\text{daily}}$ soil drying rates were calculated, across all sites and drydowns. SMAP and $\text{inSitu}_{\text{SMAP}}$ both yielded 769 because of their lower observation frequency.

Drying rates are expected to be most negative at the beginning of a drydown and trend towards zero. To ensure that abnormally infrequent observations did not affect our results, we only calculated drying rates when $t_{n+1}-t_n$ (Eq. 6) was three or fewer days. Errors in individual observations introduced considerable noise into the calculated drying rates (Figures 1 and S2-S18). Therefore, each drying rate was binned according to how many days into the drydown interval its midpoint fell, rounded to the nearest whole number day. The results and discussion below are focused on the median value from each bin.

3.3 Results

For the 2005 drydown days across all sites, the average ubRMSE between SMAP and *in situ* soil moisture is 0.033 $cm^3\ cm^{-3}$, within SMAP mission target accuracy. This is similar to the 0.038 $cm^3\ cm^{-3}$ ubRMSE reported by *Chan et al.* [2016] using observations from the full period of record. The four sites with highest ubRMSEs in *Chan et al.* [2016] (carm, sofo, kyea, reme) all had ubRMSE > 0.04 $cm^3\ cm^{-3}$ in this study as well. By comparing timescales and drying rates between SMAP and *in situ* observations, we can uncover important differences not captured by ubRMSE. All results are summarized using median values to avoid the effects of a positive skew in τ (its range is zero to infinite). Using mean values does not change the findings.

3.3.1 Exponential timescales of soil drying

The exponential model fits both SMAP and *in situ* observations of soil moisture following rainfall events (Figure 36): drying is rapid at first and slows with time. The median RMSEs between model fits and observations are well below 0.01 $cm^3\ cm^{-3}$ for all observation types (Table 1). Exponential drying timescales (τ) vary from several to more than 20 days across the 63 events. Investigation into why τ varies from event to event or site to site is beyond the scope of this paper. Possibilities include differences in meteorological conditions, water table depth, vegetation, and soil texture.

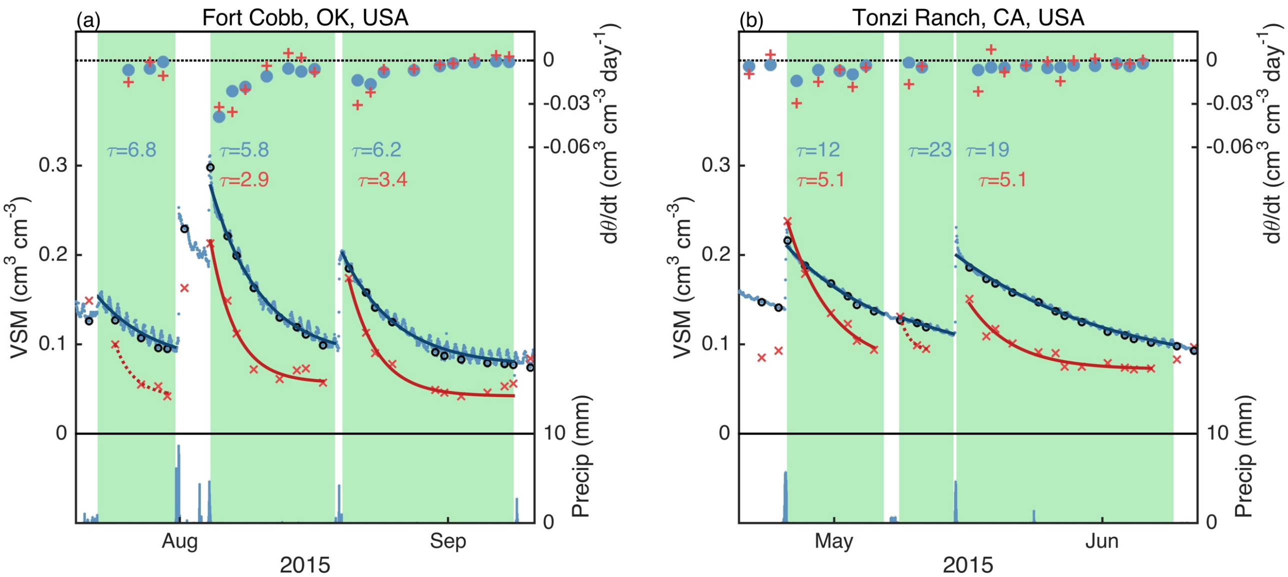

Figure 36: Rainfall (bottom), volumetric soil moisture (VSM; middle), and soil drying rates (top) at Fort Cobb, Oklahoma (**a**) and Tonzi Ranch, California (**b**). Drydowns are highlighted in green. Markers show $\mathrm{inSitu_{all}}$ (blue dot), $\mathrm{inSitu_{SMAP}}$ (black circle), and SMAP (red ex) observations. Solid curves are models whose confidence interval around τ does not include zero (acceptable fits). Dotted curves are fitted exponential models whose confidence interval around τ includes zero (low-quality fits). $\mathrm{InSitu_{SMAP}}$ fits are nearly identical to $\mathrm{inSitu_{all}}$ fits (Figure 18) and are not shown. τ values for acceptable model fits are displayed according to color.

Table 7: Model Fits, Parameters, and Uncertainties.
Median RMSEs, parameters, and uncertainties for exponential fits to each data type. These data come from 63 drydowns that provide acceptable model fits to all three observation types. *A* and θ_f values and uncertainties are expressed as 100* cm^3 cm^{-3}.

	Observations used to fit model		
	$\mathrm{InSitu_{all}}$	$\mathrm{InSitu_{SMAP}}$	SMAP
RMSE (cm^3 cm^{-3})	0.0042	0.0020	0.0062
τ (days)	7.33	7.30	4.08
τ uncertainty (days)	0.19	1.30	1.29
A (100* cm^3 cm^{-3})	11.3	11.1	15.2
A uncertainty (100* cm^3 cm^{-3})	0.09	2.1	3.4
θ_f (100* cm^3 cm^{-3})	9.0	9.1	9.2
θ_f uncertainty (100* cm^3 cm^{-3})	0.11	0.84	1.0

τ values fit to SMAP data are consistently smaller than those fit to $\mathrm{inSitu_{all}}$. For example, the third drydown in Figure 36a has SMAP and $\mathrm{inSitu_{all}}$ τ values of 3.4 and 6.2 days, respectively. This difference is consistent across nearly all drydowns: of the 63 events with acceptable fits, 53 fall below the 1:1 line in Figure 37a. The median τ value is 44% smaller when fit to SMAP (4.08 days) than when fit to $inSitu_{all}$ (7.33 days) (Table 7). Restricting the frequency and timing of *in situ* observations to that of SMAP does not decrease the exponential drying timescale. Corresponding τ values fit to $inSitu_{all}$ and $inSitu_{SMAP}$ are centered on the 1:1 line in Figure 37b, and their median values are nearly identical (Table 7).

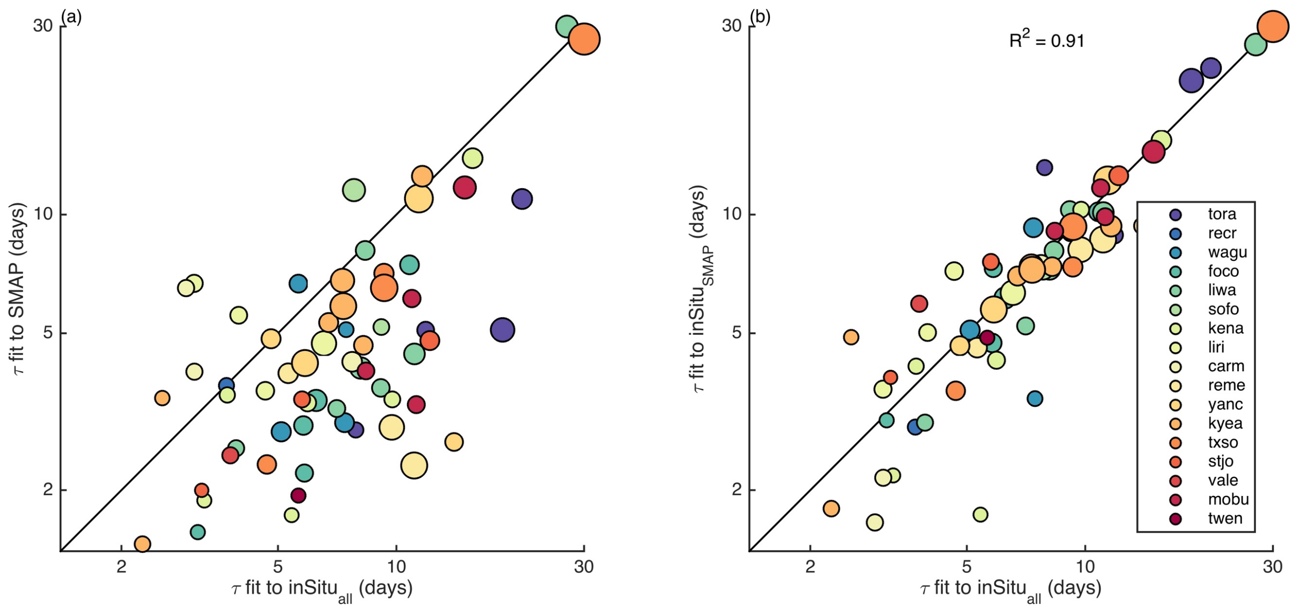

Figure 37: (**a**) Relationship between $inSitu_{all}$-fit and SMAP-fit τ values. (**b**) Relationship between $inSitu_{all}$-fit and $inSitu_{SMAP}$-fit τ values.
Marker colors correspond to each site as shown. Marker sizes correspond to length of drydown.

Based on *A* (Eq. 5), SMAP almost always observes a larger magnitude of soil moisture drying than *in situ* probes do. Of the 63 modeled drydowns, 53 have larger *A* values when fit to SMAP than when fit to $inSitu_{all}$. They lie above the 1:1 line in Figure 38a. Median values are 35% higher for SMAP than for *in situ* (Table 7). As with τ values, restricting the frequency and timing of *in situ* observations to that of SMAP does not change the modeled magnitude of drying. Figure 38b shows that *A* values associated with $inSitu_{all}$ and $inSitu_{SMAP}$ are nearly identical (fall along the 1:1 line).

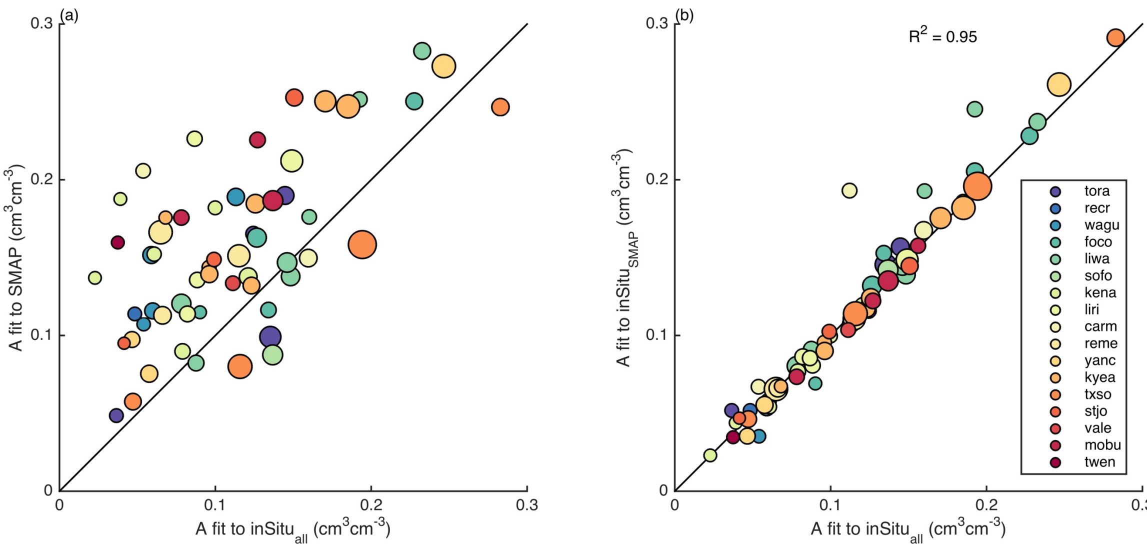

Figure 38: (**a**) Relationship between $inSitu_{all}$-fit and SMAP-fit A values. (**b**) Relationship between $inSitu_{all}$-fit and $inSitu_{SMAP}$-fit A values.
Marker colors correspond to each site as shown. Marker sizes correspond to length of drydown.

By plotting the final soil moisture values (θ_f in Eq. 5), we show that they are not identical between models fit to SMAP and $inSitu_{all}$ and that they exhibit no consistent difference (Figure 39a). As before, θ_f values when the model is fit to $inSitu_{all}$ and $inSitu_{SMAP}$ are nearly identical (Figure 39b).

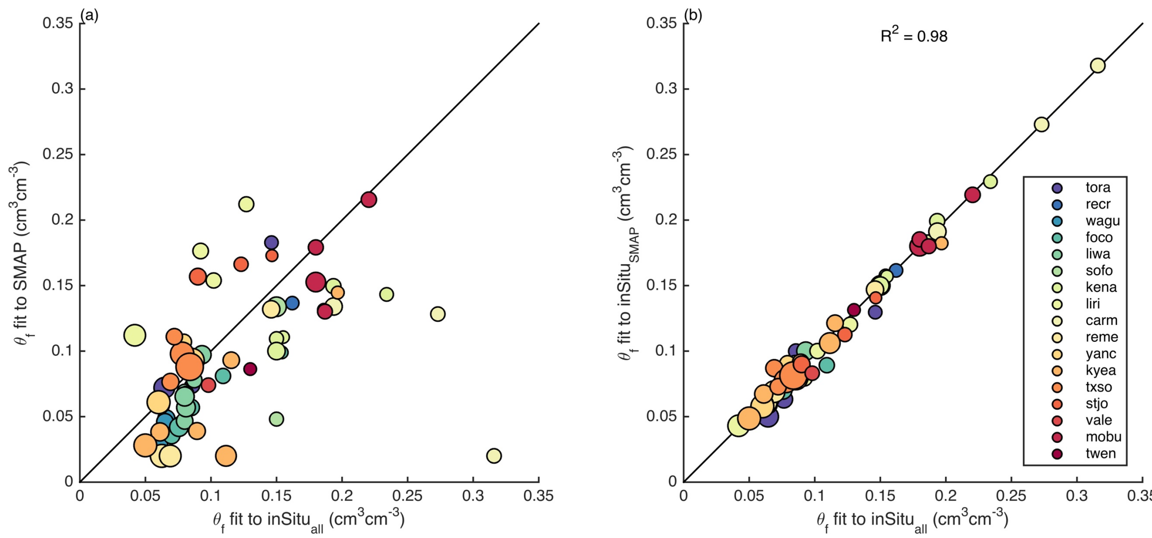

Figure 39: As in Figure 38, but showing θ_f parameter values.

Parameter uncertainties (Table 7) are primarily related to the number of observations, not how well the exponential model describes the data. Fits to $\text{inSitu}_{\text{all}}$ have the lowest uncertainty. Models fit to $\text{inSitu}_{\text{SMAP}}$ and SMAP have the same limited number of observations and similarly high parameter uncertainties due to the challenge of fitting a multiple-parameter model with a limited number of observations.

3.3.2 Discrete drying rates

Figure 40 shows how drying rates vary with increasing time since cessation of rainfall. Data for each site are shown individually in Figure 19 – Figure 35. As expected, the most negative rates (fastest drying) occur soon after rain events. Although there is considerable noise within each daily bin, median values for each day and measurement type reveal two important differences. First, the frequency of soil moisture observations does not affect the calculated drying rate: observations up to 3 days apart ($\text{inSitu}_{\text{SMAP}}$) yield rates consistent with those calculated from daily data ($\text{inSitu}_{\text{daily}}$). Second, drying rates are faster when calculated from SMAP than from $inSitu_{daily}$. In days 1 through 6, median drying rates are 1.6, 2.7, 2.4, 2.1, 1.7, and 1.6 times greater, respectively, for SMAP than $inSitu_{daily}$ (mean: 2.0). There is no apparent difference between SMAP and $inSitu_{daily}$ drying rates after day 6. Similar differences exist when SMAP and $inSitu_{SMAP}$ are compared.

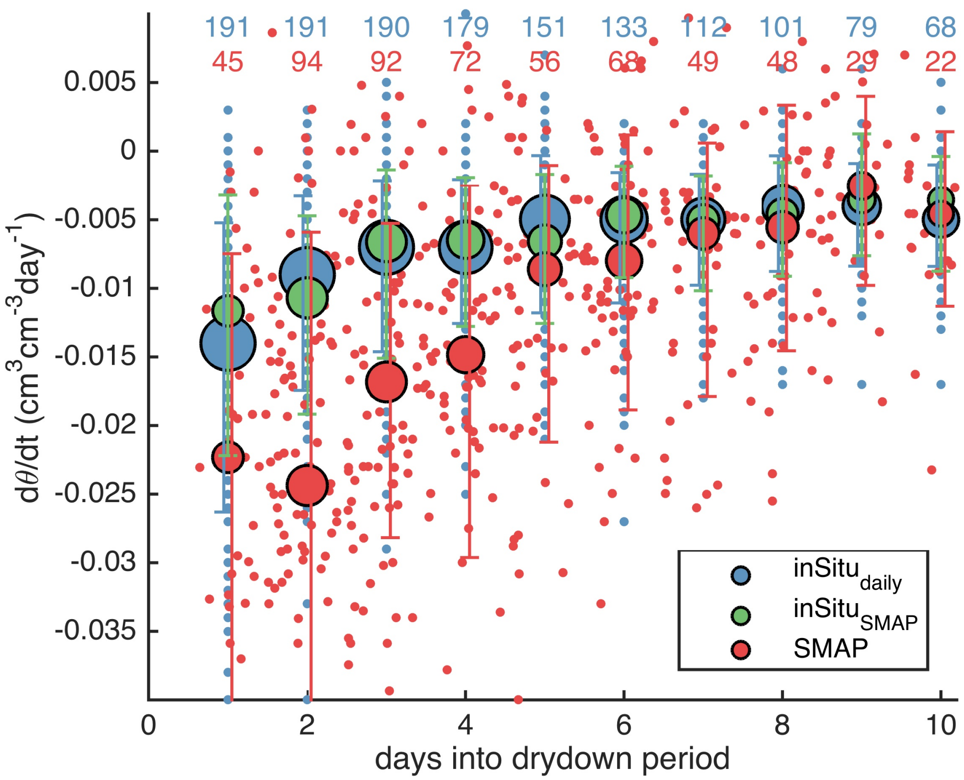

Figure 40: Drying rates calculated from $inSitu_{daily}$ (blue), $inSitu_{SMAP}$ (green), and SMAP (red) as a function of time into the drydown period.
Small markers show all data for $inSitu_{daily}$ and SMAP. Large markers show the median of each observation type in each daily bin. Large marker sizes correspond to the number of data points in each bin, which is also shown at the top of the figure. Error bars indicate +/- 1 standard deviation around the mean (mean not shown).

The drying rate results are consistent with the exponential model analysis. Compared to $inSitu_{all,}$ exponential fits to SMAP exhibit shorter median timescales and greater median magnitudes of drying (Table 7). These differences require that SMAP observes faster drying rates over the interval during which a majority of the soil drying occurs.

3.4 Discussion and Conclusions

Meeting the SMAP validation goal (ubRMSE $\leq$ 0.04 cm^3 cm^{-3}) at CVS does not guarantee that the dynamics of drying events determined from SMAP are accurate, especially given the difference in observation depth between satellite radiometer and *in situ* probes. Quantifying differences that exist is important for both data assimilation applications and model verification studies that utilize SMAP soil moisture.

The exponential model used here characterizes the timescale and magnitude of 63 soil moisture drydowns across 17 sites. The SMAP soil moisture data yield exponential drying timescales that are approximately half (44%) those determined from watershed-averaged *in situ* observations. In addition, the magnitude of SMAP drying is 35% greater than that of the *in situ* networks. Direct calculation of drying rates between consecutive observations corroborates that SMAP and *in situ* soil moisture observations exhibit different behavior. In the 6 days following the rain events (approximately the median exponential drying timescale), surface soil moisture measured by SMAP decreases twice as fast as that measured by *in situ* probes. Drying rates are effectively equal at longer intervals (>6 days) after rainfall. The differences between SMAP and *in situ* dynamics are not due to the timing and frequency of SMAP observations; the subset of *in situ* observations concurrent with SMAP yields nearly identical results as its high-frequency counterpart.

SMAP and *in situ* probes measure drying behavior differently because they are sensitive to soil moisture at different depths. L-band radiometer measurements are sensitive to soil water between the surface and a moisture-dependent depth, usually 5 cm or less [e.g., *Njoku and Kong*, 1977]. The *in situ* probes at 15 of the 17 CVS, however, are centered at 5 cm, and thus do not measure soil moisture in the top several centimeters [*Rondinelli et al.*, 2015]. These differences in sensing depth lead to different characterizations of soil moisture drying. Rain events create positive vertical moisture gradients. The near-surface soil is wetter than deeper soil shortly after rainfall, but tends to dry more quickly due to evaporation and vertical redistribution [e.g., *Schneeberger et al.*, 2004]. Moreover, L-band sensing depth for very wet soil may be as little as ~1 cm [*Escorihuela et al.*, 2010], further accentuating the combined effects of vertical soil moisture gradients and different sensing depths. The two Australia sites yield similar results to those from other sites, despite having vertically-inserted probes, possibly because the soil depth observed by the probes is still deeper than SMAP penetration depth. In addition, the sensor head may shelter rain [*Adams et al.*, 2015], making probe observations drier than SMAP retrievals until the soil equilibrates.

Results are consistent with those from SMOS [*Rondinelli et al.*, 2015; *Champagne et al.*, 2016], suggesting that shortened drydowns may be an issue for any L-band instrument. It is also possible that non-uniform rainfall within the validation pixel could lead to different drying dynamics, which should be evaluated in future studies.

Hydrologic applications and studies that utilize SMAP soil moisture must consider the differences in sensing depth, drying timescale, and drying rate discussed here. Results from this chapter can help guide efforts to optimize the usefulness of SMAP observations. In addition, these results provide a starting point for investigations into the role that other tools (LSMs, novel remote sensing platforms, bias correction methods) play in characterizing soil moisture dynamics.

Chapter 4: Factors affecting SMAP and Noah drying rates

4.1 Background

Soil moisture constitutes a key component of land surface hydrology. Though the volume of water is small, surface soil moisture generates outsized effects on the global water and energy balance [*McColl et al.*, 2017]. Climate, weather, and flood predictions depend on soil moisture [*Entekhabi et al.*, 1996; *Viterbo and Betts*, 1999]. Feedback between the land and atmosphere can perpetuate soil and atmospheric anomalies differently depending on the climatic regime [*Koster et al.*, 2004; *Tuttle and Salvucci*, 2016].

Precipitation wets a given parcel of soil from above. Consequently, there are two avenues by which the moisture may dissipate: (1) water moves back into the atmosphere (evapotranspiration), or (2) water moves deeper into the ground (drainage and diffusion). Evapotranspiration can be split between direct evaporation from the ground and evaporation from plant stomata (transpiration, Figure 41) [*Campbell and Norman*, 1998; *Monteith and Unsworth*, 2013]. Because rooting depths often reach 100 cm or deeper [*Schenk and Jackson*, 2002], we expect transpiration to play a role any time evaporation is occurring and vegetation is present.

To evaporate water, energy is required to overcome the latent heat of vaporization, and a vapor sink is required for the atmosphere to absorb it. Over open water or bare soil, these processes depend on surface vapor pressure, atmospheric vapor pressure, surface temperature, atmospheric temperature, radiation, albedo, and wind velocity [*Penman*, 1948; *Mahrt and Ek*, 1984]. This quantity is the potential evaporation (PE) rate. Evaporation from vegetated areas must further be scaled by the aerodynamic resistance required to move vapor from the ground or stomata into the atmosphere [*Wang and Dickinson*, 2012].

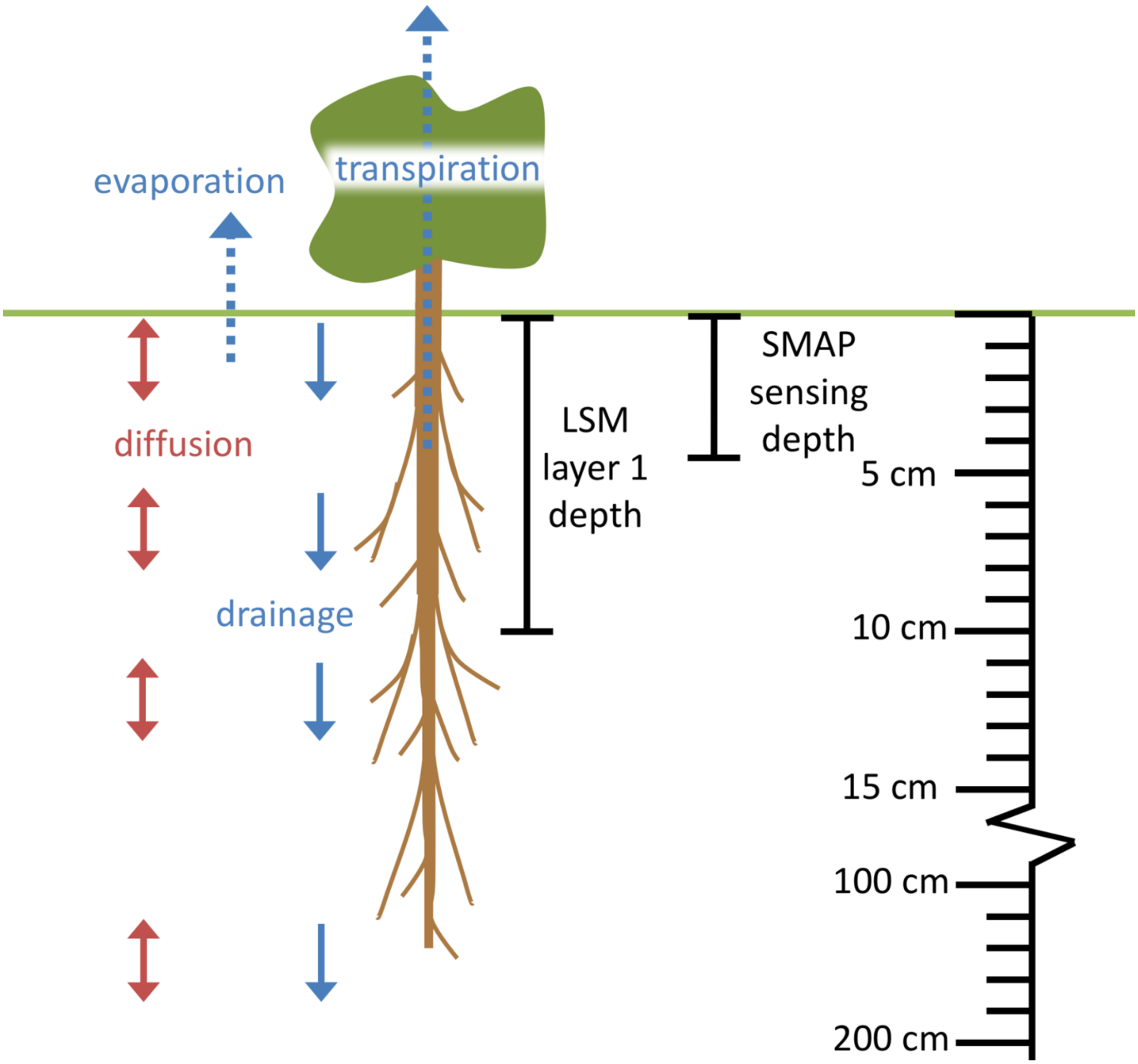

Figure 41: Cartoon showing processes contributing to drying and the depths that SMAP and the Noah LSM represent

Of course, evapotranspiration also depends on the moisture supply (moisture stress) in the soil. Moisture is commonly quantified as the volume of water divided by the volume of soil in which that water resides. This is called volumetric soil moisture (VSM), and its units are cm^3 cm^{-3}. In the Noah LSM and other common LSMs, moisture stress for a bare surface is represented as a three-stage function that depends on two VSM thresholds. Above field capacity, evaporation proceeds at its potential rate (stage 1 evaporation); below a residual soil moisture content, no evaporation occurs; between the two thresholds, evaporation depends on relative moisture content (stage 2 evaporation) [*Allen*, 2000; *Chen and Dudhia*, 2001].

Vegetated surfaces introduce two counteracting effects that are absent from bare surfaces. Evaporation decreases because of shading from the canopy that intercepts solar radiation [*Mahfouf and Noilhan*, 1991], and transpiration is introduced, which can draw moisture from the root zone. (Transpiration rates depend on type of vegetation, soil moisture content, and atmospheric state [*Chen and Dudhia*, 2001]).

Drainage and diffusion are assumed to be negligible in our study. This simplification implies that wetting fronts infiltrate through the root zone in less time than the model time step spans (for us, the time steps are the one or more days between SMAP observations), and that any further diffusion is negligible compared with evapotranspiration rates. This is a common assumption in models of soil moisture dynamics [e.g., *Laio et al.*, 2001; *Guswa et al.*, 2002; *Federer et al.*, 2003; *Porporato et al.*, 2004], and we adopt it as well.

NASA's SMAP (Soil Moisture Active Passive) mission has been providing global observations of surface soil moisture content since March 2015. In this study, by analyzing SMAP and precipitation data together, we provide estimates of how long water remains near the land surface after a rain event. We expect the driving mechanisms behind SMAP drying rates to be similar to those described above. For comparison, we also look at how such mechanisms affect simulations from the Noah LSM, a model that incorporates the aforementioned findings from the literature into its structure and parameters [*Ek et al.*, 2003; *Xia et al.*, 2012a].

We expect there to be differences between SMAP observations and Noah simulations. The goal of both is to provide information that reflects the real world. Previous work has shown that SMAP achieves its mission goal of 0.04 $cm^3\ cm^{-3}$ unbiased root mean squared error (ubRMSE) compared with its *in situ* validation network [*Chan et al.*, 2016; *Colliander et al.*, 2017]. However, during rain-free periods, soil moisture decreases faster and over a shorter time period as observed by SMAP than *in situ* [*Shellito et al.*, 2016b]. The discrepancies in drying rates are likely because SMAP and *in situ* networks observe slightly different soil moisture depths. To prevent *in situ* probes from being disrupted by fauna or farm equipment and exposed to the atmosphere, they are typically centered at no less than 5 cm depth, meaning they measure soil moisture content between 3.5 and 6.5 cm [*Rondinelli et al.*, 2015]. SMAP nominally represents 0-5 cm soil moisture, but penetration depth can be less, especially when water content is high [*Njoku and Kong*, 1977; *Escorihuela et al.*, 2010; *Jackson et al.*, 2012]. Though this difference complicates validation efforts, SMAP nonetheless presents an opportunity to assess shallow soil moisture dynamics, which is our goal here. Continuous, continent-wide *in situ* observations do not exist, so we make our comparisons instead against Noah simulations of 0-10 cm soil moisture (its shallowest soil layer). The difference between SMAP sensing depth and Noah simulation depth is expected to result in drying dynamics that are different in a similar way as SMAP and *in situ* dynamics are different [*Shellito et al.*, 2016b]: slower, longer drying periods for the model than for SMAP.

We focus our investigation on North America, using SMAP observations, meteorological forcing data from the National Land Data Assimilation System (NLDAS), simulated data from the Noah LSM, and vegetation data from the Moderate Resolution Imaging Spectroradiometer (MODIS). Both NLDAS and Noah data are are available on a 1/8 degree grid covering North America [*Xia et al.*, 2012b]. SMAP and NDVI are available globally [*Entekhabi et al.*, 2014; *NASA LP DAAC*, 2016].

With these tools, we quantify the controls on SMAP and Noah soil moisture drying rates after rain events. The existing framework for understanding soil drying rates includes two hypotheses we will address. (1) Soil texture exerts some control on drainage rates and readily evaporable water [*Allen*, 2000; *Santanello et al.*, 2007; *Xia et al.*, 2015]. (2) Evaporation is controlled by meteorology and water availability [*Monteith and Unsworth*, 2013].

4.2 Materials and Methods

4.2.1 Data

4.2.1.1 SMAP retrievals

The SMAP mission was launched in January 2015 and provides morning and evening (6 AM and 6 PM local time, respectively) estimates of VSM, in $cm^3\ cm^{-3}$, between 0 and 5 cm globally every 1-3 days [*Entekhabi et al.*, 2014]. Retrievals are indirect estimates of soil moisture based on passive microwave (1.41 GHz) brightness temperature as described in *Entekhabi et al.* [2014]. We use the "enhanced" level 3 soil moisture data product, version 1, which is available from the National Snow and Ice Data Center. The SMAP radiometer has a native spatial resolution of 36 km but this product utilizes the Backus-Gilbert optimal interpolation algorithm to post soil moisture retrievals onto the 9 km Equal-Area Scalable Earth grid ver. 2 (EASE-2) [*O'Neill et al.*, 2016]. We use only AM overpasses because the SMAP algorithm assigns only one temperature to both the soil and its overlying canopy, a condition that is best met in the morning hours [*Jackson et al.*, 2012; *Entekhabi et al.*, 2014]. We exclude data that have been flagged for uncertain quality due to dense vegetation (>5 kg/m^2), mountainous terrain (>3° slope standard deviation), and >5% of the sensing area comprising frozen ground, snow, ice, precipitation, or static water. These exclusions decrease the number of SMAP observations by 56.5% (mostly because of vegetation in the eastern portion of North America). Figure 42 (top panel) shows the number of SMAP observations between March 31, 2015 and January 27, 2017, after removing flagged data. These are the observations used in this study.

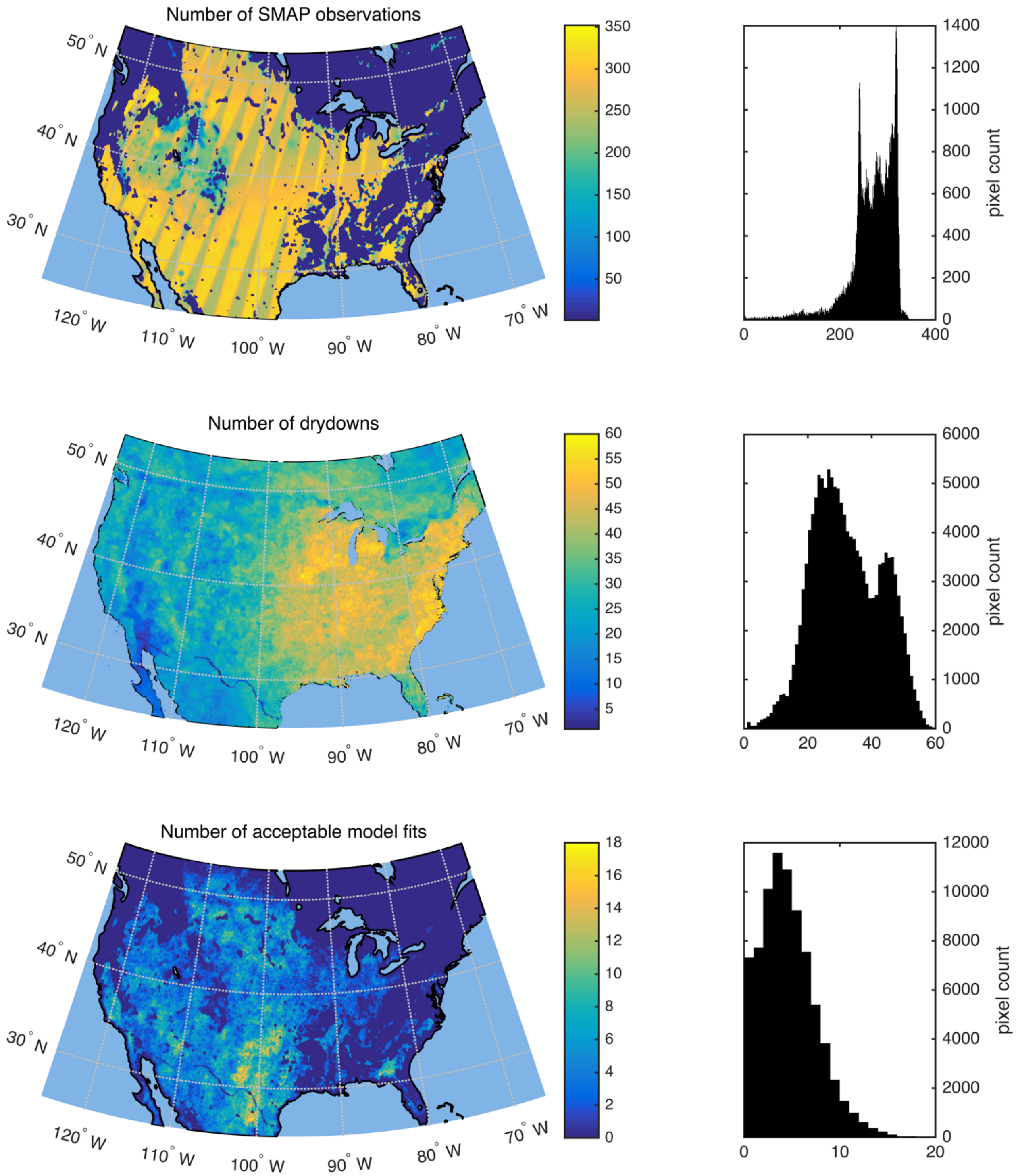

Figure 42: Distribution of SMAP observations (top), the number of drydowns calculated from NLDAS precipitation forcing (middle), and the number of acceptable model fits (bottom) in the study domain

4.2.1.2 NLDAS Primary Forcing

We use surface meteorological data (precipitation, solar radiation, long-wave radiation, specific humidity, temperature, pressure, wind speed, and potential evaporation [PE]) from the NLDAS-2 primary (default) forcing fields [*Xia*, 2009; *Xia et al.*, 2012b]. These data have been derived from the National Center for Environmental Prediction (NCEP) North American Regional Reanalysis (NARR), interpolated to the NLDAS 1/8th-degree grid and disaggregated to hourly frequency [*Cosgrove et al.*, 2003].

As described in *Xia et al.* [2012b], NLDAS rainfall is supplemented with the NCEP Climate Precdiction Center's unified gauge-based precipitation, which has been adjusted for orographic effects [*Daly et al.*, 1994]. Shortwave radiation is adjusted using satellite-derived radiation to remove a known positive bias [*Pinker et al.*, 2003].

PE is calculated using the modified Penman scheme of *Mahrt and Ek* [1984]. This equation uses air temperature, wind speed, net radiation, specific humidity, and a surface exchange coefficient that depends on the atmospheric stability [*Mahrt and Ek*, 1984]. Using the specific humidity and temperature fields, we have also calculated the vapor pressure deficit using equations 2.9 and 2.17 of *Shuttleworth* [2012].

Within the United States, NLDAS also provides a gridded soil texture product derived from 1-km State Soil Geographic (STATSGO) data [*Miller and White*, 1998; *Mitchell et al.*, 2004]. Figure 43 shows that although there are 15 categories, some types (silt, sandy clay loam, sandy clay, silty clay, organic materials, water, and bedrock) all occupy less than 3% of the domain. We therefore focus on the dominant 8 textures: loam (26.0%), silt loam (25.9%), sandy loam (23.0%), sand (6.8%), silty clay loam (4.2%), clay loam (4.1%), loamy sand (3.6%), and clay (3.4%).

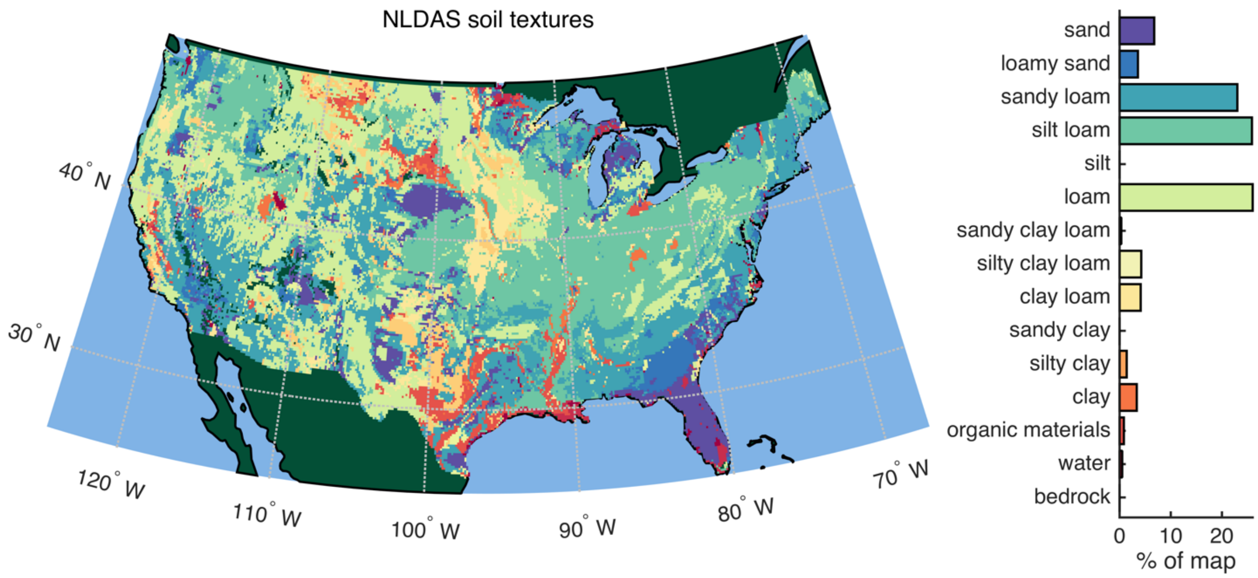

Figure 43: Soil textures according to NLDAS.

4.2.1.3 NLDAS Noah simulations

The meteorological data described in 4.2.1.2 are used to force the Noah LSM [*Chen and Dudhia*, 2001] from 1979 to present as part of the NDLAS-2 project [*Xia et al.*, 2012b]. The simulations use a climatologically-based parameter to define fractional vegetation cover. The shallowest soil layer in the Noah LSM is 0-10 cm, which is different from the SMAP retrieval depth of 0-5 cm (Figure 41). We have obtained Noah simulations of 0-10 cm soil moisture, 0-10 cm soil temperature, soil surface (skin) temperature, fractional vegetation cover, and potential evapotranspiration data from the Goddard Earth Sciences Data and Information

Services Center (GES DISC) [*Xia*, 2012]. Soil moisture values are converted from kg/m^2 to $cm^3\ cm^{-3}$ to be consistent with SMAP units.

4.2.1.4 Vegetation data

NASA's Terra and Aqua satellites carry the MODIS instrument and provide Normalized Difference Vegetative Index (NDVI) data every 16 days globally [*NASA LP DAAC*, 2016]. The data have a resolution of 1 km and have been linearly interpolated in the days between retrievals.

4.2.1.5 Domain

Our study utilizes SMAP and NLDAS data from the nearly two-year period since SMAP began operation: March 31, 2015, through January 27, 2017.

Although SMAP and NDVI data are available globally, the NLDAS forcing and simulation data cover only North America. Therefore, our study is limited to the domain found between longitudes 124.9° and 67.1° West and latitudes 25.1° and 52.9° North (Figure 42). This area consists of 189,720 SMAP pixels and 103,936 NLDAS pixels. Approximately ¼ of the domain is ocean and is excluded. Of the remaining 136,422 SMAP pixels, 59% have at least one non-flagged observation. We focus our analysis on these 79,987 "active" SMAP pixels.

4.2.2 Methods

4.2.2.1 Matchup of NLDAS and MODIS pixels to SMAP pixels

Our study requires linking SMAP observations with MODIS NDVI observations, NLDAS meteorology, and NLDAS Noah simulation data. Each SMAP pixel is matched with the NLDAS or MODIS pixel that contains the center point of the SMAP cell.

Because the SMAP grid is finer than the NLDAS grid, multiple SMAP pixels will at times correspond to the same NDLAS pixel. Though this is not ideal, it is preferable to basing our analysis on the NLDAS grid, which would force us to exclude some SMAP pixels or blend them with their neighbor when they fall within the same NLDAS pixel. In this way, we keep SMAP as the focus of this study. Moreover, the meteorological and model data from NLDAS are spatially and temporally continuous, so it is expected that neighboring SMAP grid cells should have similar (if not identical) NLDAS data associated with them.

The MODIS grid is finer than the SMAP grid, and we assign each SMAP pixel the NDVI value closest to its center point.

4.2.2.2 Drydown periods

We utilized the precipitation field in the NLDAS forcing dataset to select drydowns for our analysis. Following *Shellito et al.* [2016b], a drydown is a period of dry weather that follows a soil wetting event. We automate this selection process for all NLDAS pixels according to the following logic: 1) the event precipitation volume must surpass 5 mm in a 24-hour period; 2) the dry period must begin after the event precipitation stops and end a day before 3 mm or more additional precipitation accumulates; and 3) the dry period must be at least 3 days long.

The spatial distribution of the number of drydowns is shown in Figure 42 (middle). We anticipate some errors in the NDLAS precipitation dataset, so our analyses require excluding some drydowns as detailed in the following section.

4.2.2.3 Calculation of drying timescales

We calculate a drying timescale for the drydowns identified in 4.2.2.2. Timescales are estimated by fitting an exponential decay model [*Kurc and Small*, 2004; *Rondinelli et al.*, 2015; *Shellito et al.*, 2016b] to the soil moisture values as they dry out:

$$\theta(t) = A * e^{\left(-\frac{t}{\tau}\right)} + \theta_f \ . \tag{7}$$

θ is surface soil moisture content ($cm^3\ cm^{-3}$), t is time since the beginning of the drydown (days), and A, τ, and θ_f are empirically-determined fitting parameters indicating, respectively, the magnitude of soil moisture drying ($cm^3\ cm^{-3}$), the exponential time constant (days), and a final soil moisture content ($cm^3\ cm^{-3}$).

Our analysis focuses on the τ values that result from a least squares fitting of the above model parameters to SMAP soil moisture retrievals. We include in our analysis only model fits where (1) τ parameter uncertainties at the 67% significance level (one standard deviation) do not include zero, (2) RMSE values between the model and the observations are less than 0.012 $cm^3\ cm^{-3}$ (90^{th} percentile), and (3) model R^2 values are above 0.8 (10^{th} percentile). We define these models as "acceptable." Unacceptable model fits can result from noisy or erroneous forcing data or not enough observations in the drydown period. (Because the model has three parameters, if there are two or fewer observations in a drydown, we do not even attempt a fit.) Changing these criteria thresholds does not change the overall results.

We also fit the model to surface soil moisture as simulated by Noah in NLDAS. To maintain consistency and facilitate comparisons, we utilize only those Noah observations that are concurrent with SMAP overpasses. Using all the Noah soil moisture observations would not substantially change the parameter values [*Shellito et al.*, 2016b].

Our analysis includes only models that have been acceptably fit to both SMAP and Noah soil moisture. These restrictions ensure consistency in our comparisons between SMAP and Noah model fits and minimize any effects of forcing data errors. The geographic distribution of the 331,957 models that have been acceptably fit to both SMAP and Noah is shown in Figure 42 (bottom).

To summarize the resulting τ parameter values, we use histograms that have been passed through a kernel smoothing function, resulting in an empirical probability density function (ePDF). We select kernel bandwidths of 0.24 and 0.60 for to SMAP and Noah τ distributions, respectively. This provides appropriate smoothing resolutions as shown for SMAP data in Figure 44. The maximum τ probability is the location of the ePDF peak (in this case, 2.22 days). The ePDFs represent the τ distributions quite well in both and will be used without the underlying histogram in subsequent figures.

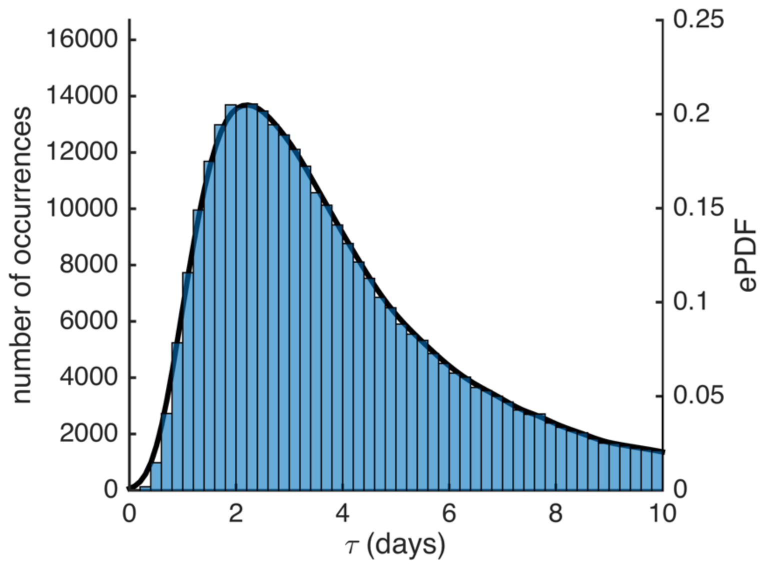

Figure 44: τ histogram and ePDF for all models fit to SMAP data.

4.2.2.4 Calculation of drying rates

As a non-parametric alternative to the drydown timescales in 4.2.2.3, we also use a finite differences approach to calculate soil drying rates during the drydown periods [*Shellito et al.*, 2016b]:

$$\frac{d\theta}{dt} = \frac{\theta_{n+1} - \theta_n}{t_{n+1} - t_n}. \tag{8}$$

n and *n+1* correspond to consecutive observations. This analysis produces 4,738,702 SMAP drying rates, or an average of 75.2 per active SMAP pixel. By multiplying by the SMAP sensing depth (50 mm [*Entekhabi et al.*, 2014]), we are left with an estimate of the depth of water leaving the top 5 cm of soil through evapotranspiration, diffusion, or infiltration each day. Preliminary analyses showed that SMAP observations can at times reach and stay at a maximum value, near 0.5 $cm^3\ cm^{-3}$, producing drying rates of exactly 0 mm/day. This is an artifact of the SMAP algorithm and does not reflect the drying process. These cases have been removed.

For comparison, we also determine the concurrent Noah drying rates. Since Noah represents soil moisture between 0 and 100 mm, we obtain Noah drying rates in mm/day by multiplying by 100 mm. Thus, Noah drying rates correspond to the depth of water leaving the top 10 cm of soil each day, which is twice the thickness of the SMAP sensing depth. Because we are assuming that diffusion and drainage between layers is negligible, this drying rate approximates the total evapotranspiration out of the top layer of the model. A scatter plot between Noah drying rates and Noah layer 1 evaporation confirms this (Figure 45). Because there are over 400,000 points, we scale point densities by color instead of showing them individually. Hotter locations correspond with higher point densities. The data nicely track the 1:1 line.

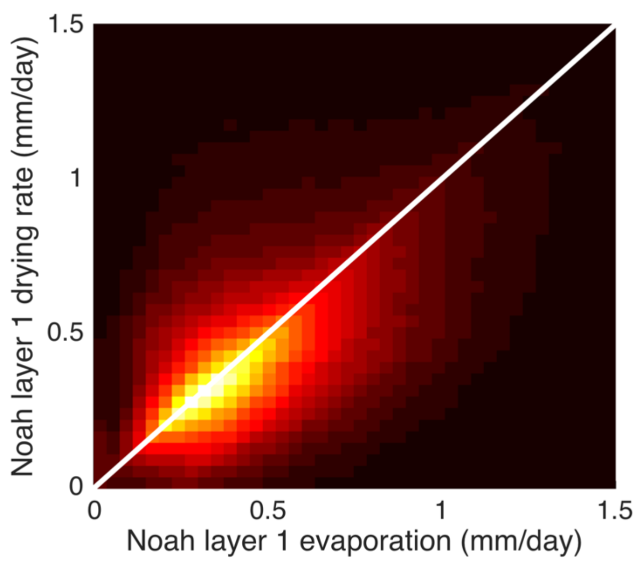

Figure 45: Scatter plot showing Noah layer 1 drying and evaporation rates. Hot colors indicate higher point densities. 1:1 line shown in white.

Drying rates are expressed in absolute terms (mm H_2O/day) and as a fraction of PE, which indicates evaporative efficiency (the fraction of the potential that is realized by water leaving the top 5 or 10 cm). Our analysis of these data includes determining how drying rates relate to soil moisture content (θ_n) in each observation pair, in addition to the factors listed in 4.2.2.5.

4.2.2.5 Effects of meteorologic conditions and land surface states

We quantify the effects of meteorologic conditions and land surface states on drying dynamics by using the NLDAS forcing and NDVI retrievals described in 4.2.1.2 and 4.2.1.4. For each quantity, we record the arithmetic mean through the extent of either the exponential decay model (from cessation of rainfall to the time of the last soil moisture observation) or the drying rate calculation (from t_n to t_{n+1}).

With these data, we can provide continent-wide summaries of the effect of each environmental state on the drying dynamics. We assess the role of environmental data by dividing them into quantiles and comparing fitted τ values and surface drying rates. In each case, either the entire distribution is shown, or bootstrapping is employed to estimate the median value and its standard error. Those parameters are displayed as markers with error bars in our figures. Bootstrapped statistics are generated using 500 instances of 100 random samples.

4.3 Results

4.3.1 Drying timescales

The drying timescales as observed by SMAP and simulated by Noah are quite different. Figure 46 (left) shows that SMAP drying timescales are short, with a maximum τ probability of 2.2 days. Noah has a wider distribution of drying timescales and a maximum τ probability of 4.8 days, 118% longer than SMAP timescales. Figure 46 (right) is a scatter plot that shows the how each drydown event is observed by the satellite and the model. The most common τ pairs (white hot) are consistent with the ePDFs: 2.06 and 4.06 days, respectively. However, we do not see a linear feature in the scatter plot, which means that the longest drydowns as observed by SMAP do not correspond with the longest drydowns as simulated by Noah, and vice versa. This indicates that in at least these cases, there are different mechanisms at work.

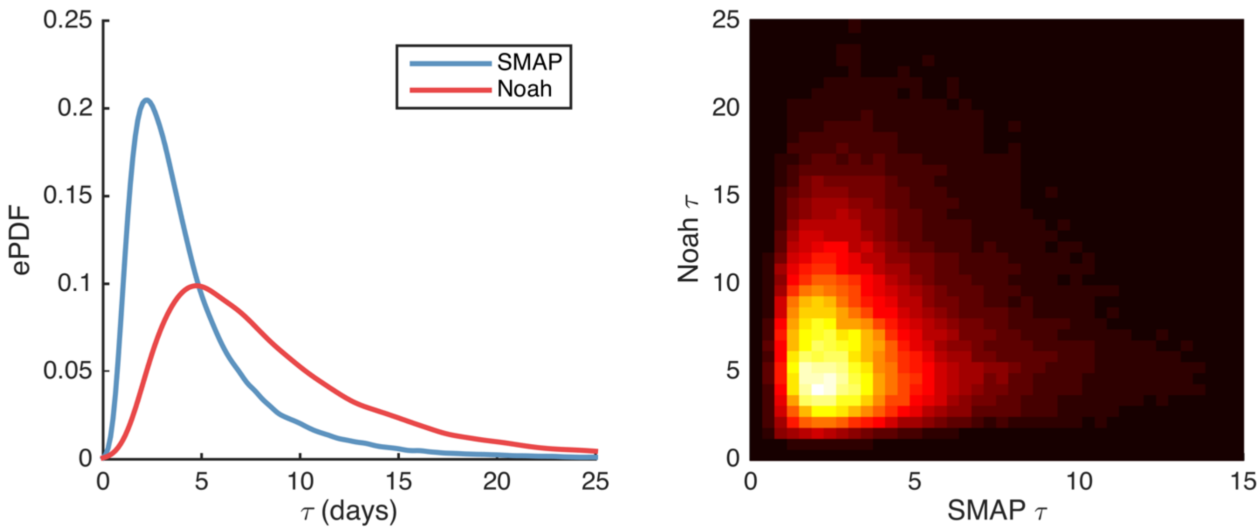

Figure 46: ePDFs (left) and scatter plot (right) comparing SMAP and Noah τ values. Hot colors indicate higher point densities.

In the next sections, we investigate the role that four environmental factors play in controlling the τ distributions: geography, soil texture, vegetation, and PE.

4.3.1.1 Role of geography

The distributions of τ fit to SMAP and Noah vary according to region (Figure 47, top and middle). These plots use a 25-pixel moving window to smooth the τ values. Displayed are median values from each window that contain at least 50 acceptable model fits. Because maximum τ probabilities in models fit to Noah are approximately double those fit to SMAP, we have adjusted the color scaling to emphasize regions that deviate from that multiplier. There are two main regions where SMAP and Noah drying timescales disagree: interior high latitudes, where SMAP has relatively longer drying timescales than Noah, and arid southern and western regions, where the opposite is true. The best agreement is found the southeast and much of the Great Plains.

The bottom panel of Figure 47 shows the mean NDVI values throughout the sensing period. Visual inspection suggests a positive correlation between SMAP drying timescales and NDVI, with the lowest values for both located in the High Plains, West and Southwest. In contrast, the shortest drying timescales from Noah simulations are located at high latitudes and span a range of NDVI values. We further explore the relationship between NDVI and drying dynamics below, in sections 4.3.1.4 and 4.3.2.2.

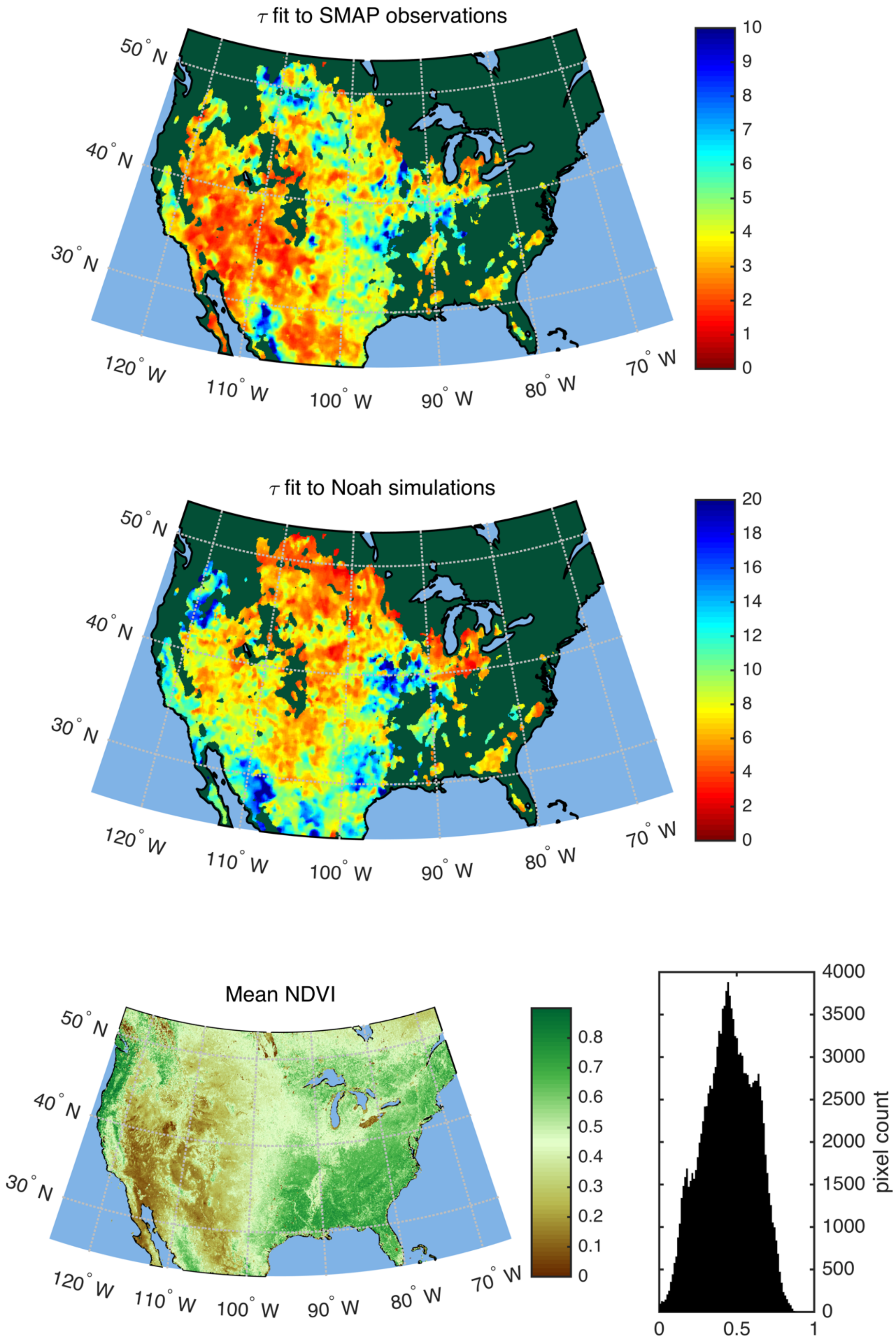
τ fit to SMAP observations
50° N
40° N
30° N
120° W
110° W
100° W
90° W
80° W
70° W
0
1
2
3
4
5
6
7
8
9
10
τ fit to Noah simulations
50° N
40° N
30° N
120° W
110° W
100° W
90° W
80° W
70° W
0
2
4
6
8
10
12
14
16
18
20
Mean NDVI
50° N
40° N
30° N
120° W
110° W
100° W
90° W
80° W
70° W
0
0.1
0.2
0.3
0.4
0.5
0.6
0.7
0.8
pixel count
0
500
1000
1500
2000
2500
3000
3500
4000
0
0.5
1

Figure 47: Distributions of τ fit to SMAP (top) and to Noah (middle). Bottom shows mean NDVI.

4.3.1.2 Role of soil texture

Soil texture plays a role in the distributions of drying timescales for models fit both to SMAP and to Noah (Figure 48). The maximum probabilities of each ePDF are listed in Table 8.

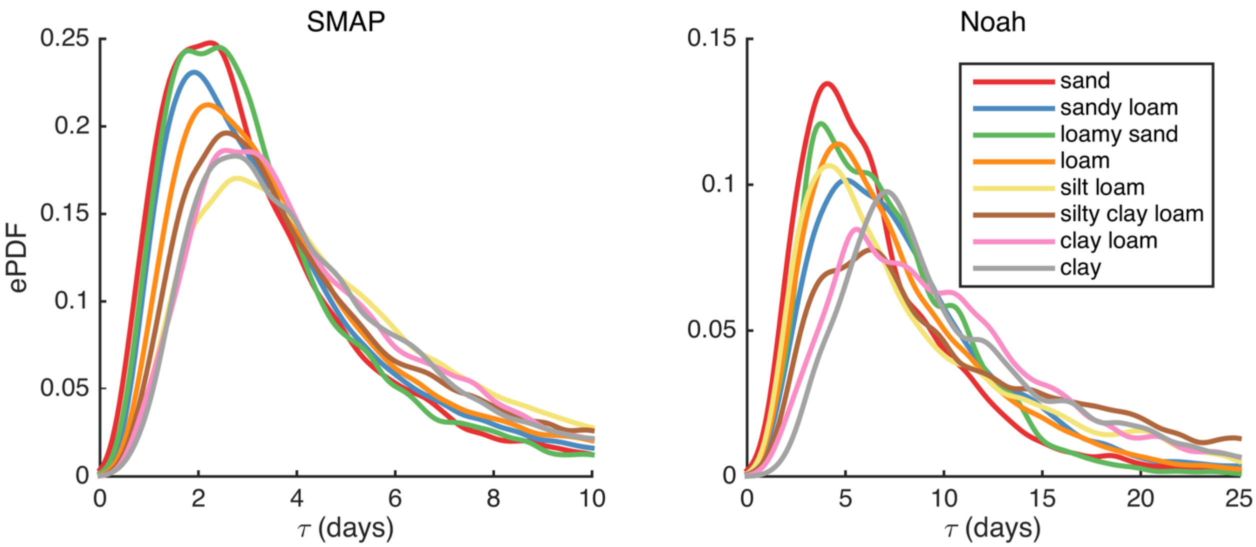

Figure 48: ePDFs of τ distributions in the most prevalent soil textures as fit to SMAP observations and Noah simulations.

Table 8: Maximum τ probabilities for the four most prevalent soil textures.

	Peak τ in models fit to	
	SMAP	Noah
Sand	2.24	4.01
Sandy loam	1.91	5.02
Loamy sand	2.41	3.76
Loam	2.21	4.60
Silt loam	2.78	4.18
Silty clay loam	2.58	6.27
Clay loam	2.54	5.52
Clay	2.74	7.11

For τ values fit to both SMAP and Noah, the shortest drying timescales are found in relatively coarse-grained textures (sandy loam and loamy sand, respectively), and the longest drying timescales are found in fine-grained textures (silt loam and clay, respectively). Fine-grained soils (clay, clay loam, silty clay loam, silt loam) also tend to have thicker tails than coarse-grained soils (sand, sandy loam loamy sand, loam), which is consistent with the expectation that fine-grained soils retain more water at the same water tension levels than coarse-grained soils do [*Saxton et al.*, 1986].

The major difference between the role of soil texture on SMAP observations compared to Noah simulations is the degree of the effect. The difference between the shortest and longest SMAP drying timescales is 46% (1.91 days vs. 2.78 days). The difference between the shortest and longest Noah drying timescales is 89% (3.76 days vs. 7.11 days).

4.3.1.3 Role of PE

PE reflects the readiness by which the atmosphere can take up moisture, so we expect soil drying rates to be affected by PE rates. To quantify its role on drying timescales, all τ values have been separated into three quantiles (terciles) according to their associated NLDAS PE rates. (PE depends on atmospheric conditions, so the terciles contain identical drydown events. The only difference is whether SMAP or Noah data are describing those events.) Figure 49 and Table 9 show that PE exerts a strong control over drying timescales as observed by SMAP and little control over drydowns as simulated by Noah. Moreover, the little effect that PE does have on Noah drying timescales is reversed from what would be expected: despite high atmospheric demand for moisture, the highest PE tercile is associated with Noah simulations that show water remaining in the soil for longer. For models fit to SMAP, there is a nearly two-fold difference in peak ePDF between the top and bottom terciles.

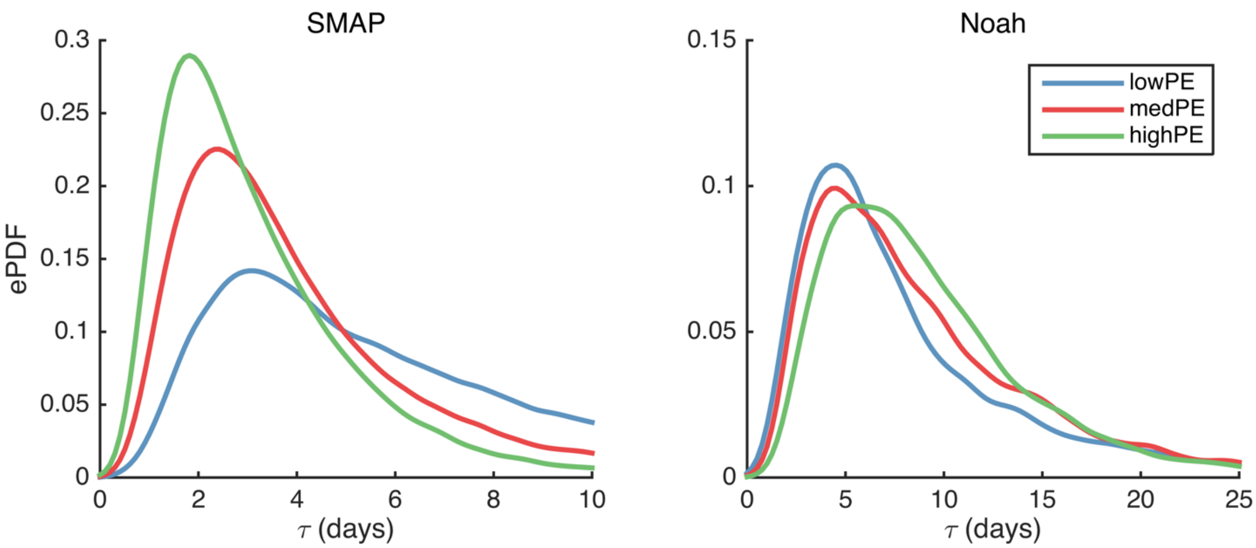

Figure 49: ePDFs of τ distributions for three terciles of PE rates as fit to SMAP observations and Noah simulations

Table 9: Maximum τ probabilities for each PE tercile.

	Peak τ in models fit to	
PE tercile	SMAP	Noah
Low	3.03	4.55
Medium	2.42	4.55
High	1.82	5.56

4.3.1.4 Role of vegetation

Visual inspection of Figure 47 suggests the existence of a relationship between average NDVI and SMAP drying timescales. Because vegetation varies throughout the year, we investigate this effect more closely by looking at the τ values associated with specific NDVIs.

We separate all NDVI values into ten quantiles (deciles). Figure 50 shows the median τ values from models fit to both SMAP and Noah in each decile. As NDVI increases, SMAP drydown timescales also increase, with the exception of the highest decile. This trend does not exist in the Noah drydown timescales. Instead, we see a widening of the distribution of Noah τ values with NDVI, as shown by the larger standard errors. The median values of τ fit to Noah show no monotonic trend. The strongest relationship both SMAP and Noah τ values have with vegetation is between 0.15 and 0.35 NDVI, where they exhibit opposite responses to increasing NDVI.

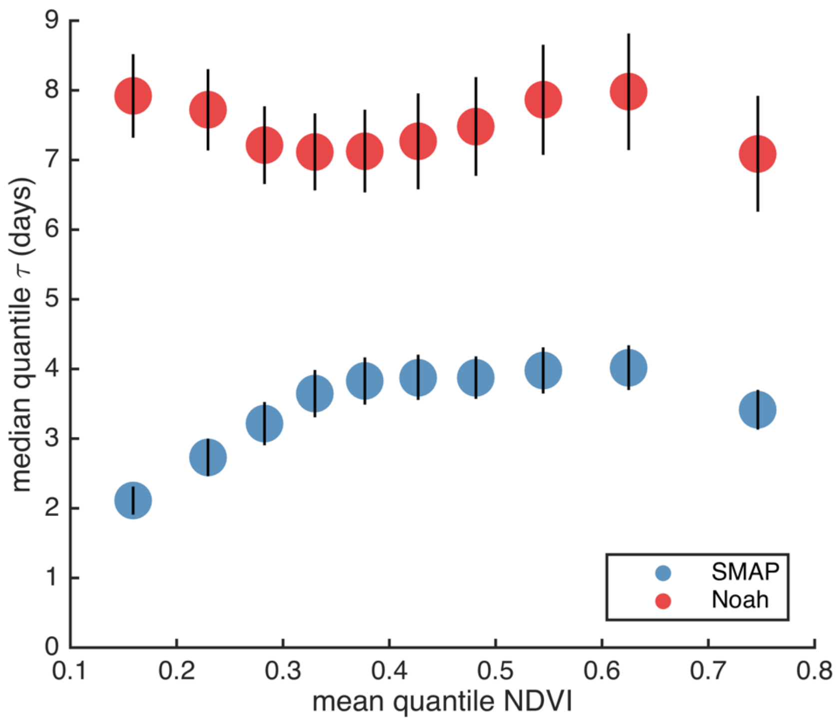

Figure 50: Median τ values and standard errors from each NDVI decile.

4.3.2 Drying rates

The trends shown in 4.3.1 are based on SMAP and Noah data that have been fit to an exponential decay model. We established the important variables, but there are some relationships in the data that warrant further investigation. Figure 51, Figure 52, and Figure 53 are scatter plots of the correlation between NDVI, PE, and soil moisture. Hotter colors indicate higher point densities. NDVI and PE are positively related (Figure 51) because both tend to be higher in the summer. Note that while the correlation is weak, high NDVI values are consistently collocated with high PE rates (spring and summer vegetation), and low PE rates are consistently collocated with low NDVI (winter). The third cluster is sites with high PE and low NDVI, which reflects desert conditions. NDVI and VSM have a positive correlation (Figure 52) because vegetation cannot grow where there is insufficient moisture. Finally, PE and VSM have a negative correlation (Figure 53), because when atmospheric demand is high, it will more readily remove moisture from the shallow soil.

Next, we present results that use calculated drying rates to investigate how PE, NDVI, and VSM affect soil moisture dynamics separately.

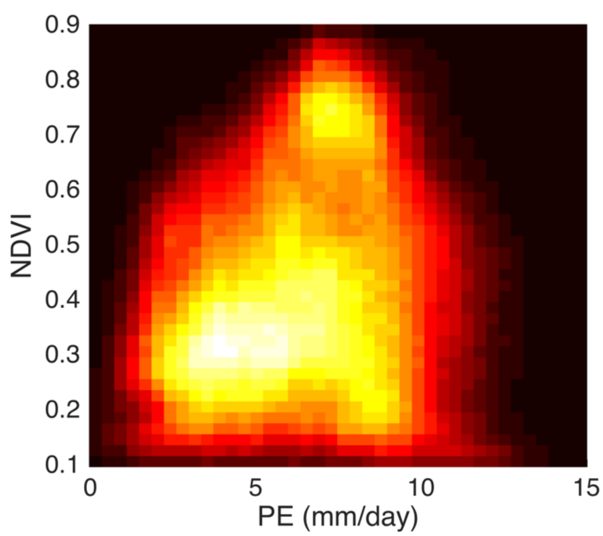

Figure 51: Scatter plot showing correlation of PE with NDVI. Pearson's R is 0.11. Hot colors indicate higher point densities.

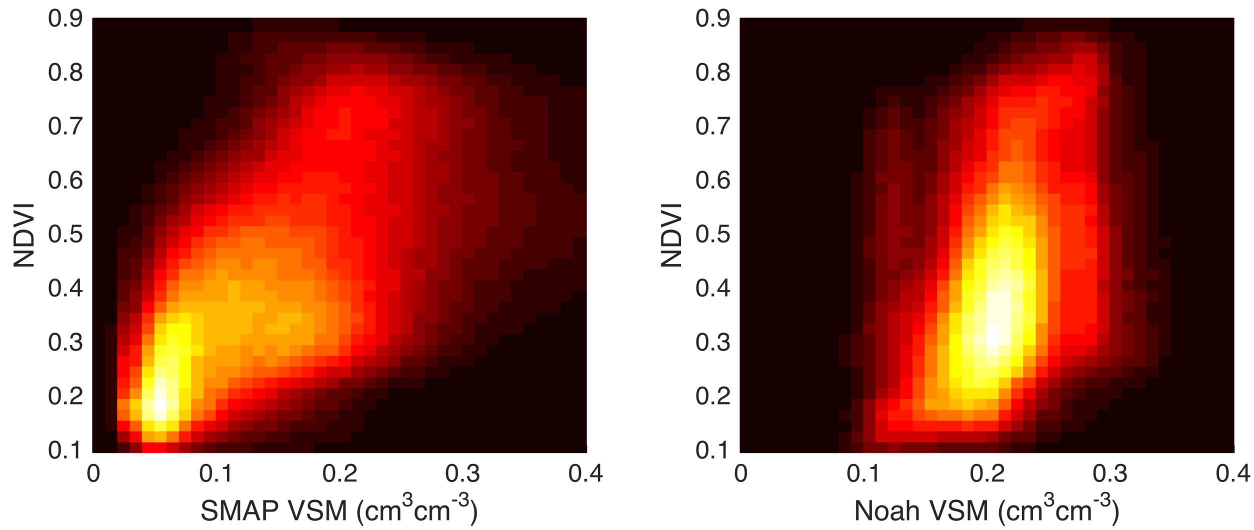

Figure 52: Scatter plots showing correlation of NDVI with VSM
from SMAP (left, R=0.49) and Noah (right, R=0.29). Hot colors indicate higher point densities.

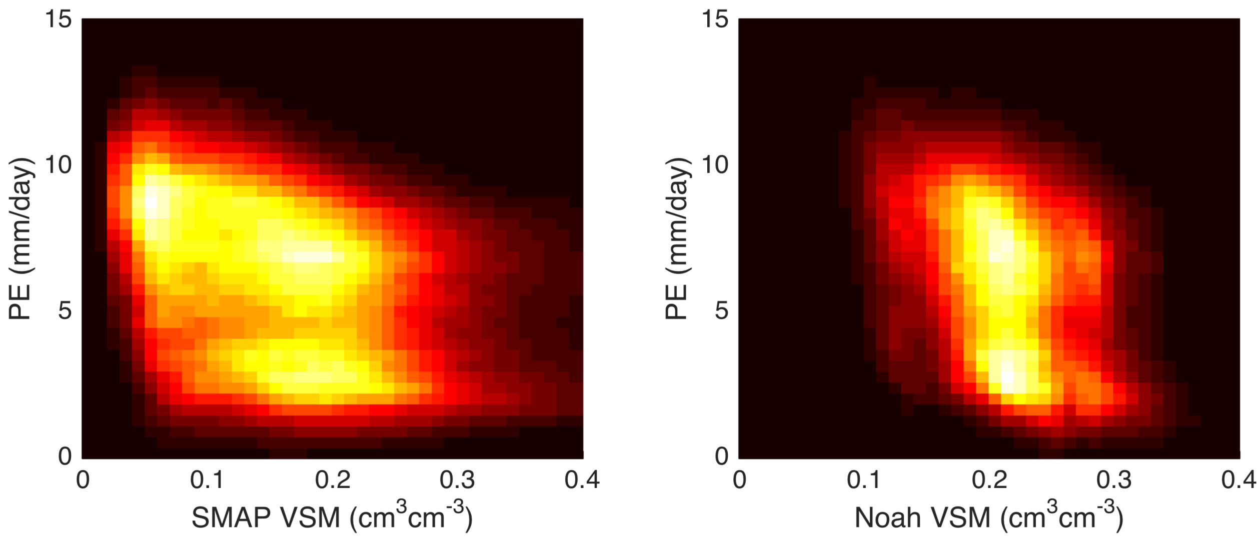

Figure 53: Scatter plots showing correlation of PE with VSM
from SMAP (left, R=-0.33) and Noah (right, R=-0.36). Hot colors indicate higher point densities.

4.3.2.1 Role of PE

We expect drying to be faster when more water exists in the soil. We also expect drying to be faster when PE is higher. Figure 54 shows how the two factors affect one another. We have divided the drying rates into terciles according to PE rate. We use 10 bins of increasing soil moisture content to further divide the data and plot the results in terms of drying rates (top) and evaporative efficiency (bottom).

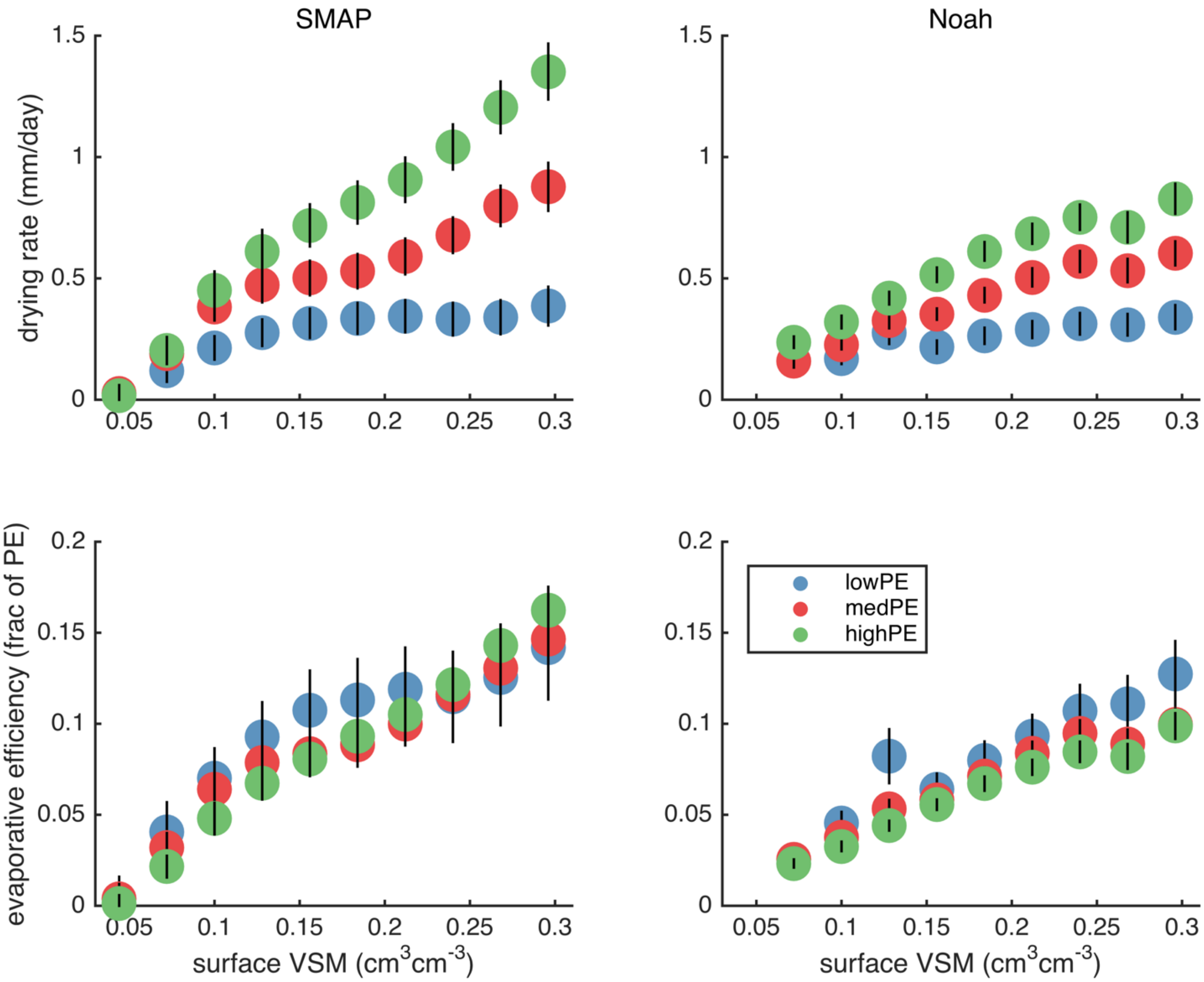

Figure 54: Drying rates (top) and evaporative efficiency (bottom) of surface soil moisture as a function of soil moisture content for low, medium, and high PE rates as observed by SMAP (left) and simulated by Noah (right). Error bars show standard error of each median value. Markers show median values.

It is apparent from Figure 54 (top) that SMAP observations (left) and Noah simulations (right) both have an increased sensitivity of drying rate to soil moisture content when PE rates are high. SMAP shows this sensitivity to a larger degree than Noah does. For both, when PE rates are low, the drying rates plateau around 0.3 mm/day.

The bottom panels of Figure 54 show that the evaporative efficiency is not affected by the PE rate itself. For both SMAP and Noah, there is an approximately linear relationship between soil moisture content and evaporative efficiency in all three PE terciles. The standard errors overlap.

4.3.2.2 Role of vegetation

Vegetative cover can shade the ground and therefore decrease direct evaporation from the ground. However, it also introduces transpiration. These mechanisms have opposing effects on the overall drying rate shown in Figure 55.

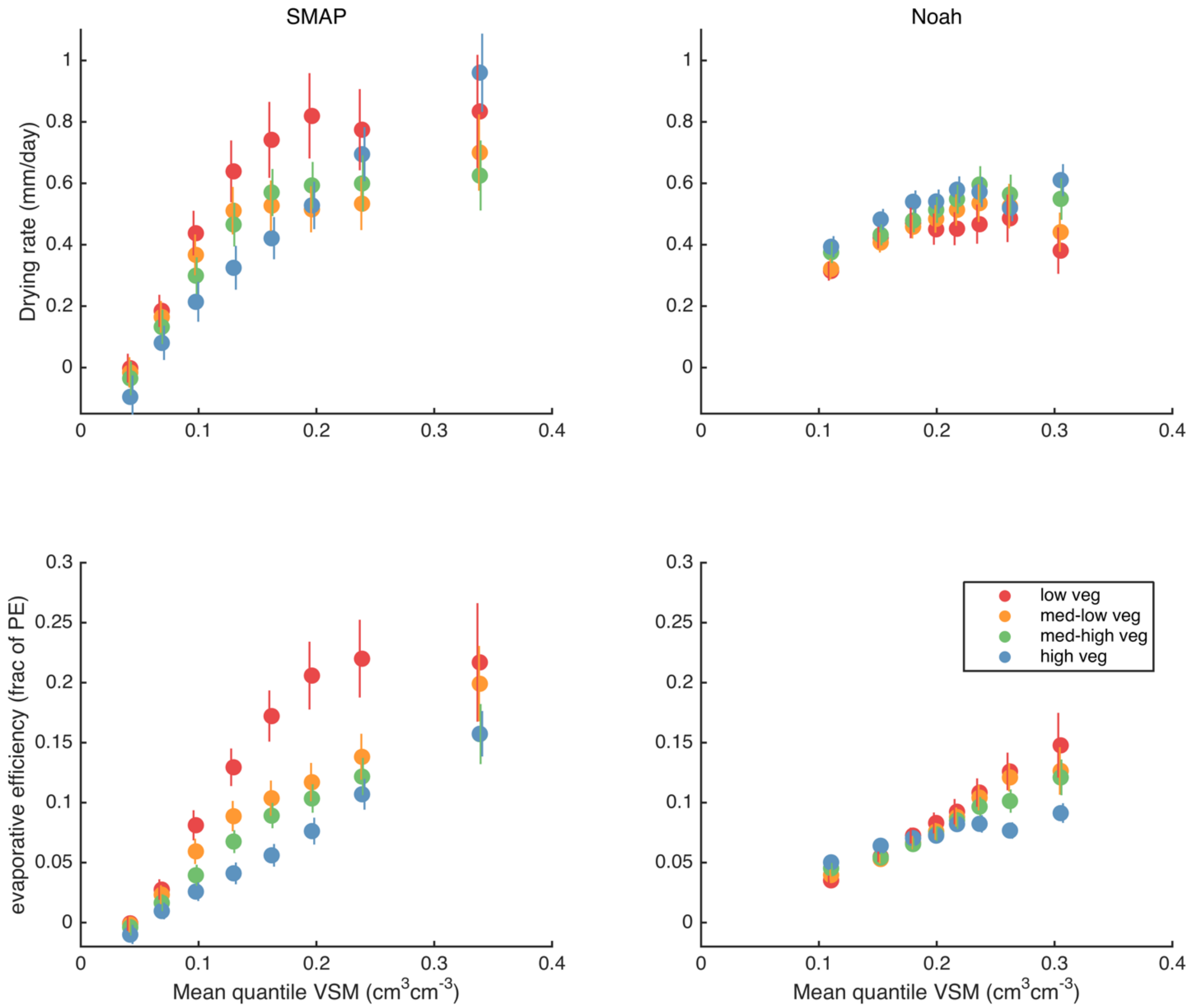

Figure 55: Drying rates (top) and evaporative efficiency (bottom) of surface soil moisture as a function of 8 VSM quantiles (x-axis) and 4 NDVI quantiles (colors). Moisture levels and drying rates are from SMAP observations (left) and Noah simulations (right). Error bars show standard error of each median value. Markers show median values.

The top left panel of Figure 55 shows that according to SMAP observations, (1) drying rate depends highly on VSM, no matter the vegetation level, and (2) at almost all soil moisture levels, the highest drying rates are over pixels with the lowest vegetation levels. The one exception is in the highest soil moisture quantile, where the most densely-vegetated quantile dries faster than the most sparsely-vegetated quantile. (The drying rate of the former increases linearly with VSM, whereas less-vegetated quartiles reach a plateau.) The top right panel shows that Noah simulations exhibit a weakly positive dependence of drying rate on VSM. At all soil moisture levels, more vegetation is associated with faster Noah drying rates, which is the opposite from how vegetation affects SMAP drying rates.

The bottom two panels of Figure 55 show the same data as those above them, but drying rates are expressed as a fraction of potential evaporation. This normalization removes the negative correlation of PE with VSM (Figure 53) and the positive correlation of PE with NDVI (Figure 51). For both SMAP and Noah, evaporative efficiency monotonically increases with soil moisture, except for a plateau in the low vegetation quartile at SMAP VSMs between 0.25 and 0.35 cm^3 cm^{-3}.

Both SMAP and Noah data show a negative effect of vegetation on evaporative efficiency. For SMAP (bottom left), the trend is the same as it was prior to normalization. More vegetation unequivocally decreases evaporative efficiency. For Noah (bottom right), the trend is weak, but the effect of vegetation is in the opposite direction from pre-normalization (top right). At most Noah-simulated VSM levels, evaporative efficiency is higher when vegetation cover is low.

4.4 Discussion

The data from NASA's SMAP mission, combined with existing environmental remote sensing and modeling data, have provided insights into the environmental factors affecting surface soil moisture dynamics.

Overall, SMAP drying timescales are about half as long as those from Noah simulations. The most likely cause for this disparity is the difference between

SMAP sensing depth (between the surface and up to 5 cm) and the thickness of the shallowest soil layer being simulated in Noah (prescribed at 0-10 cm). Soil drying starts at the surface and progresses into the ground [*Schneeberger et al.*, 2004], so it is expected that the top few centimeters should dry over a shorter time period than soil near the bottom of Noah's first layer.

The difference in representative depths also plays a role in the relative contributions of surface evaporation and transpiration. Bare soil evaporation plays a proportionally smaller role for a thick surface layer than it does a thin one. Transpiration pulls about equally from all parts of a layer, assuming uniform wetness and root distribution. Therefore, as soil shifts from bare to vegetated, the soil depth being represented will determine how drying is partitioned between evaporation and transpiration.

In the transition from low to moderate NDVI (0.1 to 0.35), SMAP observations show a lengthening of the drying timescale (Figure 50). We attribute this change to an increase in the shaded ground area and aerodynamic resistance. The resulting decrease of direct evaporation from the soil surface is not offset by the increase in transpiration out of the top few centimeters that the vegetation provides. Noah simulations, on the other hand, show the opposite effect through the same NDVI interval. The increase in transpiration from the top 10 centimeters is greater than the decrease in surface evaporation, so the overall effect of increased vegetation is a shortening of the drying timescale. As a reminder, Noah uses a climatology-based parameter to assign fractional vegetation cover. Our NDVI values are from real observations. Using climatological values dampens but does not change the effects seen in Figure 50, since seasonality will never correspond perfectly with the conditions of any given year.

Soil texture is a fundamental component of soil infiltration and redistribution models [*Campbell*, 1974; *Van Genuchten*, 1980; *Chen and Dudhia*, 2001]. It is expected that the higher water tension that fine-grained soils (silts and clays) provide should hold soil water longer than coarse grained soils (sands) as the soil dries. Our results show an overall trend that supports this theory (Figure 48, Table 8). However, the correspondence between grain size and drying timescale is not perfect, and it is exhibited to different degrees by SMAP observations and Noah simulations. Noah has soil parameters for each texture category coded into it, which provides for different wilting points, field capacities, and hydraulic diffusivities and conductivities [*Chen and Dudhia*, 2001]. SMAP shows that while it is true that different soil textures have different dynamics, the degree of those differences is much smaller (46% versus 89%) than Noah simulations would suggest.

The inexact correspondence of drying timescales with soil texture between SMAP and Noah supports the findings of *Xia et al.* [2015]: substituting one soil map with another will not improve simulations. The relationship between soil textures and parameters are built around laboratory experiments [*Campbell*, 1974] that only approximate those that are seen on a ~10 km scale. Chapter 2 corroborates the fact that map- and laboratory-based soil textures are not optimal for use at the landscape scale [*Shellito et al.*, 2016a].

In assessing soil drying rates, we must simultaneously consider the supply of water (soil moisture), the atmospheric demand for it (PE), and the vegetative cover (NDVI). Having established that NDVI affects drying behavior, we look at the role of PE and soil moisture. Three conclusions come out of Figure 54, all of which are supported by both SMAP observations and Noah simulations: (1) drying rates are positively related to soil moisture content, (2) the sensitively of drying rates to soil moisture depends on PE (higher PE results in higher sensitivities), and (3) evaporative efficiency is linearly related to soil moisture, regardless of PE rate. All three points indicate that at the continental scale, evapotranspiration is water-limited (stage 2 evaporation). These conclusions support our working assumption that saturation beyond the field capacity, where gravity drainage is active and evaporation is limited by PE, is uncommon at the timescales of our observations and simulations.

Lastly, we lastly look to Figure 55 to understand the role of vegetation on drying rates, independent of soil moisture and PE rate. According to SMAP observations, vegetation has a strong influence on evaporative efficiency at every soil moisture level. Areas with less vegetation have higher evaporative efficiencies. This translates to faster drying rates, which corroborates our earlier findings that SMAP drying timescales are shorter when NDVI is below 0.35. The only exception to this trend is highly vegetated pixels that are also in the wettest quartile. High NDVI usually means high PE (Figure 51), and ample moisture supply ensures the atmospheric demand is met. This category therefore has the fastest overall drying rates of all shown, but only because its PE rate is also high, not because of the vegetation present.

The implications of Figure 55 regarding Noah simulations are subtler. For most moisture levels, vegetation correlates with lower evaporative efficiencies. However, because the Noah model layer is thicker than the SMAP sensing layer, transpiration is more effective at offsetting this decrease in efficiency. This results in a weaker negative relationship between vegetation and surface evaporation than is seen using the shallower SMAP observations. When looking at drying rates themselves (Figure 55, top right), we see the relationship is entirely obscured and in fact flipped because of the higher PE rates that well-vegetated pixels tend to have (Figure 51).

In summary, SMAP observations and Noah simulations both support our finding that that given an equal soil moisture level and PE, the presence of vegetation will slow the speed at which surface soil moisture dries. The counter-acting roles vegetation has in increasing shaded area and introducing transpiration make this result dependent on depth, so it is most effectively seen in the SMAP observations. The trend is barely present over the 0-10 cm Noah simulation depth. These findings are most applicable to regions with intermediate moisture levels and relatively sparse vegetation (NDVI < 0.35). Moist soil, thick vegetation, or a thicker soil layer would move the system into a regime where drying is dominated by transpiration, which, given enough atmospheric water demand, would negate the tempering effect that vegetation has on evaporative efficiency.

4.5 Conclusion

We show the ability of SMAP to capture drying dynamics after rain events in North America. The extent of SMAP retrievals is limited by dense vegetation cover in the eastern portion of the domain, but observations are sufficient to draw several conclusions regarding how PE, VSM, NDVI, and soil texture affect soil drying dynamics. We use simulations of soil moisture from the shallowest layer of the Noah LSM to support our findings and gain insight into how the 0-5 cm SMAP dynamics differ from those simulated by the 0-10 cm Noah layer.

1. In North America, drying timescales from SMAP observations are approximately half those from Noah simulations. The longest drydowns from SMAP are found in arid regions. The longest drydowns from Noah are found at high latitudes. In the Great Plains, the Noah drying timescales are consistently twice those of SMAP. We attribute these differences at least in part to the different soil depths being represented.
2. Both SMAP and Noah observations show that soil texture influences drying timescales. The effect is greater for Noah than for SMAP, suggesting that the former places too much weight on this aspect of the system.
3. Drying rates are affected by VSM, PE, and NDVI. More soil moisture and higher PE rates cause faster drying rates. The effect of each is sensitive to and magnified by the other. The presence of vegetation in SMAP observations causes drying rates to decrease. The presence of vegetation in Noah simulations causes drying rates to increase. This difference

implies that transpiration plays a larger role in soil drying as simulated by Noah than as observed by SMAP.

4. We calculate evaporative efficiency by normalizing drying rates by PE. Both SMAP and Noah data show that vegetation decreases evaporative efficiency. The effect of vegetation can be obscured because it is positively correlated with both VSM and PE, two factors that increase surface soil moisture drying rates. It can also be obscured as the soil layer being studied gets thicker and transpiration dynamics overcome those of surface evaporation.

References

Adams, J. R., H. McNairn, A. A. Berg, and C. Champagne (2015), Evaluation of near-surface soil moisture data from an AAFC monitoring network in Manitoba, Canada: Implications for L-band satellite validation, *J. Hydrol.*, *521*, 582–592, doi:10.1016/j.jhydrol.2014.10.024.

Albergel, C., P. de Rosnay, C. Gruhier, J. Muñoz-Sabater, S. Hasenauer, L. Isaksen, Y. Kerr, and W. Wagner (2012), Evaluation of remotely sensed and modelled soil moisture products using global ground-based in situ observations, *Remote Sens. Environ.*, *118*, 215–226, doi:10.1016/j.rse.2011.11.017.

Allen, R. . (2000), Using the FAO-56 dual crop coefficient method over an irrigated region as part of an evapotranspiration intercomparison study, *J. Hydrol.*, *229*(1–2), 27–41, doi:10.1016/S0022-1694(99)00194-8.

Bastidas, L. A., T. S. Hogue, S. Sorooshian, H. V. Gupta, and W. J. Shuttleworth (2006), Parameter sensitivity analysis for different complexity land surface models using multicriteria methods, *J. Geophys. Res.*, *111*(D20), D20101, doi:10.1029/2005JD006377.

Betts, A. K., J. H. Ball, A. C. M. Beljaars, M. J. Miller, and P. A. Viterbo (1996), The land surface-atmosphere interaction: A review based on observational and global modeling perspectives, *J. Geophys. Res.*, *101*(D3), 7209, doi:10.1029/95JD02135.

Beven, K. (1989), Changing ideas in hydrology — The case of physically-based models, *J. Hydrol.*, *105*(1–2), 157–172, doi:10.1016/0022-1694(89)90101-7.

Beven, K. (1995), Linking parameters across scales: Subgrid parameterizations and scale dependent hydrological models, *Hydrol. Process.*, *9*(5–6), 507–525, doi:10.1002/hyp.3360090504.

Beven, K., and A. Binley (1992), The future of distributed models: Model calibration and uncertainty prediction, *Hydrol. Process.*, *6*(3), 279–298, doi:10.1002/hyp.3360060305.

Beven, K., and P. Germann (1982), Macropores and water flow in soils, *Water Resour. Res.*, *18*(5), 1311–1325, doi:10.1029/WR018i005p01311.

Al Bitar, A., D. Leroux, Y. H. Kerr, O. Merlin, P. Richaume, A. Sahoo, and E. F. Wood (2012), Evaluation of SMOS Soil Moisture Products Over Continental U.S. Using the SCAN/SNOTEL Network, *IEEE Trans. Geosci. Remote Sens.*, *50*(5), 1572–1586, doi:10.1109/TGRS.2012.2186581.

Blankenship, C., J. Case, B. Zavodsky, and G. Jedlovec (2014), Assimilation of SMOS Retrieved Soil Moisture into the Land Information System, in *EUMETSAT Conference 2014; 22-26 Sep. 2014*, p. 8, Geneva, Switzerland.

Bosch, D. D., V. Lakshmi, T. J. Jackson, M. Choi, and J. M. Jacobs (2006), Large scale measurements of soil moisture for validation of remotely sensed data: Georgia soil moisture experiment of 2003, *J. Hydrol.*, *323*(1–4), 120–137, doi:10.1016/j.jhydrol.2005.08.024.

Boyle, D. P., H. V. Gupta, and S. Sorooshian (2000), Toward improved calibration of hydrologic models: Combining the strengths of manual and automatic methods, *Water Resour. Res.*, *36*(12), 3663, doi:10.1029/2000WR900207.

Burke, E. J., R. J. Gurney, L. P. Simmonds, and T. J. Jackson (1997), Calibrating a soil water and energy budget model with remotely sensed data to obtain quantitative information about the soil, *Water Resour. Res.*, *33*(7), 1689–1697, doi:10.1029/97WR01000.

Burke, E. J., R. J. Gurney, L. P. Simmonds, and P. E. O'Neill (1998), Using a modeling approach to predict soil hydraulic properties from passive microwave measurements, *IEEE Trans. Geosci. Remote Sens.*, *36*(2), 454–462, doi:10.1109/36.662729.

Campbell, G., and J. Norman (1998), *Introduction to Enviromental Biophysics*, 2nd ed., Springer-Verlag, New York.

Campbell, G. S. (1974), Simple Method for Determining Unsaturated Conductivity from Moisture Retention Data, *Soil Sci.*, *117*(6), 311–314.

Champagne, C., T. Rowlandson, A. Berg, T. Burns, J. L'Heureux, E. Tetlock, J. R. Adams, H. McNairn, B. Toth, and D. Itenfisu (2016), Satellite surface soil moisture from SMOS and Aquarius: Assessment for applications in agricultural landscapes, *Int. J. Appl. Earth Obs. Geoinf.*, *45*, 143–154, doi:10.1016/j.jag.2015.09.004.

Chan, S. K. et al. (2016), Assessment of the SMAP Passive Soil Moisture Product, *IEEE Trans. Geosci. Remote Sens.*, *54*(8), 4994–5007, doi:10.1109/TGRS.2016.2561938.

Chen, F., and J. Dudhia (2001), Coupling an advanced land surface-hydrology model with the Penn State-NCAR MM5 modeling system. Part I: Model implementation and sensitivity, *Mon. Weather Rev.*, *129*(4), 569–585, doi:10.1175/1520-0493(2001)129<0569:CAALSH>2.0.CO;2.

Chen, F., K. Mitchell, J. Schaake, Y. K. Xue, H. L. Pan, V. Koren, Q. Y. Duan, M. Ek, and A. Betts (1996), Modeling of land surface evaporation by four schemes and comparison with FIFE observations, *J. Geophys. Res.*, *101*(D3), 7251–7268, doi:10.1029/95JD02165.

Coleman, T. F., and Y. Li (1994), On the convergence of interior-reflective Newton methods for nonlinear minimization subject to bounds, *Math. Program.*, *67*(1), 189–224, doi:10.1007/BF01582221.

Coleman, T. F., and Y. Li (1996), An Interior Trust Region Approach for Nonlinear Minimization Subject to Bounds, *SIAM J. Optim.*, *6*(2), 418–445, doi:10.1137/0806023.

Colliander, A. et al. (2015), SMAP L2/L3 Soil Moisture Product Validation using In Situ Based Core Validation Sites,

Colliander, A. et al. (2017), Validation of SMAP surface soil moisture products with core validation sites, *Remote Sens. Environ.*, *191*, 215–231, doi:10.1016/j.rse.2017.01.021.

Collow, T. W., A. Robock, J. B. Basara, and B. G. Illston (2012), Evaluation of SMOS retrievals of soil moisture over the central United States with currently available in situ observations, *J. Geophys. Res.*, *117*(D9), D09113, doi:10.1029/2011JD017095.

Coopersmith, E. J., M. H. Cosh, J. E. Bell, and W. T. Crow (2016), Multi-Profile

Analysis of Soil Moisture within the US Climate Reference Network, *Vadose Zo. J.*, *15*(1), doi:10.2136/vzj2015.01.0016.

Cosby, B. J., G. M. Hornberger, R. B. Clapp, and T. R. Ginn (1984), A Statistical Exploration of the Relationships of Soil Moisture Characteristics to the Physical Properties of Soils, *Water Resour. Res.*, *20*(6), 682–690, doi:10.1029/WR020i006p00682.

Cosgrove, B. A. et al. (2003), Real-time and retrospective forcing in the North American Land Data Assimilation System (NLDAS) project, *J. Geophys. Res.*, *108*(D22), 8842, doi:10.1029/2002JD003118.

Cosh, M. H., T. J. Jackson, R. Bindlish, and J. H. Prueger (2004), Watershed scale temporal and spatial stability of soil moisture and its role in validating satellite estimates, *Remote Sens. Environ.*, *92*(4), 427–435, doi:10.1016/j.rse.2004.02.016.

Cosh, M. H., T. J. Jackson, P. Starks, and G. Heathman (2006), Temporal stability of surface soil moisture in the Little Washita River watershed and its applications in satellite soil moisture product validation, *J. Hydrol.*, *323*(1–4), 168–177, doi:10.1016/j.jhydrol.2005.08.020.

Cosh, M. H., T. J. Jackson, S. Moran, and R. Bindlish (2008), Temporal persistence and stability of surface soil moisture in a semi-arid watershed, *Remote Sens. Environ.*, *112*(2), 304–313, doi:10.1016/j.rse.2007.07.001.

Cosh, M. H., P. J. Starks, J. A. Guzman, and D. N. Moriasi (2014), Upper Washita River Experimental Watersheds: Multiyear Stability of Soil Water Content Profiles, *J. Environ. Qual.*, *43*(4), 1328, doi:10.2134/jeq2013.08.0318.

Crow, W. T., E. F. Wood, and M. Pan (2003), Multiobjective calibration of land surface model evapotranspiration predictions using streamflow observations and spaceborne surface radiometric temperature retrievals, *J. Geophys. Res.*, *108*(D23), 4725, doi:10.1029/2002JD003292.

Crow, W. T., D. G. Miralles, and M. H. Cosh (2010), A quasi-global evaluation system for satellite-based surface soil moisture retrievals, *IEEE Trans. Geosci. Remote Sens.*, *48*(6), 2516–2527, doi:10.1109/TGRS.2010.2040481.

D'Odorico, P., L. Ridolfi, A. Porporato, and I. Rodriguez-Iturbe (2000), Preferential states of seasonal soil moisture: The impact of climate fluctuations, *Water Resour. Res.*, *36*(8), 2209–2219, doi:10.1029/2000WR900103.

Daly, C., R. P. Neilson, and D. L. Phillips (1994), A statistical-topographic model for mapping climatological precipitation over mountainous terrain, *J. Appl. Meteorol.*, *33*(2), 140–158, doi:10.1175/1520-0450(1994)033<0140:ASTMFM>2.0.CO;2.

Daly, E., and A. Porporato (2005), A Review of Soil Moisture Dynamics: From Rainfall Infiltration to Ecosystem Response, *Environ. Eng. Sci.*, *22*(1), 9–24, doi:10.1089/ees.2005.22.9.

Delworth, T. L., and S. Manabe (1993), Climate variability and land-surface processes, *Adv. Water Resour.*, *16*(1), 3–20, doi:10.1016/0309-1708(93)90026-C.

Dobson, M., F. Ulaby, M. Hallikainen, and M. El-rayes (1985), Microwave Dielectric Behavior of Wet Soil-Part II: Dielectric Mixing Models, *IEEE Trans. Geosci. Remote Sens.*, *GE-23*(1), 35–46, doi:10.1109/TGRS.1985.289498.

Doherty, J., and D. Welter (2010), A short exploration of structural noise, *Water Resour. Res.*, *46*(5), n/a-n/a, doi:10.1029/2009WR008377.

Duan, Q., S. Sorooshian, and V. Gupta (1992), Effective and efficient global optimization for conceptual rainfall-runoff models, *Water Resour. Res.*, *28*(4), 1015–1031, doi:10.1029/91WR02985.

Ek, M. B., K. E. Mitchell, Y. Lin, E. Rogers, P. Grunmann, V. Koren, G. Gayno, and J. D. Tarpley (2003), Implementation of Noah land surface model advances in the National Centers for Environmental Prediction operational mesoscale Eta model, *J. Geophys. Res.*, *108*(D22), 8851, doi:10.1029/2002JD003296.

Eltahir, E. A. B. (1998), A Soil Moisture-Rainfall Feedback Mechanism: 1. Theory and observations, *Water Resour. Res.*, *34*(4), 765–776, doi:10.1029/97WR03499.

Eltahir, E. A. B., and P. J.-F. Yeh (1999), On the asymmetric response of aquifer water level to floods and droughts in Illinois, *Water Resour. Res.*, *35*(4), 1199–1217, doi:10.1029/1998WR900071.

Entekhabi, D., I. Rodriguez-Iturbe, and F. Castelli (1996), Mutual interaction of soil moisture state and atmospheric processes, *J. Hydrol.*, *184*(1–2), 3–17, doi:10.1016/0022-1694(95)02965-6.

Entekhabi, D. et al. (2010), The Soil Moisture Active Passive (SMAP) Mission, *Proc. IEEE*, *98*(5), 704–716, doi:10.1109/JPROC.2010.2043918.

Entekhabi, D. et al. (2014), *SMAP Handbook Soil Moisture Active Passive, Mapping Soil Moisture Freeze / Thaw from Space*, Pasadena, CA.

Escorihuela, M. J., A. Chanzy, J. P. Wigneron, and Y. H. Kerr (2010), Effective soil moisture sampling depth of L-band radiometry: A case study, *Remote Sens. Environ.*, *114*(5), 995–1001, doi:10.1016/j.rse.2009.12.011.

Famiglietti, J. S., D. Ryu, A. a. Berg, M. Rodell, and T. J. Jackson (2008), Field observations of soil moisture variability across scales, *Water Resour. Res.*, *44*(1), W01423, doi:10.1029/2006WR005804.

Federer, C. A., C. Vörösmarty, and B. Fekete (2003), Sensitivity of Annual Evaporation to Soil and Root Properties in Two Models of Contrasting Complexity, *J. Hydrometeorol.*, *4*(6), 1276–1290, doi:10.1175/1525-7541(2003)004<1276:SOAETS>2.0.CO;2.

Ferré, P. A., J. H. Knight, D. L. Rudolph, and R. G. Kachanoski (1998), The sample areas of conventional and alternative time domain reflectometry probes, *Water Resour. Res.*, *34*(11), 2971–2979, doi:10.1029/98WR02093.

Ford, T. W., D. B. McRoberts, S. M. Quiring, and R. E. Hall (2015), On the utility of in situ soil moisture observations for flash drought early warning in Oklahoma, USA, *Geophys. Res. Lett.*, *42*(22), 9790–9798, doi:10.1002/2015GL066600.

Franks, S. W., and K. J. Beven (1997), Bayesian estimation of uncertainty in land surface-atmosphere flux predictions, *J. Geophys. Res.*, *102*(D20), 23991, doi:10.1029/97JD02011.

Gelman, A., and D. B. Rubin (1992), Inference from Iterative Simulation Using Multiple Sequences, *Stat. Sci.*, *7*(4), 457–472, doi:10.1214/ss/1177011136.

Van Genuchten, M. T. (1980), A Closed-Form Equation for Predicting the Hydraulic Conductivity of Unsaturated Soils, *Soil Sci. Soc. Am. J.*, *44*(5), 892–898.

Ghannam, K., T. Nakai, A. Paschalis, C. A. Oishi, A. Kotani, Y. Igarashi, T. Kumagai, and G. G. Katul (2016), Persistence and memory timescales in root-zone soil moisture dynamics, *Water Resour. Res.*, *52*(2), 1427–1445, doi:10.1002/2015WR017983.

Grayson, R. B., and G. Blöschl (Eds.) (2000), *Spatial Patterns in Catchment Hydrology*, Cambridget University Press, Cambridge, UK.

Guillod, B. P., E. L. Davin, C. Kündig, G. Smiatek, and S. I. Seneviratne (2013), Impact of soil map specifications for European climate simulations, *Clim. Dyn.*, *40*(1–2), 123–141, doi:10.1007/s00382-012-1395-z.

Gupta, H. V., S. Sorooshian, and P. O. Yapo (1998), Toward improved calibration of hydrologic models: Multiple and noncommensurable measures of information, *Water Resour. Res.*, *34*(4), 751, doi:10.1029/97WR03495.

Gupta, H. V., L. a. Bastidas, S. Sorooshian, W. J. Shuttleworth, and Z. L. Yang (1999), Parameter estimation of a land surface scheme using multicriteria methods, *J. Geophys. Res.*, *104*(D16), 19491–19503, doi:10.1029/1999JD900154.

Guswa, A. J., M. A. Celia, and I. Rodriguez-Iturbe (2002), Models of soil moisture dynamics in ecohydrology: A comparative study, *Water Resour. Res.*, *38*(9), 5-1-5–15, doi:10.1029/2001WR000826.

Gutmann, E. D., and E. E. Small (2005), The effect of soil hydraulic properties vs. soil texture in land surface models, *Geophys. Res. Lett.*, *32*(2), L02402–L02402, doi:10.1029/2004GL021843.

Gutmann, E. D., and E. E. Small (2007), A comparison of land surface model soil hydraulic properties estimated by inverse modeling and pedotransfer functions, *Water Resour. Res.*, *43*(5), W05418–W05418, doi:10.1029/2006WR005135.

Gutmann, E. D., and E. E. Small (2010), A method for the determination of the hydraulic properties of soil from MODIS surface temperature for use in land-surface models, *Water Resour. Res.*, *46*, W06520, doi:10.1029/2009WR008203.

Hansen, M., R. DeFries, J. R. G. Townshend, and R. Sohlberg (2000), Global land cover classification at 1 km spatial resolution using a classification tree approach, *Int. J. Remote Sens.*, *21*(6), 1331–1364.

Harrison, K. W., S. V. Kumar, C. D. Peters-Lidard, and J. A. Santanello (2012), Quantifying the change in soil moisture modeling uncertainty from remote sensing observations using Bayesian inference techniques, *Water Resour. Res.*, *48*(11), n/a-n/a, doi:10.1029/2012WR012337.

Harter, T., and J. W. Hopmans (2004), Role of vadose-zone flow processes in regional-scale hydrology: review, opportunities, and challenges, in *Unsaturated-zone Modeling: Progress, Challenges and Applications*, edited by R. A. Feddes, G. H. de Rooij, and J. C. van Dam, pp. 179–208, Kluwer Academic Publishers, Dordrecht, the Netherlands.

Hogue, T. S., L. Bastidas, H. Gupta, S. Sorooshian, K. Mitchell, and W. Emmerich (2005), Evaluation and Transferability of the Noah Land Surface Model in Semiarid Environments, *J. Hydrometeorol.*, *6*(1), 68–84, doi:10.1175/JHM-402.1.

Hogue, T. S., L. A. Bastidas, H. V. Gupta, and S. Sorooshian (2006), Evaluating model performance and parameter behavior for varying levels of land surface model complexity, *Water Resour. Res.*, *42*(8), n/a-n/a, doi:10.1029/2005WR004440.

Holtan, H. N., C. B. England, G. P. Lawless, and G. A. Schumaker (Eds.) (1968), *Moisture-tension data for selected soils on experimental watersheds*, Agriculture Research Service, U.S. Department of Agriculture, Beltsville, MD.

Hossain, F., and E. N. Anagnostou (2005), Numerical investigation of the impact of uncertainties in satellite rainfall estimation and land surface model parameters on simulation of soil moisture, *Adv. Water Resour.*, *28*(12), 1336–1350, doi:10.1016/j.advwatres.2005.03.013.

Houser, P. R., H. V. Gupta, W. J. Shuttleworth, and J. S. Famiglietti (2001), Multiobjective calibration and sensitivity of a distributed land surface water and energy balance model, *J. Geophys. Res.*, *106*(D24), 33421, doi:10.1029/2000JD900803.

Ines, A. V. M., and B. P. Mohanty (2009), Near-surface soil moisture assimilation for quantifying effective soil hydraulic properties using genetic algorithms: 2. Using airborne remote sensing during SGP97 and SMEX02, *Water Resour. Res.*, *45*(1), n/a-n/a, doi:10.1029/2008WR007022.

Ivanov, V. Y., R. L. Bras, and E. R. Vivoni (2008), Vegetation-hydrology dynamics in complex terrain of semiarid areas: 1. A mechanistic approach to modeling dynamic feedbacks, *Water Resour. Res.*, *44*(3), W03429, doi:10.1029/2006WR005588.

Jackson, T. J. (1980), Profile soil moisture from surface measurements, *J. Irrig. Drain. Div. Am. Soc. Civ. Eng.*, *106*(IR2), 81–92.

Jackson, T. J., and P. O'Neill (1987), Temporal observations of surface soil moisture using a passive microwave sensor, *Remote Sens. Environ.*, *21*(3), 281–296, doi:10.1016/0034-4257(87)90013-7.

Jackson, T. J., and T. J. Schmugge (1989), Passive Microwave Remote Sensing System for Soil Moisture: Some Supporting Research, *IEEE Trans. Geosci. Remote Sens.*, *27*(2), 225–235, doi:10.1109/36.20301.

Jackson, T. J., M. H. Cosh, R. Bindlish, P. J. Starks, D. D. Bosch, M. Seyfried, D. C. Goodrich, M. S. Moran, and J. Du (2010), Validation of Advanced Microwave Scanning Radiometer Soil Moisture Products, *IEEE Trans. Geosci. Remote Sens.*, *48*(12), 4256–4272, doi:10.1109/TGRS.2010.2051035.

Jackson, T. J. et al. (2012), Validation of Soil Moisture and Ocean Salinity (SMOS) Soil Moisture Over Watershed Networks in the U.S., *IEEE Trans. Geosci. Remote Sens.*, *50*(5), 1530–1543, doi:10.1109/TGRS.2011.2168533.

Jackson, T. J. et al. (2016), *Calibration and Validation for the L2/3_SM_P Version 3 Data Products*, Pasadena, CA.

Juglea, S., Y. Kerr, A. Mialon, J. P. Wigneron, E. Lopez-Baeza, A. Cano, A. Albitar, C. Millan-Scheiding, M. Carmen Antolin, and S. Delwart (2010), Modelling soil moisture at SMOS scale by use of a SVAT model over the Valencia Anchor Station, *Hydrol. Earth Syst. Sci.*, *14*(5), 831–846, doi:10.5194/hess-14-831-2010.

Kerr, Y. H., P. Waldteufel, P. Richaume, I. Davenport, P. Ferrazoli, and J.-P.

Wigneron (2010a), *SMOS Level 2 Processor for Soil Moisture Algorithm Theoretical Basis Document (ATBD)*, Toulouse, France.

Kerr, Y. H. et al. (2010b), The SMOS Mission: New Tool for Monitoring Key Elements of the Global Water Cycle, *Proc. IEEE*, *98*(5), 666–687, doi:10.1109/JPROC.2010.2043032.

Koren, V., F. Moreda, and M. Smith (2008), Use of soil moisture observations to improve parameter consistency in watershed calibration, *Phys. Chem. Earth*, *33*(17–18), 1068–1080, doi:10.1016/j.pce.2008.01.003.

Koster, R. D. et al. (2004), Regions of strong coupling between soil moisture and precipitation, *Science (80-.).*, *305*(5687), 1138–1140, doi:10.1126/science.1100217.

Koster, R. D. et al. (2006), GLACE: The Global Land–Atmosphere Coupling Experiment. Part I: Overview, *J. Hydrometeorol.*, *7*(4), 590–610, doi:10.1175/JHM510.1.

Kurc, S. A., and E. E. Small (2004), Dynamics of evapotranspiration in semiarid grassland and shrubland ecosystems during the summer monsoon season, central New Mexico, *Water Resour. Res.*, *40*(9), W09305–W09305, doi:10.1029/2004WR003068.

Laio, F., A. Porporato, L. Ridolfi, and I. Rodriguez-Iturbe (2001), Plants in water-controlled ecosystems: active role in hydrologic processes and response to water stress, *Adv. Water Resour.*, *24*(7), 707–723, doi:10.1016/S0309-1708(01)00005-7.

Liang, X., J. Guo, and L. R. Leung (2004), Assessment of the effects of spatial resolutions on daily water flux simulations, *J. Hydrol.*, *298*(1–4), 287–310, doi:10.1016/j.jhydrol.2003.07.007.

Liu, Y., H. V. Gupta, S. Sorooshian, L. A. Bastidas, and W. J. Shuttleworth (2005), Constraining Land Surface and Atmospheric Parameters of a Locally Coupled Model Using Observational Data, *J. Hydrometeorol.*, *6*(2), 156–172, doi:10.1175/JHM407.1.

Mahfouf, J. F., and J. Noilhan (1991), Comparative Study of Various Formulations of Evaporations from Bare Soil Using In Situ Data, *J. Appl. Meteorol.*, *30*(9), 1354–1365, doi:10.1175/1520-0450(1991)030<1354:CSOVFO>2.0.CO;2.

Mahrt, L., and M. Ek (1984), The Influence of Atmospheric Stability on Potential Evaporation, *J. Clim. Appl. Meteorol.*, *23*(2), 222–234, doi:10.1175/1520-0450(1984)023<0222:TIOASO>2.0.CO;2.

Martens, B., D. Miralles, H. Lievens, D. Fernández-Prieto, and N. E. C. Verhoest (2016), Improving terrestrial evaporation estimates over continental Australia through assimilation of SMOS soil moisture, *Int. J. Appl. Earth Obs. Geoinf.*, *48*, 146–162, doi:10.1016/j.jag.2015.09.012.

Mattikalli, N. M., E. T. Engman, L. R. Ahuja, and T. J. Jackson (1998), Microwave remote sensing of soil moisture for estimation of profile soil property, *Int. J. Remote Sens.*, *19*(9), 1751–1767, doi:10.1080/014311698215234.

McColl, K. A., S. H. Alemohammad, R. Akbar, A. G. Konings, S. Yueh, and D. Entekhabi (2017), The global distribution and dynamics of surface soil moisture, *Nat. Geosci.*, doi:10.1038/ngeo2868.

Miller, D. A., and R. A. White (1998), A Conterminous United States Multilayer Soil Characteristics Dataset for Regional Climate and Hydrology Modeling, *Earth Interact.*, *2*(2), 1–26, doi:10.1175/1087-3562(1998)002<0001:ACUSMS>2.3.CO;2.

Milzow, C., P. E. Krogh, and P. Bauer-Gottwein (2011), Combining satellite radar altimetry, SAR surface soil moisture and GRACE total storage changes for hydrological model calibration in a large poorly gauged catchment, *Hydrol. Earth Syst. Sci.*, *15*(6), 1729–1743, doi:10.5194/hess-15-1729-2011.

Mitchell, K. E. et al. (2004), The multi-institution North American Land Data Assimilation System (NLDAS): Utilizing multiple GCIP products and partners in a continental distributed hydrological modeling system, *J. Geophys. Res.*, *109*(D7), 1–32, doi:10.1029/2003JD003823.

Monteith, J. L., and M. Unsworth (2013), *Principles of environmental physics*, 4th ed., Academic Press, Oxford.

Nandagiri, L. (2007), Calibrating hydrological models in ungauged basins : possible use of areal evapotranspiration instead of streamflows, in *Predictions in Ungauged Basins: PUB Kick-off (Proceedings of the Kick-off meeting held in Brasilia, 20-22 November 2002)*, pp. 275–281, IAHS.

NASA LP DAAC (2016), MOD13A2 Level 3 Vegetation Indices. Version 5. NASA EOSDIS Land Processes DAAC, USGS Earth Resources Observation and Science (EROS) Center, Sioux Falls, South Dakota (https://lpdaac.usgs.gov), accessed [12 31, 2016], at https://lpdaac.,

Njoku, E. G., and D. Entekhabi (1996), Passive microwave remote sensing of soil moisture, *J. Hydrol.*, *184*(1–2), 101–129, doi:10.1016/0022-1694(95)02970-2.

Njoku, E. G., and J.-A. Kong (1977), Theory for passive microwave remote sensing of near-surface soil moisture, *J. Geophys. Res.*, *82*(20), 3108–3118, doi:10.1029/JB082i020p03108.

Njoku, E. G., T. J. Jackson, V. Lakshmi, T. K. Chan, and S. V Nghiem (2003), Soil Moisture Retrieval From AMSR-E, *IEEE Trans. Geosci. Remote Sens.*, *41*(2), 215–229, doi:10.1109/TGRS.2002.808243.

O'Neill, P. E., S. Chan, E. G. Njoku, T. Jackson, and R. Bindlish (2016), SMAP Enhanced L3 Radiometer Global Daily 9 km EASE-Grid Soil Moisture, Version 1, , doi:10.5067/ZRO7EXJ8O3XI.

Osborne, T. M., D. M. Lawrence, J. M. Slingo, A. J. Challinor, and T. R. Wheeler (2004), Influence of vegetation on the local climate and hydrology in the tropics: Sensitivity to soil parameters, *Clim. Dyn.*, *23*, 45–61, doi:10.1007/s00382-004-0421-1.

Pan, M., A. K. Sahoo, E. F. Wood, A. Al Bitar, D. Leroux, and Y. H. Kerr (2012), An Initial Assessment of SMOS Derived Soil Moisture over the Continental United States, *IEEE J. Sel. Top. Appl. Earth Obs. Remote Sens.*, *5*(5), 1448–1457, doi:10.1109/JSTARS.2012.2194477.

Pauwels, V. R. N., A. Balenzano, G. Satalino, H. Skriver, N. E. C. Verhoest, and F. Mattia (2009), Optimization of Soil Hydraulic Model Parameters Using Synthetic Aperture Radar Data: An Integrated Multidisciplinary Approach, *IEEE Trans. Geosci. Remote Sens.*, *47*(2), 455–467, doi:10.1109/TGRS.2008.2007849.

Penman, H. L. (1948), Natural Evaporation from Open Water, Bare Soil and Grass, *Proc. R. Soc. A Math. Phys. Eng. Sci.*, *193*(1032), 120–145, doi:10.1098/rspa.1948.0037.

Peters-Lidard, C. D., D. M. Mocko, M. Garcia, J. A. Santanello, M. A. Tischler, M. S. Moran, and Y. Wu (2008), Role of precipitation uncertainty in the estimation of hydrologic soil properties using remotely sensed soil moisture in a semiarid environment, *Water Resour. Res.*, *44*(5), n/a-n/a, doi:10.1029/2007WR005884.

Pinker, R. T. et al. (2003), Surface radiation budgets in support of the GEWEX Continental-Scale International Project (GCIP) and the GEWEX Americas Prediction Project (GAPP), including the North American Land Data Assimilation System (NLDAS) project, *J. Geophys. Res.*, *108*(D22), 8844, doi:10.1029/2002JD003301.

Pitman, A. J. (2003), The evolution of, and revolution in, land surface schemes designed for climate models, *Int. J. Climatol.*, *23*(5), 479–510, doi:10.1002/joc.893.

Porporato, A., P. D'Odorico, F. Laio, and I. Rodriguez-Iturbe (2003), Hydrologic controls on soil carbon and nitrogen cycles. I. Modeling scheme, *Adv. Water Resour.*, *26*(1), 45–58, doi:10.1016/S0309-1708(02)00094-5.

Porporato, A., E. Daly, and I. Rodriguez-Iturbe (2004), Soil Water Balance and Ecosystem Response to Climate Change, *Am. Nat.*, *164*(5), 625–632, doi:10.1086/424970.

Rawls, W. J., P. Yates, and L. Asmussen (1976), *Calibration of selected infiltration equations for the Georgia Coastal Plain*, U.S. Department of Agriculture, Beltsville, MD.

Reichle, R. H., and R. D. Koster (2004), Bias reduction in short records of satellite soil moisture, *Geophys. Res. Lett.*, *31*(19), L19501, doi:10.1029/2004GL020938.

Richards, L. A. (1931), Capillary conduction of liquids through porous mediums, *J. Appl. Phys.*, *1*(5), 318, doi:10.1063/1.1745010.

Richter, H., A. W. Western, and F. H. S. Chiew (2004), The Effect of Soil and Vegetation Parameters in the ECMWF Land Surface Scheme, *J. Hydrometeorol.*, *5*(6), 1131–1146, doi:10.1175/JHM-362.1.

Rodell, M., and H. K. Beaudoing (2007), GLDAS Noah Land Surface Model L4 3 Hourly 0.25 x 0.25 degree Subsetted, version 001, , doi:10.5067/F4KOLPJZHKOT.

Rodriguez-Iturbe, I. (2000), Ecohydrology: A hydrologic perspective of climate-soil-vegetation dynamies, *Water Resour. Res.*, *36*(1), 3–9, doi:10.1029/1999WR900210.

Rondinelli, W. J., B. K. Hornbuckle, J. C. Patton, M. H. Cosh, V. A. Walker, B. D. Carr, and S. D. Logsdon (2015), Different Rates of Soil Drying after Rainfall Are Observed by the SMOS Satellite and the South Fork in situ Soil Moisture Network, *J. Hydrometeorol.*, *16*(2), 889–903, doi:10.1175/JHM-D-14-0137.1.

Rosero, E., Z.-L. Yang, T. Wagener, L. E. Gulden, S. Yatheendradas, and G.-Y. Niu (2010), Quantifying parameter sensitivity, interaction, and transferability in hydrologically enhanced versions of the Noah land surface model over transition zones during the warm season, *J. Geophys. Res.*, *115*(D3), D03106, doi:10.1029/2009JD012035.

Salvucci, G. D., and D. Entekhabi (2011), An alternate and robust approach to calibration for the estimation of land surface model parameters based on remotely sensed observations, *Geophys. Res. Lett.*, *38*(16), L16404, doi:10.1029/2011GL048366.

Santanello, J. A., C. D. Peters-Lidard, M. E. Garcia, D. M. Mocko, M. A. Tischler, M. S. Moran, and D. P. Thoma (2007), Using remotely-sensed estimates of soil moisture to infer soil texture and hydraulic properties across a semi-arid watershed, *Remote Sens. Environ.*, *110*, 79–97, doi:10.1016/j.rse.2007.02.007.

Saxton, K. E., W. J. Rawls, J. S. Romberger, and R. I. Papendick (1986), Estimating Generalized Soil-water Characteristics from Texture, *Soil Sci. Soc. Am. J.*, *50*(4), 1031–1036, doi:10.2136/SSSAJ1986.03615995005000040039X.

Schaap, M. G., and F. J. Leij (1998), Database-Related Accuracy and Uncertainty of Pedotransfer Functions, *Soil Sci.*, *163*(10), 765–779, doi:10.1097/00010694-199810000-00001.

Schär, C., D. Lüthi, U. Beyerle, and E. Heise (1999), The soil-precipitation feedback: A process study with a regional climate model, *J. Clim.*, *12*, 722–741.

Schenk, H. J., and R. B. Jackson (2002), The Global Biogeography of Roots, *Ecol. Monogr.*, *72*(3), 311–328, doi:10.1890/0012-9615(2002)072[0311:TGBOR]2.0.CO;2.

Schneeberger, K., C. Stamm, C. Matzler, and H. Fluhler (2004), Ground-Based Dual-Frequency Radiometry of Bare Soil at High Temporal Resolution, *IEEE Trans. Geosci. Remote Sens.*, *42*(3), 588–595, doi:10.1109/TGRS.2003.821058.

Schulze-Makuch, D., D. A. Carlson, D. S. Cherkauer, and P. Malik (1999), Scale Dependency of Hydraulic Conductivity in Heterogeneous Media, *Groundwater*, *37*(6), 904–919, doi:10.1111/j.1745-6584.1999.tb01190.x.

Seneviratne, S. I., T. Corti, E. L. Davin, M. Hirschi, E. B. Jaeger, I. Lehner, B. Orlowsky, and A. J. Teuling (2010), Investigating soil moisture–climate interactions in a changing climate: A review, *Earth Sci. Rev.*, *99*(3–4), 125–161, doi:10.1016/j.earscirev.2010.02.004.

Serafini, V. V., and Y. C. Sud (1987), The time scale of the soil hydrology using a simple water budget model, *J. Climatol.*, *7*(6), 585–591, doi:10.1002/joc.3370070606.

Seyfried, M. S., L. E. Grant, E. Du, and K. Humes (2005), Dielectric Loss and Calibration of the Hydra Probe Soil Water Sensor, *Vadose Zo. J.*, *4*(4), 1070, doi:10.2136/vzj2004.0148.

Shellito, P. J., E. E. Small, and M. H. Cosh (2016a), Calibration of Noah Soil Hydraulic Property Parameters Using Surface Soil Moisture from SMOS and Basinwide In Situ Observations, *J. Hydrometeorol.*, *17*(8), 2275–2292, doi:10.1175/JHM-D-15-0153.1.

Shellito, P. J. et al. (2016b), SMAP soil moisture drying more rapid than observed in situ following rainfall events, *Geophys. Res. Lett.*, *43*(15), 8068–8075, doi:10.1002/2016GL069946.

Shuttleworth, W. J. (2012), *Terrestrial Hydrometeorology*, John Wiley & Sons, Ltd., Oxford.

Singh, S. K., A. Bárdossy, J. Götzinger, and K. P. Sudheer (2012), Effect of spatial resolution on regionalization of hydrological model parameters, *Hydrol. Process.*, *26*(23), 3499–3509, doi:10.1002/hyp.8424.

Skamarock, W. C., J. B. Klemp, J. Dudhia, D. O. Gill, D. M. Barker, M. G. Duda, X.-Y. Huang, W. Wang, and J. G. Powers (2008), A description of the advanced research WRF version 3, *NCAR Tech. Note NCAR/TN-475+STR*, (June), 125.

Soet, M., and J. N. M. Stricker (2003), Functional behaviour of pedotransfer functions in soil water flow simulation, *Hydrol. Process.*, *17*(8), 1659–1670, doi:10.1002/hyp.1207.

Sorooshian, S., Q. Duan, and V. K. Gupta (1993), Calibration of rainfall-runoff models: Application of global optimization to the Sacramento Soil Moisture Accounting Model, *Water Resour. Res.*, *29*(4), 1185, doi:10.1029/92WR02617.

Teuling, A. J., R. Uijlenhoet, B. van den Hurk, and S. I. Seneviratne (2009), Parameter Sensitivity in LSMs: An Analysis Using Stochastic Soil Moisture Models and ELDAS Soil Parameters, *J. Hydrometeorol.*, *10*(3), 751–765, doi:10.1175/2008JHM1033.1.

Topp, G. C., and J. L. Davis (1985), Measurement of Soil Water Content using Time-domain Reflectrometry (TDR): A Field Evaluation, *Soil Sci. Soc. Am. J.*, *49*(1), 19, doi:10.2136/sssaj1985.03615995004900010003x.

Topp, G. C., J. L. Davis, and A. P. Annan (1980), Electromagnetic determination of soil water content: Measurements in coaxial transmission lines, *Water Resour. Res.*, *16*(3), 574–582, doi:10.1029/WR016i003p00574.

Troy, T. J., E. F. Wood, and J. Sheffield (2008), An efficient calibration method for continental-scale land surface modeling, *Water Resour. Res.*, *44*(9), n/a-n/a, doi:10.1029/2007WR006513.

Tuttle, S., and G. Salvucci (2016), Empirical evidence of contrasting soil moisture-precipitation feedbacks across the United States, *Science (80-.).*, *352*(6287), 825–828, doi:10.1126/science.aaa7185.

Ulaby, F. T., R. K. Moore, and A. K. Fung (1986), *Microwave Remote Sensing: Active and Passive, Vol III, From Theory to Applications*, Artech House, Norwood, MA.

Vereecken, H., R. Kasteel, J. Vanderborght, and T. Harter (2007), Upscaling Hydraulic Properties and Soil Water Flow Processes in Heterogeneous Soils, *Vadose Zo. J.*, *6*(1), 1, doi:10.2136/vzj2006.0055.

Viterbo, P., and A. K. Betts (1999), Impact of the ECMWF reanalysis soil water on forecasts of the July 1993 Mississippi flood, *J. Geophys. Res. Atmos.*, *104*(D16), 19361–19366, doi:10.1029/1999JD900449.

Vrugt, J. A., H. V. Gupta, W. Bouten, and S. Sorooshian (2003), A Shuffled Complex Evolution Metropolis algorithm for optimization and uncertainty assessment of hydrologic model parameters, *Water Resour. Res.*, *39*(8), n/a-n/a, doi:10.1029/2002WR001642.

Vrugt, J. A., C. J. F. ter Braak, M. P. Clark, J. M. Hyman, and B. A. Robinson

(2008), Treatment of input uncertainty in hydrologic modeling: Doing hydrology backward with Markov chain Monte Carlo simulation, *Water Resour. Res.*, *44*(12), W00B09, doi:10.1029/2007WR006720.

Vrugt, J. A., B. A. Robinson, and J. M. Hyman (2009), Self-Adaptive Multimethod Search for Global Optimization in Real-Parameter Spaces, *IEEE Trans. Evol. Comput.*, *13*(2), 243–259, doi:10.1109/TEVC.2008.924428.

Wang, K., and R. E. Dickinson (2012), A review of global terrestrial evapotranspiration: Observation, modeling, climatology, and climatic variability, *Rev. Geophys.*, *50*(2), doi:10.1029/2011RG000373.

Western, A. W., R. B. Grayson, and G. Blöschl (2002), Scaling of soil moisture: A hydrologic perspective, *Annu. Rev. Earth Planet. Sci.*, *30*(1), 149–180, doi:10.1146/annurev.earth.30.091201.140434.

Wöhling, T., S. Gayler, E. Priesack, J. Ingwersen, H.-D. Wizemann, P. Högy, M. Cuntz, S. Attinger, V. Wulfmeyer, and T. Streck (2013), Multiresponse, multiobjective calibration as a diagnostic tool to compare accuracy and structural limitations of five coupled soil-plant models and CLM3.5, *Water Resour. Res.*, *49*, 8200–8221, doi:10.1002/2013WR014536.

Wooldridge, S. ., J. . Kalma, and J. . Walker (2003), Importance of soil moisture measurements for inferring parameters in hydrologic models of low-yielding ephemeral catchments, *Environ. Model. Softw.*, *18*(1), 35–48, doi:10.1016/S1364-8152(02)00038-5.

Wösten, J. H. M., P. A. Finke, and M. J. W. Jansen (1995), Comparison of class and continuous pedotransfer functions to generate soil hydraulic characteristics, *Geoderma*, *66*(3–4), 227–237, doi:10.1016/0016-7061(94)00079-P.

Xia, Y. (2009), NLDAS Primary Forcing Data L4 Hourly 0.125 x 0.125 degree V002, , doi:10.5067/6J5LHHOHZHN4.

Xia, Y. (2012), NLDAS Noah Land Surface Model L4 Hourly 0.125 x 0.125 degree V002, , doi:10.5067/47Z13FNQODKV.

Xia, Y. et al. (2012a), Continental-scale water and energy flux analysis and validation for North American Land Data Assimilation System project phase 2 (NLDAS-2): 2. Validation of model-simulated streamflow, *J. Geophys. Res.*, *117*(D3), D03110, doi:10.1029/2011JD016051.

Xia, Y. et al. (2012b), Continental-scale water and energy flux analysis and validation for the North American Land Data Assimilation System project phase 2 (NLDAS-2): 1. Intercomparison and application of model products, *J. Geophys. Res.*, *117*(D3), D03109, doi:10.1029/2011JD016048.

Xia, Y., M. B. Ek, Y. Wu, T. Ford, and S. M. Quiring (2015), Comparison of NLDAS-2 Simulated and NASMD Observed Daily Soil Moisture. Part II: Impact of Soil Texture Classification and Vegetation Type Mismatches, *J. Hydrometeorol.*, *16*(5), 1981–2000, doi:10.1175/JHM-D-14-0097.1.

Yapo, P. O., H. V. Gupta, and S. Sorooshian (1996), Automatic calibration of conceptual rainfall-runoff models: sensitivity to calibration data, *J. Hydrol.*, *181*(1–4), 23–48, doi:10.1016/0022-1694(95)02918-4.